Guidance on Thickness Design for Wide-Bandgap Semiconductor Thermal Neutron Detectors with Layered Structure and Research on Their Microscopic Radiation Resistance

Submitted in accordance with the requirements
of University of Lancaster for the degree of Doctor of Philosophy

by

Zhang, Zhongming
©2024

July 27, 2024

Commenced ....; Submitted ....; Examined ....; Accepted ....

For Chieh-En,
with love.

Acknowledgements

I would like to thank my supervisor, Dr Michael Aspinall, for his patience in guiding me. He is the one who made my dream of being free to pursue my research in the field of neutron detection come true. He has not only given me support in my studies and research, but has also helped me a lot in my life. Words cannot express the respect and gratitude I have for him. Once again, I sincerely thank him for all that he has done.

I would like to thank Professor Zhifu Zhu of Zhengzhou University for working with me on the exploration of wide-bandgap semiconductor neutron detectors. I thank him for applying for joint funding from the Royal Society International Exchanges 2021 Cost share (£12k, IEC-NSFC-211373), which was successfully awarded. I thank him for his comments on the thesis. I admire his knowledge and attitude towards science.

I am grateful to my colleagues at Donghua University of Technology, Prof Jijun Zou, Qing Zhou, Shuting Yang and others. I thank them for their generosity in providing samples of GaN detectors. I thank them for their help in semiconductor

growth, detector preparation and neutron detection.

Thanks to Dr Samuel Murphy for his generous help with molecular dynamics. Thanks to him for his pertinent advice in the PhD appraisals.

Thanks to Dr Stephen Monk for his valuable advice on the direction of the research and comments on the phase reports in the early stages of the PhD.

Thanks to Prof Stephen Croft for the discussion on the improvement of the thesis.

I acknowledge the School of Engineering at Lancaster University for funding this PhD studentship as part of the Lancaster University College at Beijing Jiaotong University (LUC@BJTU) teaching assistant programme. I also thank the research staff for their helpful discussions and support, particularly Dr Tilly Alton, who provided assistance with the Geant4 installation. Additionally, I would like to express my gratitude to Jayan Suthar for his discussions about the research.

Thanks to the High-End Computing (HEC) cluster and support staff at Lancaster University.

Thank you to my father, Hongjun Zhang, who passed away in 2019. Every moment I will miss the time with him. Thank you to him for teaching me so much in life and for his love that gave me the courage to pursue my dreams. He will always live on in my heart.

Thank you to my mother, Chunhui Zhang, for being a strong woman, for

supporting me in pursuing my dreams, for supporting my research, and for being able to live independently and strongly after my father's death. She is a role model to me.

Thank you to my wife, Chieh-En Yu, for accompanying me on this journey. I thank her for her strength and tolerance, for taking care of me and for her advice on writing my thesis. I would like to say to her that I love you.

Finally, I would like to thank all the people I have met on this amazing journey and for being there for me at every stage. Sincere blessings to them all.

Abstract

In semiconductor neutron detectors with a layered structure, the fundamental structure consists of a converter layer and a semiconductor layer. It has been shown in research focused on these detectors that the thicknesses of both the converter and semiconductor layers crucially impact the efficiency of neutron detection.

However, there is a notable scarcity of studies that determine the optimal thickness of the converter layer and the corresponding optimal thickness of the semiconductor layer, especially using direct theoretical formulas for the efficiency of the converter layer. This lack of research is particularly evident for wide-bandgap semiconductor materials such as diamond, silicon carbide (SiC), gallium oxide (Ga_2O_3), gallium nitride (GaN), and the perovskite material caesium lead bromide ($CsPbBr_3$).

Herein, on the basis of theoretical studies about the efficiency of layered semiconductor detectors, a systematic method has been proposed for calculating the optimal thicknesses for two types of converter layers. This method has been implemented in computational software. By inputting the macroscopic cross-section and the range of secondary charged particles in the converter layer, the software can quickly determine the optimised thickness for B_4C or LiF. Due to the complexity of the theoretical studies, the Monte Carlo method has been innovatively employed to ascertain the optimal thicknesses of diamond, SiC, Ga_2O_3, GaN, and $CsPbBr_3$ for maximising neutron detection efficiency.

Additionally, in anticipation of deploying these detectors in high-radiation environments, further research has been conducted into the micro-radiation processes and radiation resistance of the aforementioned materials, encompassing both neutron and γ radiation. This has led to the identification of the materials' Displacement Per Atom (DPA) values and the maximum growth thickness for γ rays of various energies.

This research will contribute to guiding the manufacturing of wide-bandgap semiconductor neutron detectors and enhancing their production efficiency.

Declaration

I, Zhongming Zhang, hereby certify that this thesis and the research described in it is all my own work unless otherwise indicated and has not been submitted in any previous application for a higher degree. The work presented here was carried out at Lancaster University. I, as the author and candidate, acknowledge Dr Zhifu Zhu, for providing, growing and fabricating semiconductor neutron detectors.

Date........................ Signature of candidate...

Zhongming Zhang

I, Dr Michael Douglas Aspinall, hereby certify that the candidate has fulfilled the conditions of the resolution and regulations appropriate for the degree of Doctor of Philosophy at Lancaster University and that the candidate is qualified to submit this thesis in application for that degree.

Date........................ Signature of supervisor...

Dr Michael Douglas Aspinall

Contents

Acknowledgements **i**

Abstract **iv**

Declaration **vi**

List of tables **ix**

List of figures **xi**

1 Introduction **1**

2 Background **6**

- 2.1 Neutrons . . . 8
- 2.2 Neutron detectors . . . 16
  - 2.2.1 Gas detectors . . . 16
  - 2.2.2 Scintillator detectors . . . 17
  - 2.2.3 Semiconductor detectors . . . 20
- 2.3 Wide-bandgap semiconductor materials for neutron detection . . . 21
  - 2.3.1 Diamond . . . 22
  - 2.3.2 Silicon carbide . . . 24
  - 2.3.3 Gallium oxide . . . 25
  - 2.3.4 Gallium nitride . . . 26
  - 2.3.5 Summary . . . 28
- 2.4 Converter layer . . . 29
  - 2.4.1 Materials . . . 30
  - 2.4.2 Optimal thickness . . . 34
- 2.5 Monte Carlo method . . . 41
- 2.6 Geometry and tracking . . . 44
- 2.7 Molecular dynamics . . . 50
- 2.8 Large-scale atomic/molecular massively parallel simulator . . . 53

3 Methodology **55**

- 3.1 Developed programme . . . 56
  - 3.1.1 Converter layer thickness calculation programme . . . 56
  - 3.1.2 Search for threshold displacement energy programme . . . 64
  - 3.1.3 Automatic semiconductor layer thickness optimisation programme . . . 67
- 3.2 Radiation detection simulations . . . 68

- 3.2.1 Semiconductor layer thickness optimisation simulations . . . 68
- 3.2.2 Gamma resistance simulations 71
- 3.3 Displacement damage simulations 73
  - 3.3.1 Molecular dynamics simulations 73
  - 3.3.2 Monte Carlo simulations 78

4 Results **82**
- 4.1 Monte Carlo simulation model validation 83
- 4.2 Thickness optimisation 87
  - 4.2.1 Converter layer 87
  - 4.2.2 Semiconductor layer 90
- 4.3 Threshold displacement energy of $CsPbBr_3$ 92
- 4.4 Microscopic neutron radiation resistance 96
- 4.5 Gamma rejection capability 101

5 Discussion **109**
- 5.1 Thickness optimisation 110
  - 5.1.1 Converter layer 110
  - 5.1.2 Semiconductor layer 112
- 5.2 Microscopic neutron irradiation damage 119
  - 5.2.1 Threshold displacement energy of $CsPbBr_3$ 119
  - 5.2.2 Displacement per atom 121
- 5.3 Gamma-ray rejection capability 122

6 Conclusions **126**

7 Recommendations **129**

Glossary **133**

Bibliography **138**

Appendix **147**

List of tables

2.1 Material properties of four semiconductors for radiation detection at 300 K [WMBC15]. 28

3.1 The ranges of α-particle and ^7Li in B_4C under LLDs ranging from 100 keV to 900 keV. Q = 2.310 MeV 63
3.2 The ranges of ^3H and α-particle in LiF under LLDs ranging from 100 keV to 900 keV. Q = 4.78 MeV 63
3.3 Force field parameters for the potential model used in LAMMPS simulations. ϵ represents the depth of the potential well. σ is the separation distance where the potential energy is zero. q represent the charge of the ions. 75
3.4 Threshold displacement energy for diamond, 4H-SiC, Ga_2O_3 and GaN. Reference to source is shown in square parentheses. 81

4.1 Comparison converter layer thicknesses for B_4C and LiF with the results of Mcgregor et al.[MHY$^+$03]. 86
4.2 Threshold displacement energies (eV) for each site and different temperature. 92
4.3 Displacements per atom and average primary knock-on atoms energy of five materials under a 1 MeV neutron flux. (The thicknesses of B_4C and LiF are 2.6 μm and 30.6 μm) 100
4.4 Maximum allowable semiconductor thickness in order to get a γ-ray intrinsic detection efficiency smaller than 10^{-6} with 2.32 μm B_4C converter layer for 300 keV LLD with γ-ray range from 0.5 MeV to 1.5 MeV. 102
4.5 Maximum allowable semiconductor thickness in order to get a γ-ray intrinsic detection efficiency smaller than 10^{-6} with 24.89 μm LiF converter layer for 300 keV LLD with γ-ray range from 0.5 MeV to 1.5 MeV. 108

1 Optimised semiconductor thickness with optimal B_4C converter layer thickness for diamond with LLD range from 100 keV to 900 keV. . 147
2 Optimised semiconductor thickness with optimal B_4C converter layer thickness for SiC with LLD range from 100 keV to 900 keV. 148
3 Optimised semiconductor thickness with optimal B_4C converter layer thickness for Ga_2O_3 with LLD range from 100 keV to 900 keV. . . 149
4 Optimised semiconductor thickness with optimal B_4C converter layer thickness for GaN with LLD range from 100 keV to 900 keV. . . . 150

5 Optimised semiconductor thickness with optimal B_4C converter layer thickness for $CsPbBr_3$ with LLD range from 100 keV to 900 keV. . 151
6 Optimised semiconductor thickness with optimal LiF converter layer thickness for diamond with LLD range from 100 keV to 900 keV. . 152
7 Optimised semiconductor thickness with optimal LiF converter layer thickness for SiC with LLD range from 100 keV to 900 keV. 153
8 Optimised semiconductor thickness with optimal LiF converter layer thickness for Ga_2O_3 with LLD range from 100 keV to 900 keV. . . 154
9 Optimised semiconductor thickness with optimal LiF converter layer thickness for GaN with LLD range from 100 keV to 900 keV. . . . 155
10 Optimised semiconductor thickness with optimal LiF converter layer thickness for $CsPbBr_3$ with LLD range from 100 keV to 900 keV. . 156

List of figures

2.1 Number of papers on neutron research as a function of year, based on Web of Science data spanning from 1932 to 2020. 8
2.2 Top: quasi-elastic scattering of the ^{4}He core from a ^{8}He projectile off a proton target in the laboratory frame. The length of the arrows represents the momentum per nucleon (the velocity) of the incoming and outgoing particles. Bottom:the equivalent proton-^{4}He elastic scattering in their centre-of-mass frame. [DAG$^+$22] 15
2.3 The probability of the reaction products entering the detector is a function of the solid angle and the maximum allowable range (L) [MLBO96]. 35
2.4 The initial thermal neutron intensity (I_0) is reduced by absorption in the ^{10}B film thickness is greater than the maximum allowable attenuation range (L) of either or both particles, the initial beam I_0 will be reduced before reaching the sensitive region. Depicted is the case in which the film is greater than both the alpha particle attenuation range (L_α) and the Li ion attenuation range (L_{Li}). Hence the beam intensity is reduced to I_0' at L_α and I_0'' at L_{Li} [MLBO96]. 36
2.5 Events occurring near the contact have a very high probability that one of the reaction products will enter the detector. The probability diminishes as the reactions take place further from the contact [MLBO96]. 37
2.6 Calculated sensitivity of ^{10}B coated GaAs Schottky barrier detectors to thermal neutrons as a function of film thickness. Shown are the sensitivity contributions from the Li ions and α particles as well as the resulting total sensitivity. The analysis was performed for front side irradiation and a particle minimum energy requirement of 300 keV [MLBO96]. 39
2.7 The Top Level Category Diagram of the Geant4 toolkit. The open circle on the joining lines represents a using relationship; the category at the circle end uses the adjoined category [AAA$^+$03]. 48
2.8 A snapshot of the molecular dynamics (MD) simulated system containing graphene membrane for Trihalomethanes (THMs) separation; (green: chlorine, black: carbon, yellow: fluorine, red: oxygen and white: hydrogen). [AKJ15]. 52

3.1 The window of the converter layer thickness calculation programme. 62
3.2 Schematic structure of the simulated detector. 68

3.3 Crystal structure of $CsPbBr_3$ for the molecular dynamics (MD) simulations performed. It shows green spheres representing Cs atoms, yellow spheres representing Br atoms, and Pb atoms inside the gray rhombi. 74
3.4 Potential curves for molecular dynamics (MD) simulations. 77
3.5 The illustrative process of neutron-induced Primary Knock-on Atoms (PKA) and Secondary Knock-on Atoms (SKA) in the semiconductor material. [ZA21a] 79

4.1 Calculation result of 5.84 MeV α-particle in BN from SRIM. 84
4.2 5.84 MeV α-particle detection efficiency versus BN thickness. . . . 85
4.3 Ratio of pulses and incident neutrons as a function of converter layer thickness for a 300 keV LLD and 900 keV LLD [ZA20]. 86
4.4 Comparative analysis of B_4C converter layer thickness at varying LLD thresholds: theory versus Geant4 simulations. 88
4.5 Comparative analysis of LiF converter layer thickness at varying LLD thresholds: theory versus Geant4 simulations. 89
4.6 Spatial distribution of TDE for Cs site. The unit of the temperature scale is eV. 93
4.7 Spatial distribution of TDE for Pb site. The unit of the temperature scale is eV. 94
4.8 Spatial distribution of TDE for Br site. The unit of the temperature scale is eV. 95
4.9 Primary knock-on atoms energy spectrum for diamond. This energy spectrum was created by ROOT. The X-axis shows the energy of PKA in keV. The Y-axis shows the count number of PKA. The figure keys show: Entries, the total number of PKA; Mean, the average PKA energy in keV; and Std Dev, the standard deviation of PKA energy (keV). 98
4.10 Primary knock-on atoms energy spectrum for SiC. This energy spectrum was created by ROOT. The X-axis shows the energy of PKA in keV. The Y-axis shows the count number of PKA. The figure keys show: Entries, the total number of PKA; Mean, the average PKA energy in keV; and Std Dev, the standard deviation of PKA energy (keV). 98
4.11 Primary knock-on atoms energy spectrum for Ga_2O_3. This energy spectrum was created by ROOT. The X-axis shows the energy of PKA in keV. The Y-axis shows the count number of PKA. The figure keys show: Entries, the total number of PKA; Mean, the average PKA energy in keV; and Std Dev, the standard deviation of PKA energy (keV). 99
4.12 Primary knock-on atoms energy spectrum for GaN. This energy spectrum was created by ROOT. The X-axis shows the energy of PKA in keV. The Y-axis shows the count number of PKA. The figure keys show: Entries, the total number of PKA; Mean, the average PKA energy in keV; and Std Dev, the standard deviation of PKA energy (keV). 99

4.13 Primary knock-on atoms energy spectrum for $CsPbBr_3$. This energy spectrum was created by ROOT. The X-axis shows the energy of PKA in keV. The Y-axis shows the count number of PKA. The figure keys show: Entries, the total number of PKA; Mean, the average PKA energy in keV; and Std Dev, the standard deviation of PKA energy (keV). 100
4.14 Gamma-ray detection efficiency to γ-ray energy range from 0.5 MeV to 1.5 MeV versus semiconductor thickness for 300 keV LLD with optimal B_4C (top) and LiF (bottom) converter layer thickness for diamond. The optimal thicknesses for B_4C and LiF converter layer are 2.32 μm and 24.89 μm. 103
4.15 Gamma-ray detection efficiency to γ-ray energy range from 0.5 MeV to 1.5 MeV versus semiconductor thickness for 300 keV LLD with optimal B_4C (top) and LiF (bottom) converter layer thickness for SiC. The optimal thicknesses for B_4C and LiF converter layer are 2.32 μm and 24.89 μm. 104
4.16 Gamma-ray detection efficiency to γ-ray energy range from 0.5 MeV to 1.5 MeV versus semiconductor thickness for 300 keV LLD with optimal B_4C (top) and LiF (bottom) converter layer thickness for Ga_2O_3. The optimal thicknesses for B_4C and LiF converter layer are 2.32 μm and 24.89 μm. 105
4.17 Gamma-ray detection efficiency to γ-ray energy range from 0.5 MeV to 1.5 MeV versus semiconductor thickness for 300 keV LLD with optimal B_4C (top) and LiF (bottom) converter layer thickness for GaN. The optimal thicknesses for B_4C and LiF converter layer are 2.32 μm and 24.89 μm. 106
4.18 Gamma-ray detection efficiency to γ-ray energy range from 0.5 MeV to 1.5 MeV versus semiconductor thickness for 300 keV LLD with optimal B_4C (top) and LiF (bottom) converter layer thickness for $CsPbBr_3$. The optimal thicknesses for B_4C and LiF converter layer are 2.32 μm and 24.89 μm. 107

5.1 View of simulation model in LAMMPS and view of the spatial distribution of interstitial atoms evolving over time in $CsPbBr_3$. The red ball represents Br atom, the blue ball represent Pb atom and the yellow ball represents Cs atom. (a) represents the crystal structure of $CsPbBr_3$ before the simulation, while (b) to (e) illustrate the spatial distribution of interstitial atoms at a specific moment following the initiation of a cascade collision. 120

1 Neutron detection efficiency versus semiconductor material thickness with optimal B_4C converter layer thickness for diamond with LLD range from 100 keV to 900 keV. 147
2 Neutron detection efficiency versus semiconductor material thickness with optimal B_4C converter layer thickness for SiC with LLD range from 100 keV to 900 keV. 148
3 Neutron detection efficiency versus semiconductor material thickness with optimal B_4C converter layer thickness for Ga_2O_3 with LLD range from 100 keV to 900 keV. 149

4 Neutron detection efficiency versus semiconductor material thickness with optimal B_4C converter layer thickness for GaN with LLD range from 100 *keV* to 900 *keV*. 150

5 Neutron detection efficiency versus semiconductor material thickness with optimal B_4C converter layer thickness for $CsPbBr_3$ with LLD range from 100 *keV* to 900 *keV*. 151

6 Neutron detection efficiency versus semiconductor material thickness with optimal LiF converter layer thickness for diamond with LLD range from 100 *keV* to 900 *keV*. 152

7 Neutron detection efficiency versus semiconductor material thickness with optimal LiF converter layer thickness for SiC with LLD range from 100 *keV* to 900 *keV*. 153

8 Neutron detection efficiency versus semiconductor material thickness with optimal LiF converter layer thickness for Ga_2O_3 with LLD range from 100 *keV* to 900 *keV*. 154

9 Neutron detection efficiency versus semiconductor material thickness with optimal LiF converter layer thickness for GaN with LLD range from 100 *keV* to 900 *keV*. 155

10 Neutron detection efficiency versus semiconductor material thickness with optimal LiF converter layer thickness for $CsPbBr_3$ with LLD range from 100 *keV* to 900 *keV*. 156

Chapter 1

Introduction

Semiconductor neutron detectors play a crucial role in various fields, including nuclear energy, homeland security, and medical imaging. The development of these detectors has been driven by the need to accurately and efficiently detect neutrons, which are challenging to detect due to their neutral charge and lack of ionising capability. The use of semiconductor materials in neutron detection has shown promising results, particularly in the field of neutron imaging, their small size and thin profile make them convenient for use as pixel points in neutron imaging systems, and their low noise levels also facilitate easy integration into circuits.

One crucial factor that affects the detection efficiency of semiconductor neutron detectors is the thickness of the converter and semiconductor material used. The impact of the converter layer on detection efficiency is related to the absorption cross-section, the thickness of the converter layer, and the maximum allowable attenuation range of charged particles within the converter layer. This relationship has been studied, and for a given thickness of the converter layer, the probability of charged particles entering the active region can be calculated.

Merely obtaining the probability of charged particles entering the detector does not conveniently yield the optimal thickness of the converter layer. Furthermore, research on the optimal thickness of the semiconductor layer, especially regarding the optimal thickness for wide-bandgap semiconductors, is lacking. Additionally, in practical scenarios, it is unfeasible to determine the exact location of particle generation or the emission angle of charged particles at the point of their creation. This complexity also renders the direct application of theoretical formulas for deducing the optimal thickness of the semiconductor layer, as done for the converter layer, less straightforward. The growth of semiconductors is time and energy intensive. For instance, in the Metal-Organic Chemical Vapour Deposition (MOCVD) technique, depending on different operational parameters, the growth rate typically ranges from a few hundred nanometers to several micrometres per hour. Additionally, increasing the growth rate might lead to an increase in lattice defects, which can negatively impact the charge collection efficiency (CCE) and detection efficiency of the neutron detector. Therefore, it is crucial to know the minimum thickness that the semiconductor can achieve under a specific converter layer of a certain thickness. This is important for reducing growth time and cost, as well as for enhancing γ radiation resistance.

Finding the optimised thickness of the semiconductor material requires a thorough understanding of the physical processes involved in neutron detection and the properties of the semiconductor materials used.

Thermal neutrons mainly react with B and Li in the converter layer materials B_4C and LiF. Their reactions are demonstrated in Eq. 1.1 and Eq. 1.2:

$$^{10}B + n \rightarrow \alpha +^{7} Li + 2.31 \quad MeV \tag{1.1}$$

$$^{6}Li + n \rightarrow \alpha +^{3} H + 4.79 \quad MeV \tag{1.2}$$

The charged particles generated by the reactions produce ionisation as they move through the semiconductor material, resulting in the loss of energy of the charged particles. These charged particles have high energy levels, typically ranging in the MeV region. The process, known as electron or nucleus stopping of the target material, is affected by the thickness of the semiconductor material.

Initially, the optimised thickness of the semiconductor thin-film layer was assumed to be equal to the range of charged particles, such as α particles in the semiconductor material. However, upon comparing the calculation results obtained from The Stopping and Range of Ions in Matter (SRIM) software [ZZB10], it was discovered that the optimised thickness of the semiconductor is greater than the range of α particles in the semiconductor due to the contribution from other charged particles, such as ^{7}Li or ^{3}H. Given the complexity of mathematical modelling resulting from the addition of the converter layer, the Monte Carlo (MC) method based on statistical calculation can be used to determine the optimised thickness of the semiconductor in neutron detectors. The development of novel semiconductor materials and the optimisation of semiconductor thickness can enhance detection efficiency and simultaneously reduce fabrication time.

Addressing the aforementioned challenges, this thesis presents several innovative aspects in the field of neutron detection using non-directly detecting semiconductors. These innovations are as follows:

1. A theoretical method has been established to determine the optimal thickness of B_4C and LiF converter layers under various low-level discriminator (LLD) energy, and based on this method, computational software has been successfully developed.

2. A novel method has been established using the Monte Carlo approach to predict the optimal thickness of the semiconductor layer under specific conditions and with a particular converter layer. This method has been employed to predict the optimal thicknesses for five different materials (diamond, SiC, Ga_2O_3, GaN, and $CsPbBr_3$). This part of the research, excluding the research relating to $CsPbBr_3$, has been published in *Sensors* under the title "Comparison of Neutron Detection Performance of Four Thin-Film Semicon-

ductor Neutron Detectors Based on Geant4" [ZA21a].

3. Exploration of the threshold displacement energy (TDE) of $CsPbBr_3$ under various temperatures based on simulation results. A part of this research's results has been published in the *2021 IEEE Nuclear Science Symposium and Medical Imaging Conference (NSS/MIC) proceedings* under the title "Simulation of the Effect of Neutron Radiation on the Caesium Lead Bromide" [ZA21b].

4. A systematic study of the micro-radiation processes of the aforementioned five materials, including neutron and γ radiation, has been conducted. The displacement per atom (DPA) values of these five materials were obtained to assess their micro-radiation resistance. For different γ-ray energies, the maximum growth thicknesses that these five materials can achieve for the optimal neutron-γ signal discrimination were also determined.

In summary, this thesis offers valuable guidance for the design and selection of radiation-resistant semiconductor neutron detectors. This research will emphasise the potential for future advances in semiconductor neutron detectors and lay the theoretical foundation for upcoming research at Lancaster University.

Chapter 2

Background

With the continuous progress in the exploration of micro-particles, the scope of applications of these diminutive entities is expanding. Neutrons, being one of the fundamental microscopic particles, have long been the focus of research. Neutrons have found diverse applications in fields such as nuclear reactors, medical treatment, neutron imaging and cosmic ray exploration. The scope of neutron applications reveals the complexity of the neutron detection environment, which in turn presents challenges to the development of neutron detectors.

The Fukushima nuclear power plant accident in 2011 brought about a plethora of issues, including the critical problem of placing a neutron detector inside the stricken reactor for radiation monitoring to ensure that the reactor will not become critical again. Moreover, some second-generation nuclear power plant technologies have been in use for over 60 years, and are currently facing decommissioning.

Hence, there is a need for the development of in-reactor neutron dose detection technology that is accurate and safe. Apart from nuclear fission technology, the available deuterium (D) and tritium (T) fusion technology emit a substantial number of neutrons [Law57], thereby requiring more advanced neutron detection technology for their detection. Detecting and shielding against cosmic radiation is crucial for spacecraft development, thereby requiring neutron detectors to be employed in high-energy outer space radiation fields. Furthermore, the development of high-resolution neutron imaging systems also necessitates the use of neutron detectors with a smaller volume.

In summary, there is a pressing need to develop small-sized, low power-consuming, and robust neutron detectors capable of functioning in extreme environments with high temperature, high radiation, and high pressure.

2.1 Neutrons

This part delves into the concept and properties of neutrons, the focus of which began when Sir Ernest Rutherford, a British physicist, who first introduced the idea of the neutron in the early 1920s. It was not until 1932, when James Chadwick bombarded a beryllium target with a source of alpha particles, that the existence of neutrons was experimentally confirmed. Since then, research on neutrons has been ongoing, as shown in Fig. 2.1.

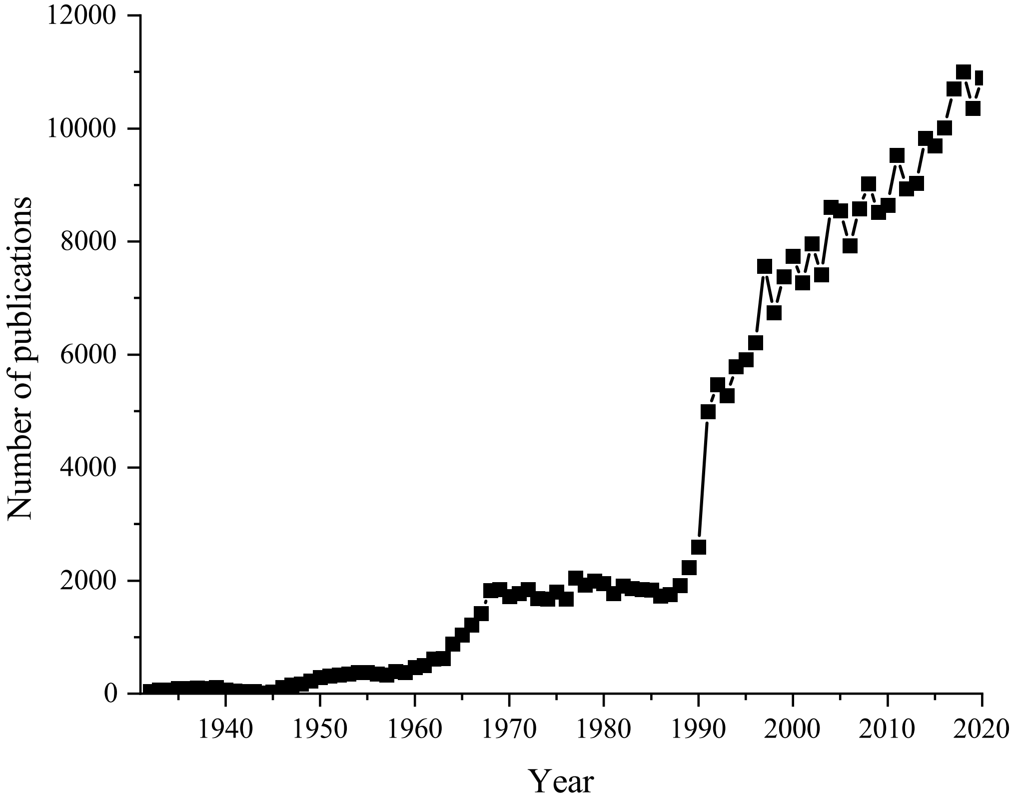

Figure 2.1: Number of papers on neutron research as a function of year, based on Web of Science data spanning from 1932 to 2020.

The neutron has a mass of $1.674927471(21) \times 10^{-27}$ kg [MNT16], slightly more massive than the proton, which has a mass of $1.672621637(83) \times 10^{-27}$ kg. The neutron's spin is $\frac{1}{2}$, and as a free neutron is an unstable particle, it has an average lifetime of 877.75 seconds [GFCW$^+$21] and a half-life about 611.0 ± 1.0 seconds. Neutrons follow the Fermi-Dirac distribution and the Pauli exclusion principle, similar to other particles. While the neutron was previously classified as a member of elementary particles, it is now understood, under the current Standard Model theory, to consist of two down quarks and one up quark, making it a composite particle.

In order to keep the baryon number conserved within the framework of the Standard Model, the only possible decay path for a neutron is for one of the quarks to change its flavour through weak force. The neutron consists of three quarks; two down quarks ($\frac{-1}{3}e$ charge) and one up quark ($\frac{+2}{3}e$ charge). A down quark can decay into a lighter up quark, releasing a $W^{\pm}$ boson. Consequently, a neutron can decay into a proton, releasing an electron and an antineutrino.

Neutrons can exist in an aggregated state in neutron stars, the densest stars after black holes. When the mass of the star reaches eight to 30 times the mass of the Sun, a supernova explosion occurs at the end of the star's evolution, produced by the collapse of gravity. The star collapses to form a star between a white dwarf and a black hole, which is many times denser than any matter on Earth. Besides neutron stars, there is evidence to suggest that neutrons can also exist in a tetraneutron state [DAG$^+$22]. Figure 2.2 shows the experimental principle for searching for the tetraneutron.

Neutrons can be classified according to their energy into supercool neutrons, cold neutrons, thermal neutrons, epithermal neutrons, and fast neutrons. Supercool neutrons have very low energy, with an energy range of less than 0.001 eV, typically obtained by slowing them down at extremely low temperatures. Cold neutrons have an energy range between 0.001 eV and 0.025 eV, usually obtained using low-temperature materials such as liquid hydrogen or helium to slow them down. Thermal neutrons are neutrons that have reached thermal equilibrium with their environment, with an energy of approximately 0.025 eV, corresponding to the thermal motion energy of gas molecules at room temperature (25^oC). Epithermal neutrons have higher energy than thermal neutrons but lower than fast neutrons, with an energy range between 0.025 eV and 10 keV. They can be generated in reactors or accelerator-based neutron sources and are often used in Boron Neutron Capture Therapy (BNCT). Fast neutrons have high energy, with an energy range greater than 10 keV, and are typically produced in nuclear fission or fusion processes. They have ionising power and can penetrate deeply into matter. These classifications help in understanding the behaviour and applications of neutrons in different physical and engineering contexts.

Neutrons are the only type of matter that can cause radioactive ionising radiation in other substances, known as neutron activation, which is widely used in medicine, academia, and industry to produce radioactive substances. Fast neutrons can travel very long distances through air, so neutron radiation needs to be shielded or moderated by substances rich in hydrogen nuclei, such as concrete and water. Nuclear reactors are a common source of neutron radiation, and water is used as an effective neutron moderator for a pressurised water reactor (PWR).

Atoms are complex systems composed of negatively charged electrons orbiting around a positively charged nucleus. Both charged particles (e.g., protons, electrons, or ions) and electromagnetic waves (e.g., γ rays) dissipate energy as they penetrate matter. Charged particles slow down, and electromagnetic waves are absorbed by the materials they traverse. However, neutrons are only influenced by strong or weak interactions when close to the nucleus. This is because, unlike other subatomic particles, neutrons are uncharged due to the cancellation of the electric charges of down and up quarks. Consequently, they can penetrate matter over substantial distances without being affected by external electromagnetic forces until they collide directly with a nucleus. Since nuclei are small compared to the atom, the likelihood of such collisions is exceedingly low. Free neutrons can remain unchanged over extended distances until they collide with a nucleus, making them highly penetrating and impervious to direct observation. The reactions of free neutrons with atomic nuclei can be classified into elastic and inelastic scattering. Elastic scattering refers to collisions where the neutron interacts with the atomic nucleus without causing any changes in the internal structure of the nucleus. In this type of collision, the total kinetic energy of the neutron and the atomic nucleus remains constant, although the direction of the neutron may change. Inelastic scattering refers to collisions where the neutron interacts with the atomic nucleus and causes changes in the internal structure of the nucleus. In this type of collision, the neutron transfers some of its energy to the nucleus, putting it into an excited state. The excited nucleus then returns to its ground state by emitting γ rays. Inelastic scattering also includes other nuclear reactions, such as capture reactions, fission reactions, (n, α) reactions, and (n, p) reactions.

The impossibility of accelerating, decelerating, or binding neutrons with electromagnetic fields, coupled with the weak magnetic moment of free neutrons, makes it challenging to control them. The only effective way to control their motion is by using the nuclear force, which involves placing stacks of nuclei in the neutron's path to absorb them. Such a reaction, where neutrons hit the nucleus of an atom, plays an important role in nuclear reactions.

Based on the introduction above, in contrast to charged particles like α and β particles, alternative methods must be adopted to detect neutrons. These methods can primarily be categorised into nuclear reaction, nuclear recoil, neutron activation, and nuclear fission techniques.

The principle of the nuclear reaction method is that through the nuclear reaction between neutrons and the nuclei of target materials, secondary charged particles are produced. Detectors are then used to detect these secondary charged particles, thus achieving indirect detection of neutrons. Common thermal neutron nuclear reaction materials are ^{6}Li, ^{10}B, and ^{3}He. The $^{6}\mathrm{Li}(n, \alpha)$ reaction releases the most energy among the three reactions, providing the best n/γ discrimination ratio. However, Li does not have suitable gaseous compounds and can only be used in solid form. The $^{10}\mathrm{B}(n, \alpha)$ reaction is the most widely used because boron materials are readily available. To improve detection efficiency, enriched boron is commonly used in neutron detector fabrication. The $^{3}\mathrm{He}(n, p)$ reaction has the largest cross-section among the three, but its acquisition cost is relatively high.

The nuclear recoil method utilises the elastic collision between neutrons and atomic nuclei. The charged atomic nuclei will produce ionisation in the detector, and the detection of the resulting electric current allows for the capture of neutron signals. This method is primarily used to detect fast neutrons. According to the conservation of energy and momentum, the smaller the mass of the recoil nucleus, the greater the energy it gains. Therefore, H is commonly used as the detection material in the nuclear recoil method, also known as the recoil proton method. After scattering, the energy and emission direction of the recoil proton can be calculated using the conservation of energy and momentum.

The nuclear fission method is similar in principle to the nuclear reaction method. The difference lies in the utilisation of fission reaction fragments that cause ionisation within the detector, thereby detecting neutrons through the observation of nuclear fission fragments. The expression for this method is (n, f). This method is primarily used to measure neutron flux. Additionally, due to the high energy of fission fragments, this method can be applied in environments with high γ-ray backgrounds.

The last method is the neutron activation method, with radiative capture as the main reaction process. This technique involves irradiating a suitable target with neutrons, converting the nuclei in the target into excited compound nuclei. The compound nucleus quickly de-excites to its ground state by emitting one or more photons. This process of neutron capture and subsequent γ radiation emission is called radiative capture, denoted as (n, γ). By detecting the radioactivity of the activated target, neutrons can be indirectly detected.

In summary, the properties of neutrons make neutron detection challenging. Typical neutron detectors comprise gas detectors, scintillator detectors, and semiconductor detectors. The following section covers part of them in detail.

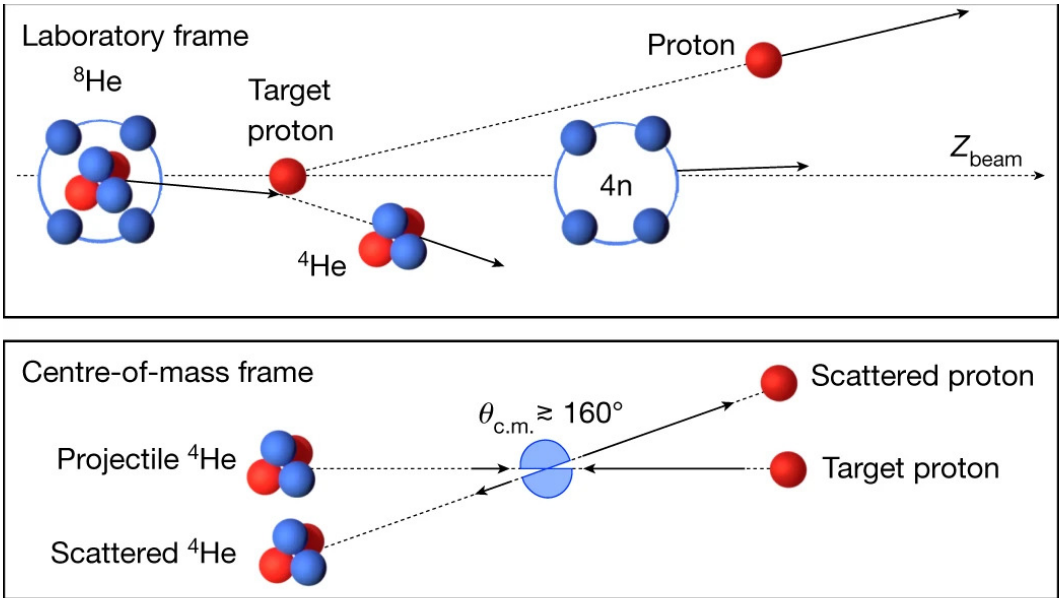

Figure 2.2: Top: quasi-elastic scattering of the ^{4}He core from a ^{8}He projectile off a proton target in the laboratory frame. The length of the arrows represents the momentum per nucleon (the velocity) of the incoming and outgoing particles. Bottom:the equivalent proton-^{4}He elastic scattering in their centre-of-mass frame. [DAG$^+$22]

2.2 Neutron detectors

2.2.1 Gas detectors

Proportional counting tubes

The most commonly used method for measuring neutrons is via boron trifluoride (BF_3) gas-filled proportional counter tubes, which have a similar structure to the Geiger-Muller (G-M) tube used for measuring γ rays. The tube is able to detect thermal neutrons by generating ion pairs in the counting tube through the ^{10}B$(n, \alpha)^7$Li reaction, and amplifying the output signal through the gas. It can also record fast neutrons with a paraffin or High-density polyethylene (HDPE) moderator placed outside the tube to thermalise neutrons before detecting them.

Boron ionisation chamber and fission chambers

Boron ionisation chambers and fission chambers are essential control components in current reactors. They are used to measure the thermal neutron flux. The thermal neutron flux in the reactor is directly proportional to the reactor power, allowing this detector to monitor the start-up and operation of the reactor.

An electrode in the ionisation chamber is coated with a film containing concentrated ^{10}B. When a neutron collides with the boron membrane, α particles and ^{7}Li nuclei are generated via the ^{10}B$(n, \alpha)^7$Li reaction. These charged particles then ionise the gas, and the incident neutron flux is determined by recording the ionisation current they produce.

When the electrode of the ionisation chamber is coated with uranium-235 (^{235}U), a fissile material, neutrons can be detected as well by recording the ionisation of fission fragments.

2.2.2 Scintillator detectors

Prior to the 1950s, gas detectors were predominantly used for neutron detection. However, with the advent of scintillation technology, scintillator detectors have become the most commonly used neutron detectors. The reason for this is that neutron measurements are generally obtained indirectly through nuclear reactions, and the penetrating power of neutrons is significantly greater than that of charged particles and γ rays, thereby making it challenging to improve the detection efficiency of neutron detectors. The advantageous features of scintillation detectors, such as their high efficiency and fast time response, make them very useful for enhancing the efficiency and increasing the counting rate.

However, the front end of scintillator detectors is typically larger than that of semiconductor detectors, and their performance in strong mixed radiation fields and high-temperature environments is less than ideal.

Zinc sulphide activated with silver

Zinc sulphide activated with silver, ZnS(Ag), has different compositions for detecting fast neutrons and thermal neutrons. The most commonly used fast neutron scintillator is a mixture of ZnS(Ag) powder and plexiglass that is pressed into a cylindrical shape at a high temperature. The working principle of this scintillator is that recoil protons produced by fast neutrons in the plexiglass make ZnS(Ag) scintillation light, which is transmitted through the plexiglass.

For detecting thermal neutrons, a scintillator made of a mixture of ZnS(Ag), glycerin, and boric acid is commonly used. This mixture is pressed and sealed in an aluminium (Al) box with a plexiglass lid. The reaction of $^{10}\mathrm{B}(n,\alpha)^{7}\mathrm{Li}$ produces α particles and $^{7}\mathrm{Li}$, which make ZnS(Ag) emit light.

Lithium glass scintillators

The lithium (Li) glass scintillator is composed of cerium-activated Li glass, with a composition of $\mathrm{LiO_2}$-$2\mathrm{SiO_2}$(Ce). It utilises T and α particles produced by the $^{6}\mathrm{Li}(n,\alpha)\mathrm{T}$ reaction to produce scintillation light.

Organic scintillators

All organic scintillators are hydrocarbons and contain a large number of hydrogen atoms and can be used for fast neutron detection. Fast neutrons hit the hydrogen nuclei and generate recoil protons by neutron-proton elastic scattering. The recoil protons cause the characteristic fluorescence of the scintillator, these photons are detected via a photomultiplier tube (PMT), which is a sensitive device that detects and amplifies low light levels. Photons enter the PMT and interact with the photocathode, releasing primary electrons through the photoelectric effect. These electrons are accelerated towards a series of dynodes, where they generate secondary electrons through secondary emission. This electron multiplication process amplifies the initial signal, producing an electrical current at the anode. The gain of PMT depends on the number of dynodes and applied voltage.

Another common feature of organic scintillators is that the luminescence decay time is short, so it can be used for high-intensity neutron flux measurements. In the time-of-flight (TOF) method for producing a fast neutron energy spectrum measurement, an organic scintillator with a fast light emission time is currently the only detector available.

The scintillation light output produced by electrons and heavily charged particles in organic scintillators is different. Appropriate pulse shape discrimination techniques can be used to distinguish neutron pulses from γ-ray pulses. Therefore, organic scintillators can measure neutrons in the presence of a strong γ-ray background. Organic scintillators currently used include anthracene crystals, plastic scintillators, and liquid scintillators.

2.2.3 Semiconductor detectors

Semiconductor detectors are characterised by small size, fast response, and high energy resolution. Thin semiconductors exhibit a low sensitivity to γ rays and can be optimised to provide an almost 100% intrinsic efficiency for charged particles. Silicon detectors have been used in this way for decades.

However, it is important to note that most silicon-based (Si) semiconductor detectors struggle to withstand radiation damage. The performance of Si-based semiconductor detectors can degrade rapidly when exposed to high γ-ray background or high-flux neutron detection environments [LZYO19].

In summary, the most commonly used neutron detectors prioritise detection performance over their ability to tolerate extreme environments. Due to the intrinsic properties of Si, ZnS and Li-based glasses, their detection performance will decrease sharply as the temperature or the radiation intensity increases. These detectors are not suitable for extreme environments where high temperature, high pressure and strong radiation fields are prevalent, such as in nuclear reactor cores, high-energy physics experimental environments, and deep space. New types of semiconductor neutron detectors should be able to operate in environments with neutron fluxes of at least 10^{12} $neutrons/cm^2 \cdot s$ without significant performance degradation.

2.3 Wide-bandgap semiconductor materials for neutron detection

The development of nuclear fusion, new generation nuclear fission reactors, and outer space nuclear technology is closely linked to neutron detector research. However, the extreme and complex environments presented by such scenarios pose significant challenges to neutron detectors, including high-intensity radiation fields, high temperatures, high pressures, and corrosive conditions. To address these challenges, more advanced neutron detectors are needed that can withstand use in extreme environments. Several semiconductor materials, such as diamond, SiC (silicon carbide), Ga_2O_3 (gallium oxide), and GaN (gallium nitride) are emerging as potential neutron detection materials due to their wide band gap, high breakdown voltage, small dark current, fast carrier mobility speed, considerable carrier drift distance, and higher thermal conductivity. These materials are excellent candidates for neutron detection in extreme environments. Research on these materials will help accelerate the production of new semiconductor neutron detectors to meet the demands of evolving nuclear technologies.

2.3.1 Diamond

The diamond detector has a wide band gap (5.5 eV), high melting point (4373°C at 127 $kbar$), strong radiation resistance, and a one hundred-hour service life under high neutron flux [WMBC15, PAM+16]. Most diamond detectors are used for X-ray detection, fusion neutron flux detection, and space detection technology [BTM+01]. In the past, the main problem that limited the application of diamond detectors was cost. Now, with the continuous maturity of Chemical Vapor Deposition (CVD) and Metal-Organic Chemical Vapor Deposition (MOCVD) technology, the cost of detector-grade diamond has dropped, laying the foundation for the widespread application of diamond detectors.

Radiation resistance studies of CVD diamond, which irradiate the material with photons, protons, pions, and α particles, demonstrate that its signal collection properties do not change with photons up to 10 $Mrad$, protons up to 5×10^{13} cm^{-2}, and pions up to 8×10^{13} cm^{-2} [BBC+95]. It indicated that diamond detectors could be used in an extreme environment with a practical service life. A 2006 study reported a ^{6}LiF-diamond detector with 100% charge collection efficiency (CCE) and approximately 1.5% energy resolution for alpha particles [MMP+06].

In 2016, a pixelated instrument, consisting of 12 independent Single-crystal Diamond Detector (SDD) matrices, was developed called the Diamond Vertical Neutron Spectrometer (DVNS). The process and results of using DVNS to obtain a 2.5 MeV neutron spectrum in the deuterium plasma of the Joint European Torus (JET) were also introduced [MGN$^+$16]. Furthermore, compared with Si photodiodes, single-crystal diamond diodes have better fast neutron time resolution [VVRP$^+$18]. In the same year, the thermal neutron and γ-ray detection performance of a diamond detector with a LiF converter layer was studied [LCZ$^+$19], which further verified the thermal neutron detection capability and γ-ray rejection capability of the detector. A study of the relationship between the detection performance of diamond and the quality of crystal showed that the CCE of diamond is affected by the quality of the crystal and the dislocation density [SHZ$^+$21].

A study of the performance of diamond detectors in a high-temperature environment showed that diamond can work properly in spectrometric mode at temperatures up to $240°C$ with energy resolution (FWHM) of about 3.5% [PAP$^+$16]. In addition to a diamond detector with a LiF converter layer, the thermal neutron detection performance of PIN diamond diodes using a boron nitride (BN) converter layer was reported [HBK$^+$20]. In recent studies, a real-time thermal neutron measurement in a nuclear fusion reactor using SDD was reported. They used a new pulse shape discrimination technology to distinguish thermal neutron signals from energetic ions and γ-ray signals in nuclear fusion plasma [KAY$^+$20].

2.3.2 Silicon carbide

SiC has many good characteristics that make it suitable for neutron detection. What is more, SiC has a similar processing technology to that of Si integrated circuits and so can be adopted quickly.

Research on using SiC to detect neutrons started in 1999. It demonstrated that SiC detectors could work properly under high neutron flux [SDR+99]. However, neutron irradiation will create defects which will affect the CCE of SiC. In 2005, the CCE of SiC Schottky diode with a β source was studied. The results showed that SiC has high CCE for β-particles [MSP+05]. There was a study which gave the performance comparison at room temperature between SiC and diamond under a 14 MeV neutron flux [OOK+18]. This study indicated that diamond had a higher count rate than SiC. However, it is worth noting that this is not a normalized comparison, and the active volume of SiC was limited to 21 μm. Simulations on SiC PN diodes have been reported [MPA+19] and showed that the SiC PN diode with a B_4C converter layer has about 4% neutron detection efficiency.

In 2020, a study of the thermal neutron irradiation influence on structural and electrical properties of n-4H-SiC and n-Al/n-4H-SiC Schottky contacts was reported [VSM+20]. This study indicated that the neutron irradiation would affect the electrical properties of the 4H-SiC detector, especially for n-Al/n-4H-SiC Schottky contacts. Both Schottky and ohmic contacts are used to improve the performance of a novel SiC-based strip sensor. The spectrum obtained by the detector shows clear α-particle events produced by neutron conversion products; α-particles and tritons can be identified clearly from the spectrum obtained by the detector [SPP+20]. SiC can be used as near-core neutron flux detectors owing to its strong radiation resistance capability [KTS+20]. A radiation resistance capability comparison between Si and 4H-SiC was conducted [HSVM20]. It demonstrated that due to the lower thickness and high doping level, 4H-SiC is a more reliable device than Si in a radiation environment.

2.3.3 Gallium oxide

Ga_2O_3 is a WBG semiconductor material with a band gap of approximately 4.8 eV, a theoretical breakdown field strength of 8 MV/cm, and electron mobility of 300 $cm^2/V \cdot s$. The Baliga figure-of-merit of β-Ga_2O_3 is four times that of GaN, ten times that of SiC, and 3444 times that of Si. Moreover, large-size β-Ga_2O_3 with low defect density ($10^3\ cm^{-2} \sim 10^4\ cm^{-2}$) can be obtained by growing it on a sapphire substrate, thereby lowering the cost of β-Ga_2O_3 devices as compared to GaN and SiC devices.

The crystal structure of β-Ga_2O_3 was studied as early as 1960 [Gel60]. A 2019 study investigated induced defects in β-Ga_2O_3 Schottky diodes under high-energy neutron radiation [FCB+19]. The results showed that high-energy neutron irradiation can reduce the number of carriers and have primary effects on the conduction band energy (Ec), which increases the concentration of a state at -2.00 eV and introduces a state at -1.29 eV. In addition, it was found that the neutron detection performance of Ga_2O_3 can be improved by doping modest concentrations of boron rather than high concentrations of boron to reduce defects in the material [LLR20]. An increase in boron doping in Ga_2O_3 increases the likelihood that boron atoms will collide with gallium or oxygen atoms and cause them to leave the lattice, creating defects. Monte Carlo (MC) simulation results for Ga_2O_3, however, show that Ga_2O_3 with a converter layer has a higher neutron detection efficiency than boron-doped Ga_2O_3 [BY20]. The relationship between neutron irradiation and defect concentrations and the anneal temperature influence on defect distribution in Ga_2O_3 were presented in a 2020 study on Ga_2O_3 deep-level defects [GMK+20]. Such work is essential in controlling the electric properties of Ga_2O_3. Finally, a recent study presented a novel thin-film based neutron detector, comprising $CsPbBr_3$, Ga_2O_3, and a converter layer, which showed a new research direction for using Ga_2O_3 in neutron detection [FIRBM+20].

2.3.4 Gallium nitride

GaN, with the biggest band gap among all commercial semiconductors, is a third-generation semiconductor material that has shown potential for near-core neutron detection [WMBC15].

In addition to its aforementioned characteristics, GaN has a very stable chemical property. It can be grown on various substrates such as aluminum nitride (AlN) [ASM$^+$10], Si [DPR$^+$03], sapphire [PFW$^+$07], and SiC [RFS$^+$00]. In 2014, a BGaN detector with good α-particle sensitivity and low γ-ray sensitivity was demonstrated, exhibiting good detection performance under high radiation conditions [AIM$^+$14]. A review of using GaN for ionisation detection was presented in 2015 [WMBC15], while in 2017, a bulk GaN α-particle detector with improved energy resolution under a bias of 550 V was reported [XMW$^+$17], indicating that GaN could have high energy resolution for neutron detection.

The radiation hardness of a PIN GaN-based α-particle detector was tested under 10 MeV electrons, and the result showed that the detector could be used for α-particle detection under a high-dose electron flux of up to 200 kGy [ZZT$^+$18]. Furthermore, the high-temperature performance of the same detector was tested [ZZL$^+$18], revealing that the detector's working temperature could reach 450 K. A GaN neutron detector with LiF was fabricated in 2020, exhibiting a neutron detection efficiency of about 1.9% under a 0 V bias [ZSZ$^+$20]. Studies on using GaN for fast neutron detectors [SVSN20] and boron neutron capture therapy (BNCT) monitors [GMMW15, GGMW19] have also been conducted. In the same year, compared to LiF converter layers, GaN with a B_4C converter layer was reported to have higher neutron detection efficiency [ZA20].

In addition to layered structures, ion-implanted GaN detectors have been investigated [SRX$^+$19]. Recent research has explored growing GaN on nitrogen-doped single layer graphene (n-SLG) substrates [SKRK20], demonstrating that high electron contents in GaN can be achieved using this approach, which could facilitate the fabrication of superior GaN devices. The short carrier lifetime in GaN makes it challenging to measure the CCE accurately. A recent study has reported on a simplified simulation of GaN CCE using the Hecht equation, as well as on the effect of carrier lifetime on CCE under neutron irradiation [ZA22].

2.3.5 Summary

Table 2.1 presents the properties of different materials: Diamond, SiC, Ga_2O_3, and GaN. It includes key properties such as bandgap, density, melting point, electron drift velocity, and hole drift velocity.

Table 2.1: Material properties of four semiconductors for radiation detection at 300 K [WMBC15].

Property	Diamond	4H-SiC	Ga_2O_3	GaN
Bandgap (eV)	5.5	3.23	4.8	3.39
Density (g/cm^3)	3.515	3.211	5.88	6.15
Melting point (^oC)	4373 (at 125 $kbar$)	2857 (at 35 atm)	1725	2500
Electron mobility ($cm^2/V \cdot s$)	1800∼2200	800∼1000	300	1000
Hole mobility ($cm^2/V \cdot s$)	1200∼1600	50∼150	1.3 (undoped)	30

2.4 Converter layer

A semiconductor detector with a layered structure utilises the nuclear reaction method for detecting atoms. In neutron research, the concept of a reaction cross-section is often introduced to describe the likelihood of a neutron interacting with a substance. The unit for the microscopic reaction cross-section is the barn, with 1 barn equating to ($10^{-24}\ cm^2$). Common semiconductor materials such as silicon, as well as wide-bandgap (WBG) semiconductors like gallium nitride (GaN) and diamond, have low thermal neutron ($0.025\ eV$) reaction cross-sections. Consequently, the probability of reactions is minimal, which leads to the challenge of directly using semiconductors to generate a significant thermal neutron detection signal. Due to this, a converter layer is incorporated within the layered structure of the semiconductor detectors. This converter layer consists of materials with a substantially higher thermal neutron reaction cross-section, such as boron (B), lithium (Li), gadolinium (Gd), and others.

Once the neutrons are moderated and hit the converter layer, there is a possibility that they will initiate a nuclear reaction with the atoms within this layer, resulting in the emission of secondary charged particles. These charged particles have a certain initial kinetic energy, and if they are emitted in an appropriate direction, they will enter the semiconductor layer. In the semiconductor layer, they lose energy through Coulomb scattering, producing a columnar ionisation of high-density plasma in the form of electron-hole pairs. The semiconductor detector then operates under a bias voltage, which serves to separate the produced electron-hole pairs and to move the charges to the corresponding electrodes. As the charges move within the detector's electric field, each one induces a charge in the external circuit. By integrating and measuring this with electronic devices such as pre-amplifiers and main amplifiers, the relevant information regarding the neutrons can be obtained.

2.4.1 Materials

As mentioned previously, various materials are used as converter layers in semiconductor neutron detectors. However, the converter layer introduces a new issue for neutron detection. As it absorbs neutrons, the secondary particles can also undergo ionisation within the converter layer, expending part of their energy. This reduces the ionisation energy of the secondary particles in the semiconductor layer, which is detrimental to detecting these charged particles. This issue is particularly significant when a Low-Level Discriminator (LLD) is introduced to shield against the energy of γ rays in the environment. Since incident radiation is typically a mixture of neutrons and γ rays, separating these is crucial for a reliable neutron detector and using an LLD is one way to achieve this. However, if the converter layer is too thin, it will not produce a sufficient number of secondary charged particles for detection. Therefore, finding a balanced or optimal thickness for the semiconductor converter layer is important.

In the research presented in this thesis, there is a particular focus on boron carbide (B_4C) and lithium fluoride (LiF) as materials for the neutron converter layer.

Boron carbide

Boron carbide (B_4C) is a ceramic material of exceptional merit, garnering attention in numerous high-end application domains due to its distinctive properties. Boron-10 (^{10}B), a stable isotope of boron, accounts for approximately 20% of the natural abundance of boron and significantly augments the application potential of boron carbide as a neutron absorber because of its presence.

The density of B_4C is around 2.52 g/cm^3. This density, along with the high thermal neutron cross-section of ^{10}B (3848 ± 40 b [SBB60]), bestows upon it superior neutron absorption capability, rendering it an optimal choice for control rods in nuclear reactors and neutron shielding materials [GVK+22]. The reaction between ^{10}B and thermal neutrons is shown in Eq. 2.1. It boasts an exceedingly high melting point of about 2450^oC, which ensures that B_4C remains stable under extreme temperature conditions, thus becoming a preferred material for the manufacture of high-temperature furnaces and refractory materials [GVK+22].

$$
{}^{10}\mathrm{B} + n \rightarrow \begin{cases} 6\%: & {}^{7}\mathrm{Li}(1.015\,\mathrm{MeV}) + \alpha(1.777\,\mathrm{MeV}), \\ & Q = 2.792\,\mathrm{MeV}\ \text{(to ground state)} \\ 94\%: & {}^{7}\mathrm{Li}^{*}(840\,\mathrm{keV}) + \alpha(1.470\,\mathrm{MeV}), \\ & Q = 2.310\,\mathrm{MeV}\ \text{(1st excited state)} \end{cases} \tag{2.1}
$$

B_4C exhibits remarkable chemical stability. It is inert to water and most acids at room temperature and also demonstrates good resistance to both oxidising and reducing agents [GVK+22]. This chemical inertness allows B_4C to retain its functionality in chemically aggressive environments, fulfilling the requirements of specific industrial applications.

Regarding hardness, B_4C is among the hardest materials known, ranking just below diamond. This quality makes it an ideal candidate for the production of abrasives, cutting tools, and ballistic materials [DRHC11].

In summary, B_4C, with its high density, elevated melting point, chemical stability, exceptional hardness, and superior neutron absorption capacity, plays an indispensable role across various high-technology fields.

Lithium fluoride

Lithium fluoride (^{6}LiF) is a material that has garnered widespread attention for its applications in the field of neutron detection. This material exploits the high cross-section of the ^{6}Li isotope for thermal neutrons (about 940 ± 4 b [FR16]), producing α particles and tritium (T) through neutron capture reactions, thereby enabling effective neutron detection [MAC+22]. The reaction between ^{6}Li and thermal neutrons is shown in Eq. 2.2.

Due to lithium's high chemical activity, the stable isotope salt ^{6}LiF is typically preferred over pure ^{6}Li. For the fabrication of neutron converters, i.e., depositing thin layers of ^{6}LiF onto an appropriate substrate, vacuum evaporation techniques are commonly employed. This method, along with a newly developed chemical deposition process, is detailed in the literature, with the respective advantages and disadvantages discussed [MAC+22].

$$^6\mathrm{Li} + n \rightarrow^3 \mathrm{H}(2.73\,\mathrm{MeV}) + \alpha(2.05\,\mathrm{MeV}), \quad Q = 4.78\,\mathrm{MeV} \tag{2.2}$$

In terms of neutron detection, ^{6}LiF has proven to be an effective material. For instance, when combined with ZnS(Ag), ^{6}LiF can be used to create a scintillation counter-based neutron detector, with its detection efficiency and resolution both simulated and validated [BLT+22]. Additionally, ^{6}LiF can be combined with other materials such as gadolinium-yttrium-aluminum-gallium garnets (GYAGG) based phosphors to form composite scintillation screens for neutron detection. This composite material has shown sensitivity and γ ray background rejection comparable to the widely used ZnS/^{6}LiF screens, but with a response time that is 40 times faster [FKA+22].

Recent studies have also developed thermal neutron radiation detectors based on ZnO-^{6}LiF/polystyrene composite materials. This composite material has demonstrated a significant response under neutron radiation sources, indicating its potential applications in the field of neutron detection [SPD23].

In summary, ^{6}LiF has attracted attention for its outstanding performance in the domain of neutron detection, exhibiting high potential both as a pure material and in combination with other materials.

2.4.2 Optimal thickness

An optimal converter layer thickness was sought to be identified, as previously mentioned, with the aim of achieving maximum efficiency in semiconductor neutron detection. Research on converter layers primarily composed of ^{10}B was first conducted in 1996 [MLBO96].

The study was initiated with detectors made of gallium arsenide (GaAs), which were equipped with a ^{10}B converter layer, and the effect of variations in the converter layer thickness on neutron detection efficiency was examined.

It is illustrated in Fig. 2.3 that there exists a probability for particles to be emitted in various directions once generated within the converter layer. Hence, a solid angle problem is presented in the calculation, and it is assumed that the

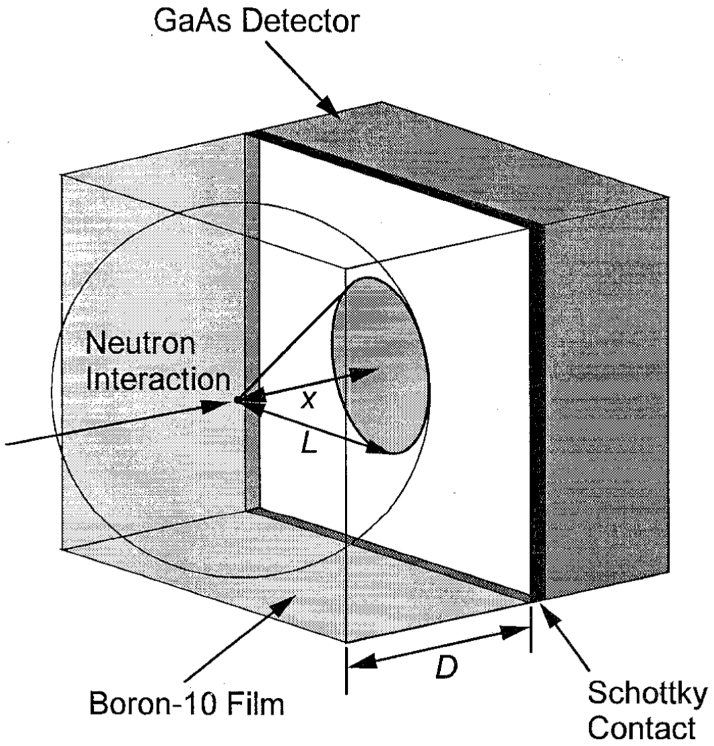

Figure 2.3: The probability of the reaction products entering the detector is a function of the solid angle and the maximum allowable range (L) [MLBO96].

system becomes isotropic after the entry of neutrons into the converter layer.

As the neutron beam penetrates further into the converter layer, a decrease in its intensity is observed, as depicted in Eq. 2.3 and Fig. 2.4.

$$I(x) = I_0 e^{-\Sigma(D-x)} \tag{2.3}$$

Here, I_0 represents the intensity of the neutron beam prior to reaching the converter layer, D denotes the thickness of the converter layer, x indicates the interaction depth from the contact, and the remaining term corresponds to the macroscopic absorption cross-section.

The impact of the interaction depth within the converter layer on detection

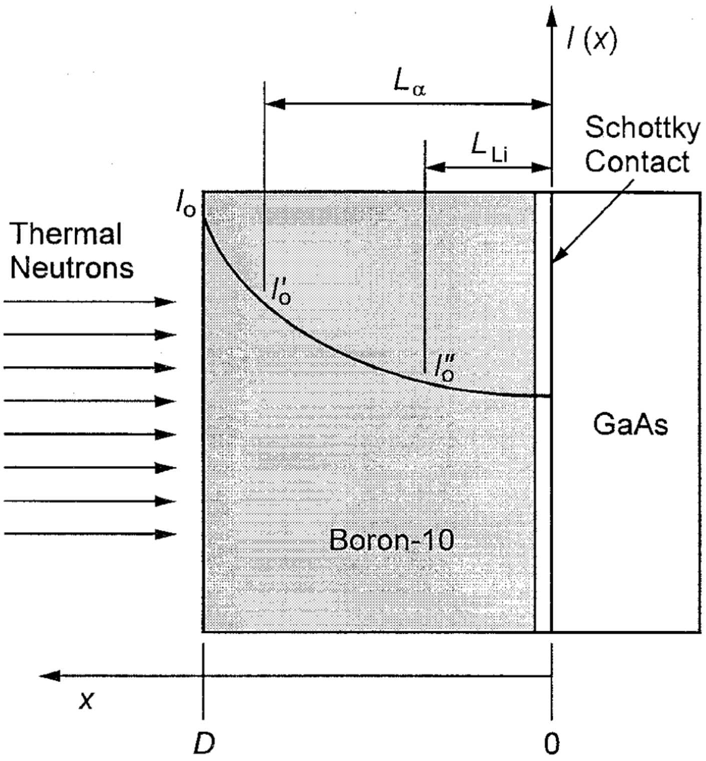

Figure 2.4: The initial thermal neutron intensity (I_0) is reduced by absorption in the ^{10}B film thickness is greater than the maximum allowable attenuation range (L) of either or both particles, the initial beam I_0 will be reduced before reaching the sensitive region. Depicted is the case in which the film is greater than both the alpha particle attenuation range (L_α) and the Li ion attenuation range (L_{Li}). Hence the beam intensity is reduced to I_0' at L_α and I_0'' at L_{Li} [MLBO96].

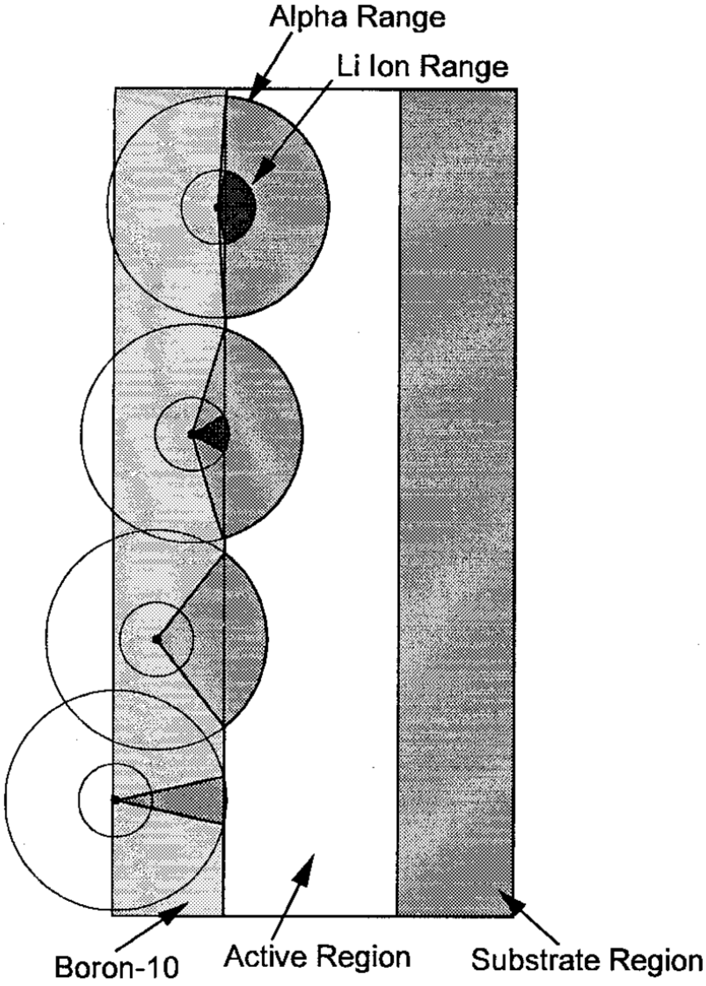

Figure 2.5: Events occurring near the contact have a very high probability that one of the reaction products will enter the detector. The probability diminishes as the reactions take place further from the contact [MLBO96].

sensitivity is demonstrated in Fig. 2.5. With an increase in distance from the contact surface, a rapid decrease in the solid angle for Li ions is observed, whereas the initial impact on α particles is less marked. A rapid decline in sensitivity for one of the reaction products (Li ions) is generally observed as a result. At greater distances, a reduction to zero in sensitivity for α particles is experienced. The probability of neutron absorption per unit distance is described by Eq. 2.4.

$$P(x) = \Sigma e^{-\Sigma(D-x)} dx \tag{2.4}$$

Two equations for the sensitivity of the charged particle detection model post-conversion through the converter layer was provided [MLBO96], which integrated the neutron conversion model with a ^{10}B converter layer from a thickness of 0 to D.

For $D \leq L$:

$$S(D) = 0.5[(1 + \frac{1}{\Sigma L})(1 - e^{-\Sigma D}) - \frac{D}{L}] \tag{2.5}$$

For $D > L$:

$$S(D) = 0.5 e^{-\Sigma(D-L)}[(1 + \frac{1}{\Sigma L})(1 - e^{-\Sigma L}) - 1] \tag{2.6}$$

The changes in detection sensitivity attributable to the two types of charged particles are directly predictable by Eq. 2.5 and Eq. 2.6. An increase in sensitivity

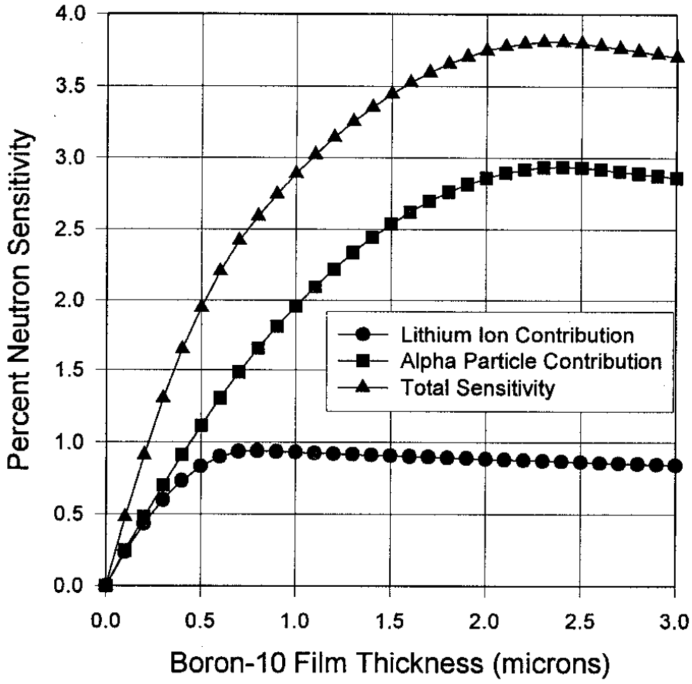

Figure 2.6: Calculated sensitivity of ^{10}B coated GaAs Schottky barrier detectors to thermal neutrons as a function of film thickness. Shown are the sensitivity contributions from the Li ions and α particles as well as the resulting total sensitivity. The analysis was performed for front side irradiation and a particle minimum energy requirement of 300 keV [MLBO96].

is initially observed, as shown in Fig. 2.6, and a peak in sensitivity is reached when the converter layer thickness attains a certain level. The optimised converter layer thickness that is sought is represented by this thickness.

The calculation of the optimal thickness by figures, although possible, is acknowledged as inconvenient. In this research, those equations were expanded upon, and a method for calculating the optimal thickness of a converter layer that yields dual charged particles was further derived. The details of this method will be elaborated in the methodology section, and it forms the foundation for the development of calculation software.

2.5 Monte Carlo method

The Monte Carlo (MC) method, also known as the statistical simulation method, is a numerical calculation method guided by the theory of probability and statistics that was proposed in the mid-1940s due to the development of science and technology and the invention of electronic computers. It involves the use of random numbers (or, more commonly, pseudorandom numbers) to solve a wide range of computational problems. It was invented in the 1940s by scientists Von Neumann, Stanislav Ulam, and Nicholas Metropolis at Los Alamos National Laboratory. Its counterpart is the deterministic algorithm. MC methods are widely used in various research areas, including financial engineering, macroeconomics, biomedicine, computational physics (e.g., particle transport calculations, quantum thermodynamic calculations, aerodynamic calculations), and machine learning.

MC methods can be roughly divided into two categories. The first category includes problems that are inherently stochastic, and their stochastic processes can be simulated directly using computer. For example, in nuclear physics research, the transport of neutrons through a reactor can be analysed by MC method. As the laws of quantum mechanics limit the interaction between neutrons and nuclei, the probability of their interaction can be identified, but not their accurate positions when the neutron interacts with the nucleus and the travel speed and direction of the new neutron produced by fission. Scientists conduct random sampling based on their probability to obtain the fission position, speed, and direction. After simulating the behaviour of a large number of neutrons, the range of neutron transmission can be obtained through statistics, which can be used as the basis for reactor design.

The second category is where the problem being solved can be transformed into the characteristic numbers of random distribution, such as the probability of the occurrence of a random event or the expected value of a random variable. Through random sampling, the probability of a random event is estimated in terms of its frequency of occurrence, or the numerical characteristics of a random variable are estimated in terms of the numerical characteristics of the sample and used as the solution to the problem. This method is mainly used for solving complex multidimensional integration problems.

Suppose there is a task to calculate the area of an irregular graph. The degree of irregularity of the graph is proportional to the complexity of the analytical calculation (e.g., integration). The MC method is based on the analogy that if there is a bag of rice with an area of X per grain, scatter the rice evenly over the graph and count how many grains are in the graph. This number of grains multiplied by the average area of the rice is the area of the graph. When there are smaller grains of rice, the more the rice scatters, the more accurate the result will be. A computer programme can generate a large number of evenly distributed coordinate points. The points within the graph can then be counted, and the area of the graph can be found by looking at their proportion of the total number of points and the area of the range of coordinate points generated.

The GEometry ANd Tracking (Geant4) simulation toolkit uses the MC method to simulate the reaction of particles with matter. When a particle is created in a particle gun, the energy, momentum, and direction of emission of the particle are determined within a range of parameters based on the input file. When the particle touches the geometry, a random number is selected to determine whether the reaction will take place. The results can be obtained by conducting a large number of random simulations. More details about Geant4 will be provided in the following section.

2.6 Geometry and tracking

Geant4, which stands for GEometry ANd Tracking, is a MC simulation package developed by the European Organisation for Nuclear Research (CERN) using C++, an object-oriented programming language, to simulate the physical processes of particle transport through matter [AAA$^+$03, AAA$^+$16]. Geant4 offers a significant advantage over commercial software such as Monte Carlo N-Particle Transport (MCNP) and Electron Gamma Shower (EGS) in that the source code is open source, allowing users to modify and extend it to suit their needs and broaden the program's range of applications.

At its core, Geant4 includes a comprehensive set of physical models that provide control over particle-matter interactions across a wide range of energies. The source code has been built with extensive data and expertise gathered from around the world, making Geant4 a repository for most of the known particle interactions.

Geant4 is written in C++, and its simulation toolkit utilises advanced software engineering techniques and object-oriented programming to achieve simplicity. For instance, the way in which reaction cross sections are entered or calculated is separate from how they are used or accessed. Similarly, the calculation of final states can be divided into alternative or complementary models depending on the energy range, particle type, and material. Users can choose from these options to create a specific application and implement the code in the user-operated classes provided by the toolkit. A significant issue with previous simulation codes was the difficulty in adding new or different physics models, which limited their development due to their increased size and complexity. In contrast, Geant4's object-oriented approach helps manage complexity and limits dependencies by defining a uniform interface and common organisational principles for all physical models. This framework makes it easier to identify and understand model functionality, and new models can be created and added with minimal modification to existing code.

The idea of developing a Geant4 program was first introduced in two independent studies completed by CERN and Japan High Energy Accelerator Research Institute in 1993, with the goal of improving the existing FORTRAN-based Geant3 simulation program using modern computing techniques. These activities merged in the autumn of 1994, and a collaboration was formed with over 100 scientists and engineers from dozens of laboratories, universities, and research institutes in Europe, Russia, Canada, Japan, and the USA, organised by the Probe Research Committee at CERN. The project, known as RD44, aimed to build a completely new program using object-oriented programming techniques based on the C++ language. The program was designed to simulate detectors with the necessary functionality and flexibility to meet the requirements for the next generation of subatomic physics experiments. It was evident that the tool would also benefit the atomic nucleus, accelerator, space, and medical physics communities, leading to rapid expansion of the initial scope with more people joining from these scientific fields. Initial studies were completed in December 1998, and Geant4 was released in February 1999. Since then, Geant4 has been continuously developed and improved with support from users.

The collaboration now benefits from the accumulated experience of many contributors in the field of physical detectors and MC simulations of physical processes. Although geographically distributed software development and large-scale object-oriented systems are no longer new, Geant4 is perhaps the largest project of its kind in terms of the size and scope of the code and the number of contributors. Each part of the Geant4 software corresponds to a distributable component (library), managed separately by a working group of experts. In addition, there are working groups for testing and quality assurance, software management, and document management. The release coordinator is responsible for each group. This distribution of responsibilities between a relatively large number of people allows for a support structure in which external users can direct questions to the appropriate experts.

Users can quickly build customised physical models using the tools in the toolkit. All aspects of the simulation process included in the Geant4 toolkit are as follows:

- The geometry of the simulated system

- The material composition of the simulated system
- Particle sources
- Simulation of the main reaction events
- Particle reaction paths
- Physical processes controlling particle reactions
- Response of sensitive areas of the detector
- Customised storage of detection data
- Visualisation of detector geometry and particle paths

Users can build stand-alone applications or applications based on another object-oriented framework. In either case, the toolkit will support everything from the initial problem definition to the production of results and graphics for output. To this end, the toolkit incorporates a user interaction interface, a built-in console, and command interpreters, all designed to manipulate the various layers of the simulation in a unified manner.

As depicted in Fig. 2.7, Geant4 is composed of several C++ classes. The global class (global) comprises the unit, constant, number, and random number handling systems. Particles and materials incorporate the settings required to describe particles and materials' physical properties and simulate particle-matter

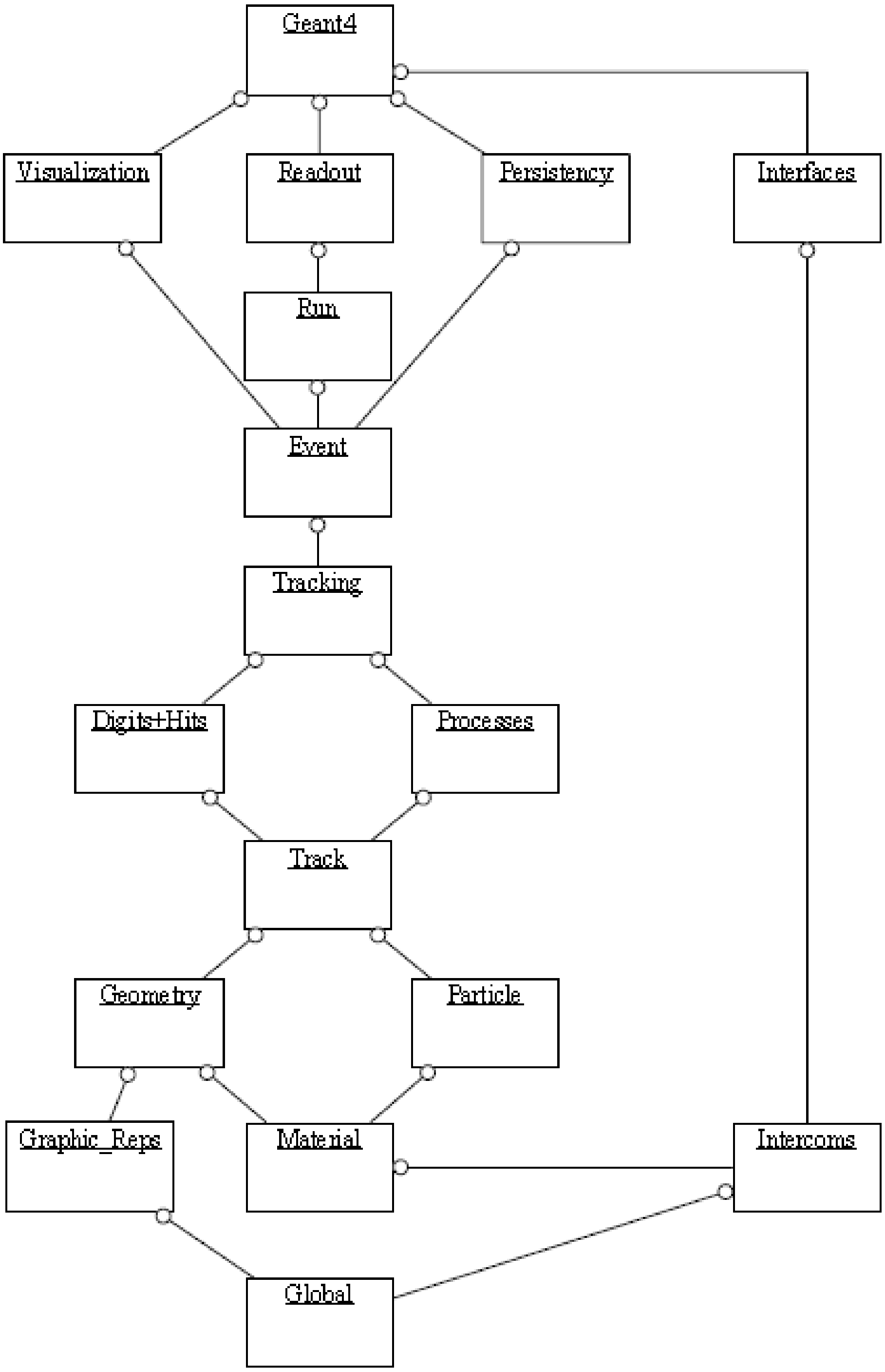

Figure 2.7: The Top Level Category Diagram of the Geant4 toolkit. The open circle on the joining lines represents a using relationship; the category at the circle end uses the adjoined category [AAA+03].

interactions. The geometry module offers the ability to characterise the model's geometry. These fundamental classes are employed to construct the desired physical model. The process classes are invoked by these classes, including stepping, tracking, event, and run. Stepping and tracking oversee the contributions produced when the trail's state changes and provide information in sensitive regions for inquiries. The event classes comprise the tracking and stepping classes, which represent all the reactive processes generated by an emitting particle.

Utilising these classes and interfacing with devices external to the toolkit through abstract interfaces, provide users with visualisation, persistency, and interface capabilities.

2.7 Molecular dynamics

Molecular dynamics (MD) is a set of molecular simulation methods combining physics, mathematics and chemistry, originally based on the idea of Newtonian mechanics for classical systems. The method focuses on the simulation of the motion of molecular and atomic systems utilising computing power. It is a multi-body simulation method that takes samples of a system consisting of different states of the molecular system in order to calculate the conformational integrals of the system and uses the results of the conformational integrals as a basis for further calculations of the thermodynamic quantities and other macroscopic properties of the system.

With the growth of computer processing power, MD has developed rapidly in the last century. The MD method based on the rigid sphere potential was reported in 1957 [AW57], after which a study on the simulation of the properties of liquid argon using the Lennard-Jones potential function method was published. Compared with the rigid spherical potential, this potential energy better describes the interaction between particles. In 1974, MD methods were used to successfully simulate the properties of water with molecular cluster behaviour [SR74]. Afterwards, constant pressure [And80], constant temperature [BPVG$^+$84, EH85] and giant canonical ensemble [CP91] MD methods were developed.

MD method basically consists of four steps: determining the initial configuration, entering the equilibrium phase, proceeding to the production phase, and finally calculating the results. To begin with, the starting structure of the molecule or system to be used in the simulation needs to be obtained, as shown in Fig. 2.8.

The starting structure should have a low energy and be able to remain stable. The general molecular starting structure is derived from experimental data or quantum chemical calculations, e.g. first-principle calculations can be used to obtain the corresponding data. Once the starting structure has been determined, the individual atomic velocities are randomly generated according to the Boltzmann distribution. The atoms will vibrate within the lattice. The temperature of the system also tends to be constant. The randomly generated atomic velocities are adjusted accordingly to the system to ensure that there are no translational shifts in the system.

After this, the process of equilibrating the system is first carried out by introducing temperature or pressure. Once it has been determined that the structure of the system to be simulated is correct and stable, classical Newtonian mechanics is introduced for the calculation. During this process, the molecules and atoms in the system will start moving according to the introduced initial velocities and will attract, repel and collide with each other. The trajectory of each atom of the system will be calculated according to the given interaction potential between the atoms. The interaction potential has a significant influence on the results of the calculation and it is therefore important to ensure that an accurate interaction potential is used to describe the interactions of the molecular atoms within the system before the calculations are carried out. After computational time, the results of the simulations are calculated and the calculation process will be sampled according to the time step set by users.

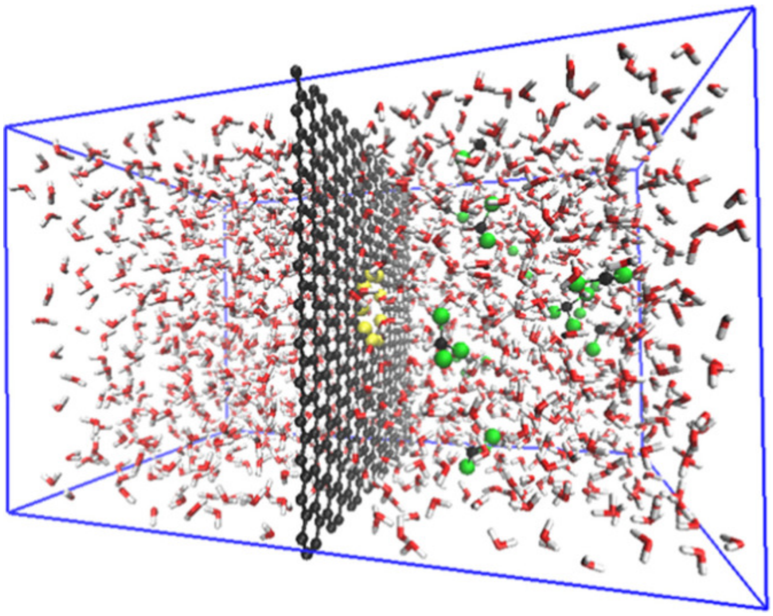

Figure 2.8: A snapshot of the molecular dynamics (MD) simulated system containing graphene membrane for Trihalomethanes (THMs) separation; (green: chlorine, black: carbon, yellow: fluorine, red: oxygen and white: hydrogen). [AKJ15].

2.8 Large-scale atomic/molecular massively parallel simulator

The Large-scale Atomic/Molecular Massively Parallel Simulator (LAMMPS) is a MD simulation package developed by the Sandia National Laboratories in the United States [Pli95]. It can be used to perform MD simulations of solid, liquid and gaseous particles. LAMMPS itself contains empirical potential functions for various elemental atoms, allowing easy modelling of microscopic systems. LAMMPS uses Message Passing Interface (MPI) as support for parallel operations. The new version of LAMMPS also supports Open Multi-Processing (OpenMP) for multi-threaded computing and graphics processing unit (GPU) acceleration. Specifically, in the process of parallel operation, LAMMPS divides the simulation domain into small sub-domains with the same computational cost by using the spatial decomposition technique of MPI parallelisation. One of these subdomains will be assigned to each processor. In addition, multi-threaded parallelisation and GPU acceleration with particle decomposition are available. Early on, LAMMPS was written in Fortran, but the code architecture has now been completely converted to C++. LAMMPS uses neighbour lists to keep track of nearby particles. These lists are optimised for systems with short-range repulsive particles so that the local density of particles does not become too large. This is in contrast to methods used to model plasmas or gravitational bodies (e.g., galaxy formation). In terms of usage, users need to compose the LAMMPS input file. Apart from the setting of boundary conditions and particle types, the input file contains three main parts. The first section contains model parameters such as crystal structure, number of atoms, type of atoms, and charge number of charged particles that need to be calculated. The second part is mainly used to define the interaction force between particles, that is, the definition of potential function. The third part is to select the appropriate ensemble for MD calculation. The first two parts can be read directly from a separate file for the introduction of more complex crystal structures and potential functions. Open visualisation tool (OVITO) [Stu09] is the software typically used for visualising LAMMPS results. In addition, the new version of LAMMPS [TAB$^+$22] also opens the Python interface, which can be used directly for data processing.

Chapter 3

Methodology

In this chapter, the methodology employed to investigate various aspects of the research on radiation detection and damage simulations in semiconductors is presented. The approach encompasses a comprehensive suite of techniques, including radiation detection simulations, a converter layer thickness calculation program based on LLD, an automatic thickness optimisation programme based on the Geant4 toolkit, indirect detection simulations, and radiation damage simulations. Additionally, the search for threshold displacement energy (TDE) of $CsPbBr_3$. Each of these methodologies has been carefully chosen and implemented to address specific research questions and contribute to a deeper understanding of the underlying phenomena. In the following sections, a detailed description of each method is provided, outlining their rationale, and implementation.

3.1 Developed programme

3.1.1 Converter layer thickness calculation programme

In the context of B_4C and LiF, two types of charged particles are generated by the neutron reaction with the converter layer. Hence, by analysing the effects of the two types of charged particles on the detection efficiency, the optimal guidance thickness of the converter layer under different LLDs can be directly determined.

Assuming that the secondary particles are emitted at an angle of 180^o, meaning that the two secondary charged particles move along the same line but in opposite directions during the recoil process, their energies can be calculated using the conservation of momentum and energy, as well as the reaction Q-value. These calculated energies are the same as those shown in Eq. 2.1 and Eq. 2.2. These energies serve as the initial energies of the particles. As an example of the reaction between ^{10}B and thermal neutrons, the derivation is illustrated as follows:

$$\because p_{\mathrm{Li}} = -p_{\alpha}$$

$$\therefore p_{\mathrm{Li}}^2 = p_{\alpha}^2 = p^2$$

$$\because E_{\mathrm{Li}} = \frac{p^2}{2m_{\mathrm{Li}}} \quad \text{and} \quad E_{\alpha} = \frac{p^2}{2m_{\alpha}}$$

$$\because E_{\mathrm{Li}} + E_{\alpha} = Q$$

$$\therefore \frac{p^2}{2m_{\mathrm{Li}}} + \frac{p^2}{2m_{\alpha}} = Q$$

$$\therefore p^2 \left(\frac{1}{2m_{\mathrm{Li}}} + \frac{1}{2m_{\alpha}} \right) = Q$$

$$\therefore p^2 \left(\frac{m_{\alpha} + m_{\mathrm{Li}}}{2m_{\mathrm{Li}} m_{\alpha}} \right) = Q$$

$$\therefore p^2 = \frac{2Q m_{\mathrm{Li}} m_{\alpha}}{m_{\alpha} + m_{\mathrm{Li}}}$$

$$\because E_{\mathrm{Li}} = \frac{p^2}{2m_{\mathrm{Li}}} \quad \text{and} \quad E_{\alpha} = \frac{p^2}{2m_{\alpha}}$$

$$\therefore E_{\mathrm{Li}} = \frac{Q m_{\alpha}}{m_{\alpha} + m_{\mathrm{Li}}}$$

$$\therefore E_{\alpha} = \frac{Q m_{\mathrm{Li}}}{m_{\alpha} + m_{\mathrm{Li}}}$$

Under this assumption, the range L of the particles in the converter layer can be calculated using their initial energies. For the two different charged particles, these ranges are denoted as L_1 and L_2. Therefore, there will be three scenarios for the optimal thickness D of the converter layer relative to the ranges L_1 and L_2 of the two types of charged particles within the converter layer materialise: $D \leq L_1 < L_2$, $L_1 < D < L_2$, and $L_1 < L_2 \leq D$.

1. For $D \leq L_1 < L_2$, when considering the presence of two types of charged particles, the following formula is derived from the equations in the last chapter:

$$
\begin{aligned}
S(D) =& 0.5[(1+\frac{1}{\Sigma L_1})(1-e^{-\Sigma D})-\frac{D}{L_1}] \\
&+0.5[(1+\frac{1}{\Sigma L_2})(1-e^{-\Sigma D})-\frac{D}{L_2}]
\end{aligned}
\tag{3.1}
$$

The first derivative is then calculated to obtain:

$$S'(D) = \Sigma e^{-\Sigma D} + \frac{0.5e^{-\Sigma D}-0.5}{L_1} + \frac{0.5e^{-\Sigma D}-0.5}{L_2} \tag{3.2}$$

Setting the first derivative equal to zero allows for the determination of the function's extremum:

$$D_1 = \frac{ln(\frac{2\Sigma}{\frac{1}{L_1}+\frac{1}{L_2}}+1)}{\Sigma} \tag{3.3}$$

It is straightforward to ascertain that D_1 is greater than zero since both the numerator and denominator are greater than zero. However, it is challenging to determine whether it is less than L_1. D_1 can be calculated using numerical methods because the values of constants in the equation are known. If D is less than L_1, the value of $S(D_1)$ is directly taken as the maximum value of the interval. If D_1 is greater than L_1, then further analysis is required.

The first derivative is inconvenient for making a determination. The second derivative is subsequently solved for, yielding:

$$S''(D) = -\Sigma^2 e^{-\Sigma D} - \frac{0.5e^{-\Sigma D}}{L_1} - \frac{0.5e^{-\Sigma D}}{L_2} \tag{3.4}$$

Observation reveals that the second derivative is continuous and less than zero throughout the interval $[0, L_1]$. This implies that the first derivative is monotonically decreasing within this interval. Therefore, $S'(L_1)$ represents the minimum value of the first derivative in this range. Consequently, by evaluating whether $S'(L_1)$ is greater than zero, the monotonicity of the function in this interval can be further analysed. According to assumption, it has been known that when the D_1 is taken, the first derivative is equal to zero, and D_1 is greater than L_1. The derivation is illustrated as follows:

$$\because S'(D_1) = \Sigma e^{-\Sigma D_1} + \frac{0.5e^{-\Sigma D_1} - 0.5}{L_1} + \frac{0.5e^{-\Sigma D_1} - 0.5}{L_2} = 0$$

$$\therefore e^{-\Sigma D_1} = \frac{1}{1 + \frac{2\Sigma}{\frac{1}{b}+\frac{1}{c}}}$$

$$\because D_1 > L_1 > 0 \quad \Sigma > 0$$

$$\therefore e^{-\Sigma D_1} < e^{-\Sigma L_1}$$

$$\therefore e^{-\Sigma L_1} > \frac{1}{1 + \frac{2\Sigma}{\frac{1}{b}+\frac{1}{c}}}$$

$$\therefore S'(L_1) > 0$$

From above derivation, $S'(L_1) > 0$ can be obtained. This indicates that the function is monotonically increasing within this interval, and thus, the maximum value of $S(D)$ is attained when $D = L_1$.

2. For $L_1 < D < L_2$,the formula of $S(D)$ is shown in Eq. 3.5.

$$\begin{aligned} S(D) =& 0.5e^{-\Sigma(D-L_1)}[(1+\frac{1}{\Sigma L_1})(1-e^{-\Sigma L_1})-1] \\ &+0.5[(1+\frac{1}{\Sigma L_2})(1-e^{-\Sigma D})-\frac{D}{L_2}] \end{aligned} \tag{3.5}$$

Same to the last condition, the first derivative is then calculated to be obtained in Eq. 3.6:

$$S'(D) = \Sigma e^{-\Sigma D} + \frac{0.5e^{-\Sigma D} - 0.5}{L_2} - \frac{0.5e^{-\Sigma(D-L_1)}(-e^{-\Sigma L_1}+1)}{L_1} \tag{3.6}$$

Setting the first derivative equal to zero allows for the determination of the function's extremum, D_2:

$$D_2 = \frac{ln(\frac{2\Sigma L_1 L_2 + L_1 + L_2(1-e^{\Sigma L_1})}{L_1})}{\Sigma} \tag{3.7}$$

To ascertain whether the $S(D_2)$ is a maximum or a minimum, points immediately to the left and right of D_2, denoted as D_{2L} and D_{2R}, are selected for evaluation.

$$\because D_{2L} < D_2 < D_{2R}$$

$$\therefore S'(D_{2L}) > S'(D_2) > S'(D_{2R})$$

$$\because S'(D_2) = 0$$

$$\therefore S'(D_{2L}) > 0 > S'(D_{2R})$$

From the aforementioned derivation, it can be understood that the first derivative is greater than zero to the left of D_2, and less than zero to the right of D_2, indicating that $S(D_2)$ is the maximum point within the interval.

3. For $L_1 < L_2 \leq D$, the formula of $S(D)$ is shown in Eq. 3.8.

$$\begin{aligned} S(D) =& 0.5e^{-\Sigma(D-L_1)}[(1+\frac{1}{\Sigma L_1})(1-e^{-\Sigma L_1})-1] \\ &+ 0.5e^{-\Sigma(D-L_2)}[(1+\frac{1}{\Sigma L_2})(1-e^{-\Sigma L_2})-1] \end{aligned} \tag{3.8}$$

Due to the function's monotonic decrease, the maximum detection efficiency is approached as D nears L_2, hence the calculation is based on L_2. $S(L_2)$ is greater than the maximum value in this interval.

The maximal sensitivities within the three respective intervals are computed directly. By comparing these three sensitivities, the thickness corresponding to the greatest sensitivity value is identified as the optimal guidance thickness.

A calculation program for the optimal thickness of boron and lithium-type converter layers has been developed, with Python serving as the programming language. The code has been packaged using PyInstaller, resulting in an executable program. The interface of the program is depicted in Fig. 3.1.

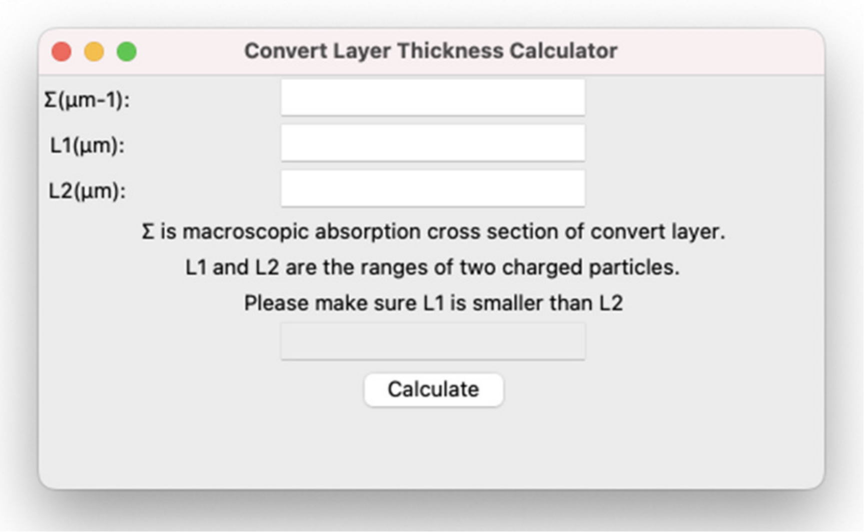

Σ is macroscopic absorption cross section of convert layer.
L1 and L2 are the ranges of two charged particles.
Please make sure L1 is smaller than L2

Figure 3.1: The window of the converter layer thickness calculation programme.

In the converter layer material, the ranges of the two types of charged particles are represented by $L1$ and $L2$, and the macroscopic neutron absorption cross-section of the converter layer is denoted by Σ. This cross-section is determined by the density of the converter layer material and the content of ^{10}B and ^{6}Li. In the calculations performed by this program, the different ranges of secondary charged particles within the converter layer under various LLDs have been taken into account.

The particle ranges under different LLDs can be found in Tab. 3.1 and Tab. 3.2. These data are utilised to ascertain the optimal converter layer thicknesses at various LLD settings. The data were obtained using the SRIM (Stopping and Range of Ions in Matter) software.

Table 3.1: The ranges of α-particle and ^7Li in B_4C under LLDs ranging from 100 keV to 900 keV. Q = 2.310 MeV

LLD (keV)	100	200	300	400	500	600	700	800	900
α (μm)	2.94	2.72	2.51	2.30	2.10	1.90	1.71	1.52	1.34
^7Li (μm)	1.49	1.36	1.23	1.09	0.93	0.74	0.51	0.19	0.00

Table 3.2: The ranges of ^3H and α-particle in LiF under LLDs ranging from 100 keV to 900 keV. Q = 4.78 MeV

LLD (keV)	100	200	300	400	500	600	700	800	900
α (μm)	5.52	5.23	4.95	4.67	4.40	4.13	3.87	3.61	3.36
^3H (μm)	30.49	28.80	27.15	25.54	23.97	22.44	20.96	19.52	18.12

In the forthcoming version, it is intended that the Bethe-Bloch equation will be introduced to allow for the direct calculation of the ranges of the two types of charged particles within the converter layer based on the LLD provided by the user, thereby enhancing the user experience.

3.1.2 Search for threshold displacement energy programme

The TDE is the minimum kinetic energy required for an atom to be permanently displaced from its lattice site to a defect position. It is also known as displacement threshold energy or displacement energy.

While conducting studies on the neutron radiation resistance of $CsPbBr_3$, limited TDE studies on $CsPbBr_3$ were found. Therefore, LAMMPS toolkit was used to obtain the TDE of $CsPbBr_3$ computationally, and based on this, an automatic TDE search programme for $CsPbBr_3$ with a command line interface was developed based on Linux scripts.

Since the crystal structure of $CsPbBr_3$ is highly symmetrical, it is not necessary to calculate every angle in space when calculating the TDE. The spherical coordinate system is used with azimuthal angle (ϕ) uniformly chosen between $0°$ and $90°$, polar angle (θ) between $0°$ and $90°$, and an angle step size of $5°$ for both ϕ and θ, resulting in a total of 361 directions.

To balance the speed and accuracy of the calculations, a simulation supercell ($10\times10\times10$) containing 5000 atoms was employed. The isothermal-isobaric ensemble is known as NPT in molecular dynamics (MD) simulations. NPT stands for an ensemble in which the Number of particles (N), Pressure (P), and Temperature (T) are kept constant during the simulation. It was used to equilibrate the system until it reached the required temperature. The system was equilibrated at specific temperatures of 100 K, 200 K, 300 K, and 400 K. The size of the system was slightly adjusted during the relaxation process to help the equilibration. After equilibration, a Langevin thermostat [HLM82], [Eva83] was applied to the system's edge, and the microcanonical ensemble, which is known as NVE. NVE stands for an ensemble in which the Number of particles (N), Volume (V), and Energy (E) are kept constant during the simulation. It was used for cascade simulations.

For each direction, a Cs, Pb, or Br atom around the central region of the system was selected as a primary knock-on atom (PKA). The Bisection method was used to obtain the TDE for each type of atom. If the relationship between the velocity of the PKA (v) and the number of defects (N) is expressed as $f(v) = N$, then the process is illustrated below:

1. Find two velocities, say v_1 and v_2, such that $v_1 < v_2$ and $f(v_1) = 0$ and $f(v_2) > 1$.
2. Find the midpoint of v_1 and v_2; say v_3.
3. v_3 is the final velocity of the given function if $f(v_3) = 1$; else follow the next step.
4. Divide the interval $[v1, v2]$. If $f(v_3) > 1$, theres exist a solution between v_1 and v_3, else if $f(v_3) = 0$, there exists a solution between v_3 and v_2.
5. Repeat above steps until $f(v) = 1$. The kinetic energy of an atom with

velocity v_3 is the TDE in this direction.

In order to determine the TDE, the counting of defects is a crucial step. The Wigner-Seitz (WS) cell method [WS33], implemented in OVITO, is employed to count the defects.

The last frame from the equilibration simulation is considered as the reference 'defect-free' configuration. The centre of a WS cell is defined by each atom site in the reference frame. Any atom located within the WS cell is deemed to occupy this site. By counting the number of atoms present in each WS cell, vacancy, interstitial, and antisite defects can be identified in subsequent frames.

In TDE simulations, the final frame of the cascade simulation is used to study the number of defects that have occurred. By counting the number of defects present in this final frame, researchers can determine whether the PKA energy used in the simulation is equal to or greater than the TDE. As mentioned earlier, if the number of defects is greater than 1, it indicates that the PKA energy is greater than the TDE. If the number of defects is equal to 1, it suggests that the PKA energy is equal to the TDE. If the number of defects is less than 1, it implies that the PKA energy is less than the TDE. Therefore, the numerical value of the TDE can be obtained.

3.1.3 Automatic semiconductor layer thickness optimisation programme

When employing the Geant4 toolkit for semiconductor layer thickness optimisation, it is essential to determine the neutron detection efficiency of the detector at varying thicknesses. Although the Geant4 toolkit supports changing specific variables during operation, this method has a disadvantage in that it requires waiting until a specific thickness calculation is completed before the next calculation can commence. In cases where the number of simulated neutrons is substantial, the speed of MC calculation can be prolonged, often spanning tens of hours and detrimental to research efficiency. Despite the Geant4 calculation code being deployable on supercomputers that utilise multiple cores, waiting for the completion of one thickness calculation before the next calculation can commence is still necessary.

Therefore, this study developed a Linux script-based programme that automatically generates Geant4 source files with varying thicknesses and submits them for computation to the supercomputer. The programme generates multiple source files for a list of thicknesses set by users and modifies each source file accordingly. As a result, the parallel simultaneous calculation of various thicknesses is achieved, significantly reducing the computation time. Users can also use the serial operation mode to save storage space, as the program will automatically delete old files, except for the results of each calculation.

3.2 Radiation detection simulations

3.2.1 Semiconductor layer thickness optimisation simulations

The detector utilised during the simulations is structured as shown in Fig. 3.2, it has an active area of 1 cm^2. The detector comprises two layers, with the upper layer being a converter layer containing B_4C or LiF and the bottom layer being the semiconductor layer. During thermal neutron detection, thermal neutrons initially react with the converter layer, producing charged particles such as α particles or tritium. These charged particles then generate electron and hole pairs along their track in the semiconductor. The generated electrons and holes will drift in the semiconductor material with the aid of an external electric field, which in turn induces a current in an external circuit that can be detected. This simulation study did not include a dead layer, nor did it involve ion implantation and doping of the semiconductor material. Consequently, the detection efficiency can be deemed as the intrinsic thermal neutron detection efficiency of the material.

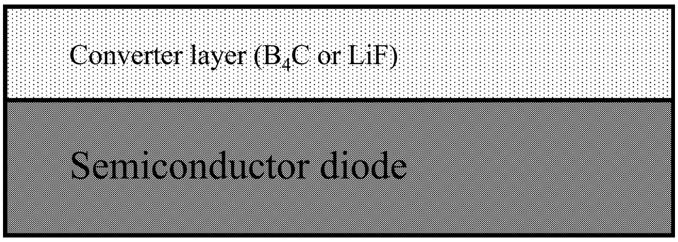

Figure 3.2: Schematic structure of the simulated detector.

The research primarily focused on studying the response of detectors to neutrons. For the simulations, Geant4 version 10.7 was utilised alongside the FTFP_B-

ERT_HP physics list. The FTFP_BERT_HP physics list employs high precision neutron models and cross-sections to describe elastic and inelastic scattering, capture, and fission for neutrons. During simulations, the neutron source was placed 1 cm above the centre of the upper surface of the detector. To reduce uncertainty while maintaining an acceptable simulation runtime, each simulation incorporated 50 million neutrons. The High-End Computing (HEC) Cluster at Lancaster University was employed to perform these simulations.

$$N_{\Omega} = N_{Total} \times \frac{\Omega}{4\pi} \tag{3.9}$$

$$\varepsilon = \frac{Pulses}{N_{\Omega}} \tag{3.10}$$

The absolute detection efficiency of the detector is calculated using Eq. 3.9 and Eq. 3.10. N_{Ω} represents the number of neutrons emitted by the source at an angle Ω (rad), and N_{Total} is the total number of particles emitted from the neutron. ε represents the ratio of recorded pulses to the number of particles at angle Ω (N_{Ω}) obtained from the simulation.

The detection efficiency is expressed as a percentage, with one decimal place retained. The semiconductor thickness at which the detection efficiency reaches its maximum is considered the optimal thickness.

To eliminate background counting during the actual detection process, a LLD was introduced. Following previous studies, LLD from 100 keV to 900 keV were employed [MHY+03] to evaluate the influence of different LLDs on the detection efficiency curve.

For different semiconductor neutron detector materials with the same converter layer material and LLD, the optimal thickness of the converter layer should be identical [WMBC15]. Therefore, B_4C and LiF were selected as the converter layer materials. The enrichment levels of ^{10}B in B_4C and ^{6}Li in LiF for the simulations are both 99.99%. This enrichment level for ^{10}B in B_4C is not difficult to achieve and can be purchased from American Elements. For ^{6}Li in LiF, achieving this enrichment level is possible but remains challenging. However, to test the potential maximum detection efficiency of a detector with a ^{6}LiF converter layer, an enrichment level of 99.99% for ^{6}Li is still chosen. LiF with 95% atom mass of ^{6}Li can be obtained from Merck. For the converter layer thickness, the results with 300 keV LLD were compared with those of other researchers [MHY^{+}03], and the thicknesses of the two converter layers for different LLD simulations were studied. In addition, the results obtained from theory were compared with Geant4 simulation results.

In summary, the semiconductor layer thickness was optimised by exploring the relationship between the semiconductor layer thickness and the detector's detection efficiency with fixed converter layer thickness.

3.2.2 Gamma resistance simulations

The Geant4 configuration for the study of γ-ray rejection capabilities is fundamentally similar to that used for neutron irradiation simulations. The primary distinction lies in the substitution of the radiation source from a neutron source to a γ source. Furthermore, the energy range of the γ rays is set from 0.5 MeV to 1.5 MeV. The choice of this energy range is due to many common γ-ray sources, including radioactive isotopes such as cobalt-60 (^{60}Co) and caesium-137 ^{137}Cs, which emit γ-ray energies within this range (1.173 MeV and 1.332 MeV for ^{60}Co, 0.662 MeV for ^{137}Cs). Therefore, simulating the intrinsic detection efficiency within this energy range can reflect the detector's performance in practical applications. Furthermore, selecting a 0.1 MeV energy step is intended to balance the coverage of the energy range with the simulation duration. Gamma rays of energy below 0.5 MeV are not considered, as they would be filtered out by the LLD. The thickness of the semiconductor is increased incrementally from 0 μm to 80 μm.

The γ-ray rejection capability of the detector was evaluated by calculating the γ-ray detection efficiency of the detector. The γ-ray detection efficiency was computed using Eq. 3.9 and Eq. 3.10. Using this method, the γ-ray rejection capability of detectors consisting of different materials was assessed.

The maximum allowable thickness of the semiconductor was determined for scenarios where the γ-ray energy range lies between 0.5 MeV to 1.5 MeV, under a 300 keV LLD, ensuring that the intrinsic γ detection efficiency is less than 10^{-6}. Ideally, the intrinsic detection efficiency for γ should be zero to guarantee that no γ exposure can trigger 'false-positive' neutron counts. However, the standard specifications for radiation portal monitors stipulate that the intrinsic detection efficiency for γ ray should be less than 10^{-6} [MKM^{+}12].

3.3 Displacement damage simulations

3.3.1 Molecular dynamics simulations

In 2021, $CsPbBr_3$ was first used for neutron detection with a converter layer [EBKAA+21]. When neutrons collide elastically with an atom, if the kinetic energy imparted by the neutrons is greater than the TDE of the lattice site, the atom will be knocked out of the lattice, creating a vacancy and an interstitial atom. Therefore, the TDE of a material is an indicator of its radiation resistance. However, to the best of our knowledge, at the time this thesis was written, there have been no studies on the TDE of $CsPbBr_3$ using MD simulations or on the effects of neutron radiation on $CsPbBr_3$ at different temperatures.

In this section, the MD simulations configuration used for TDE search of $CsPbBr_3$ will be introduced, which includes the crystal structure and potential information.

The structure of $CsPbBr_3$ used in the MD simulations is illustrated in Fig. 3.3. The density used in this research is 4.42 g/cm^3. The crystal system is cubic. The Hermann-Mauguin symbol is $Pm\bar{3}m$[221]. Hall group is $-P\ 4\ 2\ 3$. The lattice parameters are $a = b = c = 6.017\ \mathring{A}$ and $\alpha = \beta = \gamma = 90^o$ [Pro20].

Molecular dynamics utilises a potential model to calculate the interactions between atoms. The choice of potential model can significantly affect the results of the simulation. In this research, the Lennard-Jones (LJ) 12-6 potential [Jon24] and

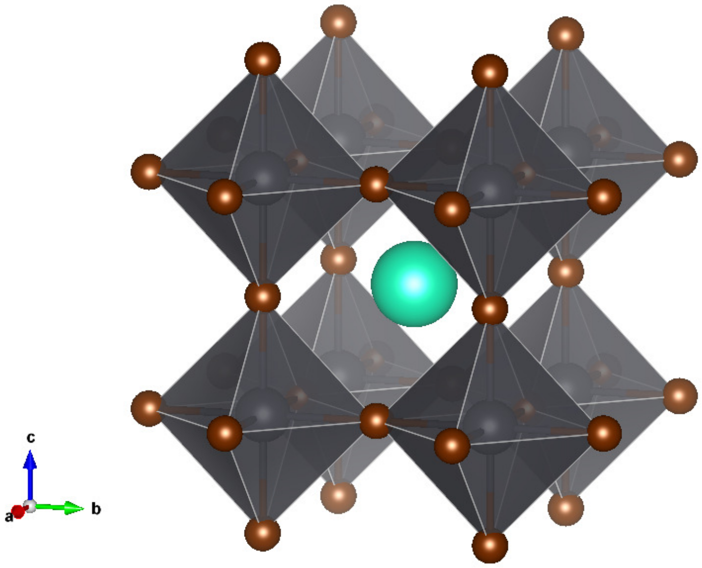

Figure 3.3: Crystal structure of $CsPbBr_3$ for the molecular dynamics (MD) simulations performed. It shows green spheres representing Cs atoms, yellow spheres representing Br atoms, and Pb atoms inside the gray rhombi.

Coulomb potential were used. The general form of the potential model is shown in Eq. 3.11, Eq. 3.12, and Eq. 3.13.

$$V_{lj}(r_{ij}) = 4\epsilon(\frac{\sigma^{12}}{r_{ij}^{12}} - \frac{\sigma^{6}}{r_{ij}^{6}}) \tag{3.11}$$

$$V_{coul}(r_{ij}) = \frac{q_i q_j}{4\pi\epsilon_0 r_{ij}} \tag{3.12}$$

$$V(r_{ij}) = V_{lj} + V_{coul} \tag{3.13}$$

In Eq. 3.11, Eq. 3.12, and Eq. 3.13, the atom labels i and j represent two interacting atoms, and r_{ij} represents the distance between them. Equation 3.11 describes the LJ 12-6 potential, where ϵ represents the depth of the potential well and σ is the separation distance where the potential energy is zero. Equation. 3.12 describes the Coulomb potential, where q_i and q_j represent the charges of the two interacting ions, and ϵ_0 is the permittivity of a vacuum. Equation. 3.13

combines the LJ 12-6 potential and the Coulomb potential to describe the overall interaction between the atoms. This potential model was derived and optimised using density functional theory (DFT) and was successfully employed to predict the phase transfer of $CsPbBr_3$ [BLF+20]. The potential model parameters used in this study are listed in Tab. 3.3.

Table 3.3: Force field parameters for the potential model used in LAMMPS simulations. ϵ represents the depth of the potential well. σ is the separation distance where the potential energy is zero. q represent the charge of the ions.

	$\epsilon(eV)$	$\sigma(\AA)$	$q(e)$
Cs	0.5784	2.927	0.86
Pb	0.01071	20524	1.03
Br	0.01023	4.129	-0.63

In addition, the Ziegler-Biersack-Littmark (ZBL) [ZZB10], shown in Eq. 3.14, is applied to the LJ and Coulomb potential in the cascade simulation at small distances. The ZBL potential is a widely used empirical potential for modeling the interactions between energetic ions and target atoms in nuclear collision cascades and ion implantation simulations. The potential is based on the Thomas-Fermi model and the effective charge concept. It describes the short-range repulsive forces that dominate when two atomic nuclei come close together. In Eq. 3.14, e represents the electron charge, ϵ_0 denotes the electrical permittivity of a vacuum, and Z_i and Z_j correspond to the nuclear charges of the two atoms. It is worth noting that the values of Z_i and Z_j typically equal the atomic numbers of the respective atom types. $\phi(r_{ij}/a)$ is the universal screening function. It is the key component of the ZBL potential and used to reproduce the repulsive part of the screened Coulomb potential for various elements. The factor a in $\phi(r_{ij}/a)$ is a scaling factor. This factor is introduced to account for the specific atomic species involved in the interaction, ensuring that the potential is suitable for a variety of different materials. $S(r_{ij})$ is a switching or screening function that smoothly transitions the ZBL potential to another potential (often a long-range potential) at larger interatomic distances. This is done to combine the short-range repulsive ZBL potential with a more comprehensive potential that also accounts for other types of atomic interactions, such as covalent bonding and van der Waals forces. The spline is performed using the atsim.potentials package.

$$\begin{aligned} E_{ij}^{ZBL} &= \frac{1}{4\pi\epsilon_0}\frac{Z_iZ_je^2}{r_{ij}}\phi\left(\frac{r_{ij}}{a}\right) + S(r_{ij}) \\ a &= \frac{0.46850}{Z_i^{0.23}+Z_j^{0.23}} \\ \phi(x) &= 0.18175e^{-3.19980x} + 0.50986e^{-0.94229x} \\ &\quad + 0.28022e^{-0.40290x} + 0.02817e^{-0.20162x} \end{aligned} \tag{3.14}$$

The potential curves variation with distance are illustrated in Fig. 3.4. Potential curves represent the potential energy of a molecular system as a function of the atomic positions or interatomic distances. They play a crucial role in determining the forces acting on atoms and the resulting dynamics of the system.

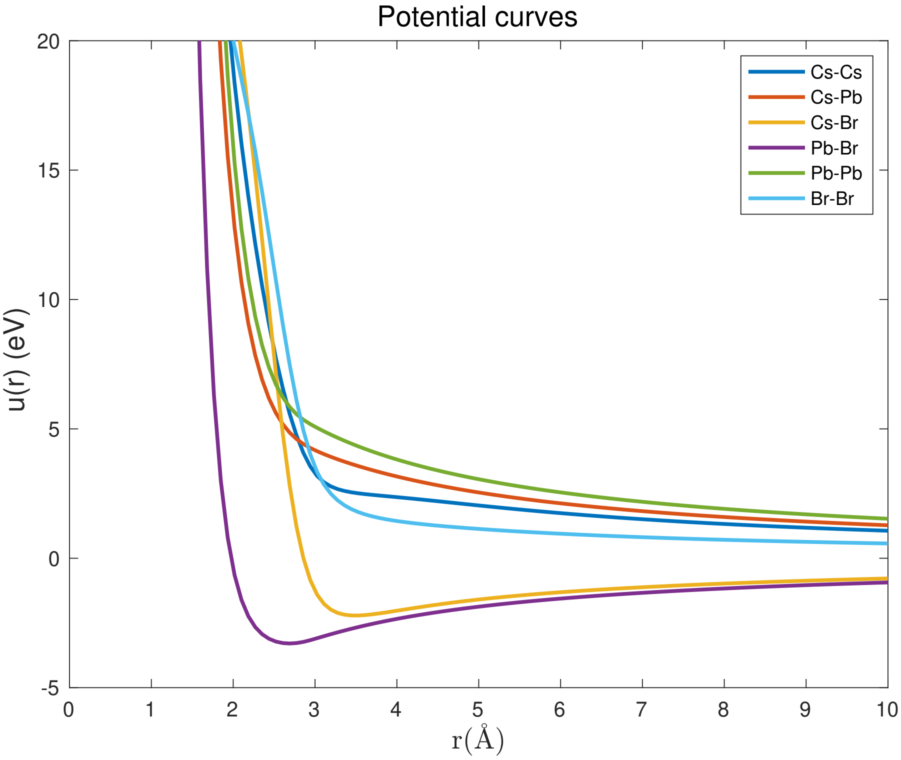

Figure 3.4: Potential curves for molecular dynamics (MD) simulations.

3.3.2 Monte Carlo simulations

It is difficult for thermal neutrons to induce cascade collisions among semiconductor atoms due to their low energy ($0.025\ eV$). However, the neutron energy in the environment around the detector could be higher, especially during a nuclear accident when the reactor core will leak high-energy neutrons. Therefore, the radiation damage effects of high-energy neutrons on detectors are studied. The radiation damage effects are mainly ionisation damage and displacement damage. For neutron irradiation, ionisation damage is negligible; therefore, displacement damage is studied.

When a high-energy neutron collides elastically with an atom within the semiconductor, there is a certain probability that the atom will move and leave the lattice position. As mentioned in previous sections, an atom that is hit by a neutron and causes it to displace is called a primary knock-out atom (PKA). Since a PKA has part of the kinetic energy of the neutron, it will continue to collide elastically with other atoms. Atoms that collide with PKAs and cause further displacements are called Secondary Knock-on Atoms (SKAs). The process is shown in Fig. 3.5.

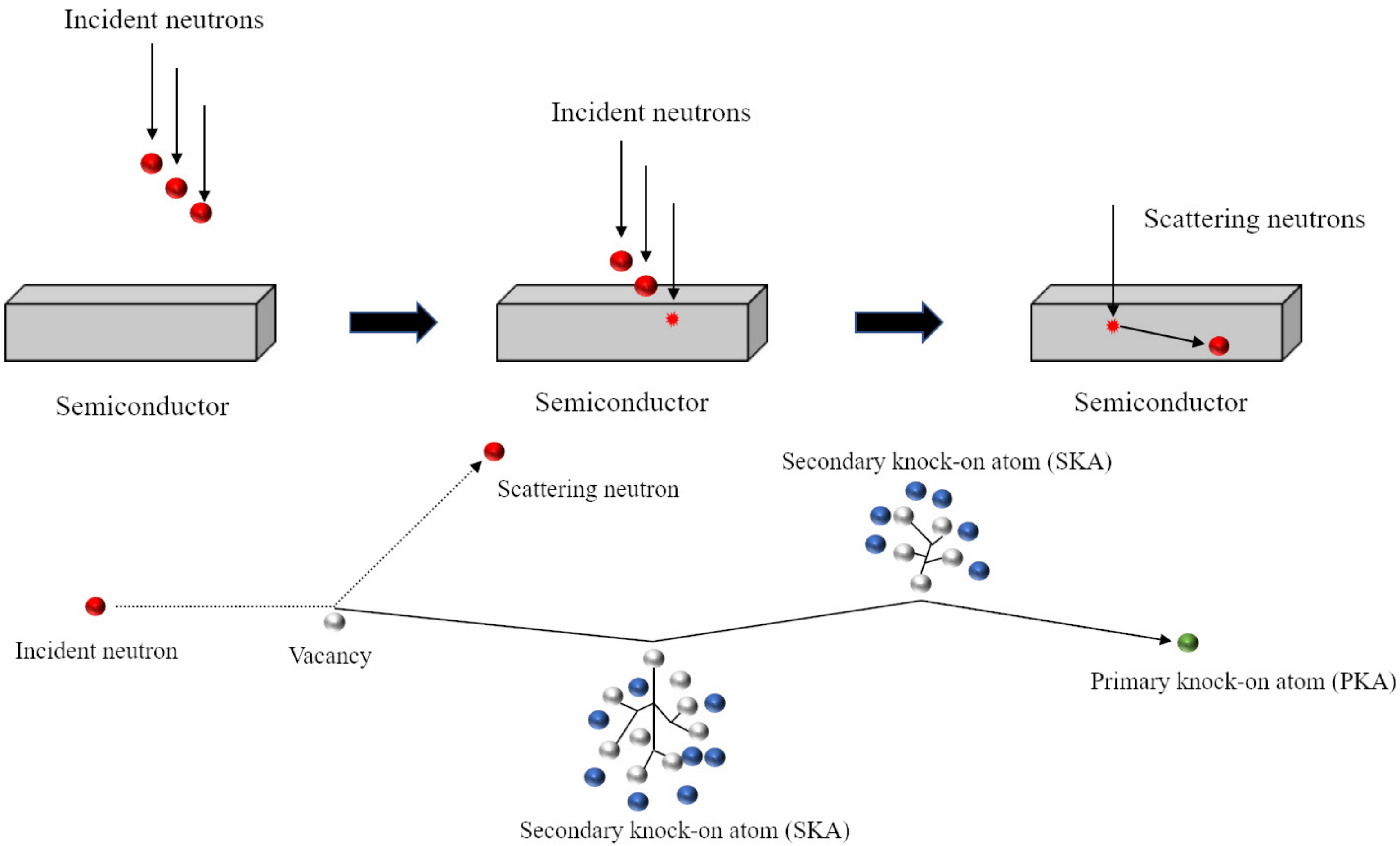

Figure 3.5: The illustrative process of neutron-induced Primary Knock-on Atoms (PKA) and Secondary Knock-on Atoms (SKA) in the semiconductor material. [ZA21a]

Material defects can be caused by the accumulation of these displacements. Therefore, the radiation resistance of the material can be predicted by calculating the displacement per atom (DPA). In this part of the study, the PKA energy spectra generated by 1 MeV neutron flux were simulated, as this energy represents the defined energy level for fast neutrons. The thicknesses of the semiconductor materials were determined through thickness optimisation, and the semiconductors were irradiated with a converter layer coating. Atomic displacements were calculated using a model that considered the kinetic energy transfer, as shown in Eq. 3.15 [NZS+18].

$$N_d(T_d) = \begin{cases} 0 & T_d < E_d \\ 1 & E_d \leq T_d < \frac{2E_d}{0.8} \\ \frac{0.8T_d}{2E_d} & \frac{2E_d}{0.8} \leq T_d < \infty \end{cases} \tag{3.15}$$

Where N_d is the predicted number of atom displacements and T_d is the damage energy (eV) which is the kinetic energy transferred to PKA from a neutron in this study. E_d is the TDE (eV). Table 3.4 shows the TDE for diamond, 4H-SiC, Ga_2O_3 and GaN. The TDE of $CsPbBr_3$ will be obtained in the later chapter. To perform a qualitative analysis of the radiation hardness of these materials and to simplify the simulations, the TDE for GaN was set to the average TDE of Ga and N in GaN, which is 20 eV, and the TDE for SiC was set to 27 eV, which is the average TDE of Si and C in SiC. A 1 MeV neutron flux was used as the particle source in these simulations.

Table 3.4: Threshold displacement energy for diamond, 4H-SiC, Ga_2O_3 and GaN. Reference to source is shown in square parentheses.

	Diamond	**4H-SiC**	**Ga_2O_3**	**GaN**
TDE (eV)	35	Si:35 C:20	25	Ga:18 N:22
	[WMBC15]	[WMBC15]	[KPF+19]	[WMBC15]

Additionally, the radiation damage prediction model for studying semiconductor PKA spectra has been successfully employed to conduct energy deposition analysis of B drug capsules under neutron irradiation [SGF+23]. The simulation results are in good agreement with the experimental data, which confirms the effectiveness of the simulation model.

Chapter 4

Results

This chapter presents the results of the simulations and analytical methods covered in the previous chapter. Advancements in wide-bandgap (WBG) semiconductor neutron detection materials are explored, focusing on the validation of the MC simulation model, optimal thickness for converter and semiconductor layer, the study of TDE of $CsPbBr_3$, microscopic radiation damage, and γ-ray rejection capabilities. The comparison of $alpha$-particle range from MC simulation and SRIM simulation is addressed in the first section, ensuring the accuracy of the Geant4 simulation framework. The second section gives the results of optimal thicknesses of the converters and indirect detection materials. The TDE of $CsPbBr_3$ is investigated in the third section, and the results of the third section will be used in the fourth section, microscopic neutron radiation resistance. Gamma rejection capabilities, crucial to neutron detectors, are evaluated in the last section.

4.1 Monte Carlo simulation model validation

The primary interaction involving thermal neutrons, with an energy of 0.025 eV, and the converter layer (either B_4C or LiF) is the reaction of thermal neutrons with either B or Li. As highlighted in the preceding section, these reactions generate charged particles, which then deposit energy in the detector. Therefore, it is crucial to ensure that the MC simulation model correctly reflects the energy loss of charged particles in the material.

The validation process involves obtaining the range of α-particles in the BN. The results of the validation are then compared with those calculated by Stopping and Range of Ions in Matter Software (SRIM). According to the SRIM calculation, the range of an α-particle in BN with an energy of 5.84 MeV is 25.76 μm (Fig. 4.1). This energy was selected because it is the typical α-particle energy from a ^{241}Am source, which is the source used in α-particle detection experiments.

Figure 4.2 illustrates the detection efficiency of α-particles as a function of BN thickness obtained using the research model in this study. The data reveal that the detection efficiency is 99.9667% at 25 μm and 100% at 26 μm, indicating that the range of the 5.84 MeV α-particle in the BN is between 25 μm and 26 μm. This outcome aligns with the predictions of SRIM, thereby confirming the precision of the model's configuration in estimating the energy dissipation of charged particles within the material. Additionally, it further confirms the accuracy of the neutron detection efficiency obtained through the model.

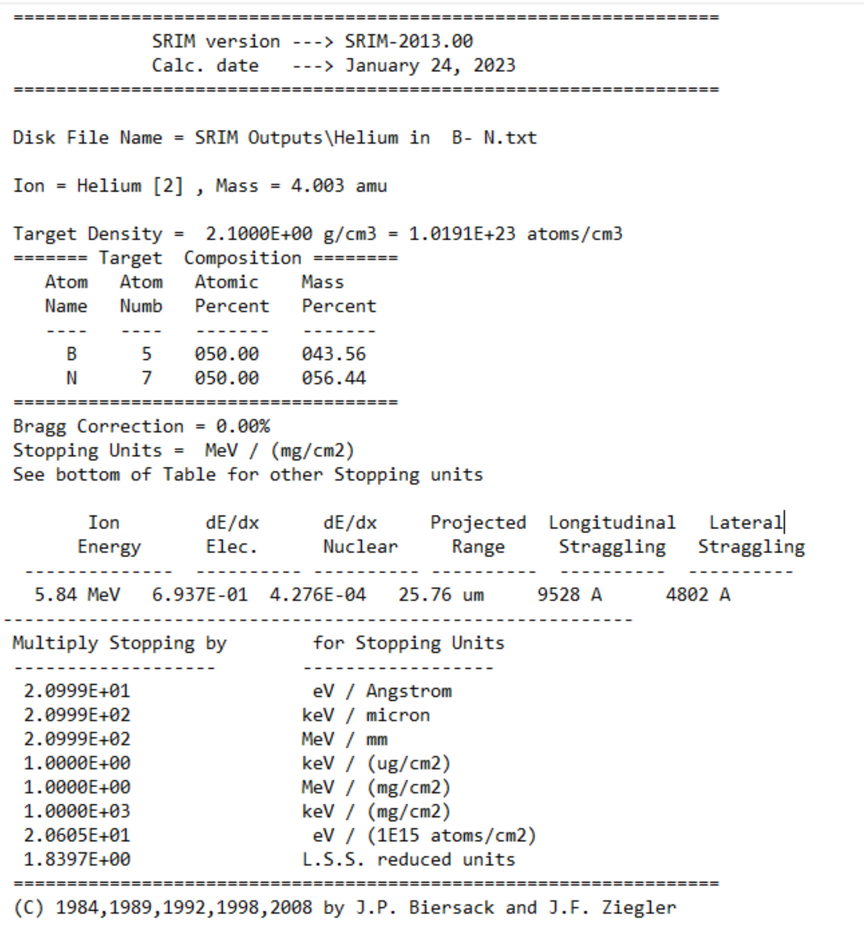

```
==================================================================
             SRIM version ---> SRIM-2013.00
             Calc. date   ---> January 24, 2023
==================================================================

Disk File Name = SRIM Outputs\Helium in  B- N.txt

Ion = Helium [2] , Mass = 4.003 amu

Target Density =  2.1000E+00 g/cm3 = 1.0191E+23 atoms/cm3
======= Target  Composition ========
   Atom   Atom   Atomic    Mass
   Name   Numb   Percent   Percent
   ----   ----   -------   -------
     B      5    050.00    043.56
     N      7    050.00    056.44
====================================
Bragg Correction = 0.00%
Stopping Units =  MeV / (mg/cm2)
See bottom of Table for other Stopping units

       Ion        dE/dx      dE/dx     Projected  Longitudinal   Lateral
      Energy      Elec.      Nuclear     Range     Straggling   Straggling
  -----------  ---------- ---------- ----------  ----------  ----------
  5.84 MeV   6.937E-01  4.276E-04   25.76 um     9528 A      4802 A
-----------------------------------------------------------
Multiply Stopping by        for Stopping Units
-------------------        -----------------
 2.0999E+01                  eV / Angstrom
 2.0999E+02                 keV / micron
 2.0999E+02                 MeV / mm
 1.0000E+00                 keV / (ug/cm2)
 1.0000E+00                 MeV / (mg/cm2)
 1.0000E+03                 keV / (mg/cm2)
 2.0605E+01                  eV / (1E15 atoms/cm2)
 1.8397E+00                 L.S.S. reduced units
==================================================================
(C) 1984,1989,1992,1998,2008 by J.P. Biersack and J.F. Ziegler
```

Figure 4.1: Calculation result of 5.84 MeV α-particle in BN from SRIM.

To further verify the accuracy of the simulation process, the optimal thicknesses of the two converter layers were compared with the results of previous studies [MHY+03] as shown in Tab. 4.1.

The thicknesses of the B_4C and LiF converter layers were optimised for use with semiconductors. Figure 4.3 illustrates the thickness and neutron detection efficiency curves of B_4C and LiF on a 30 μm GaN film with 300 keV LLD and 900 keV LLD. The concentrations of ^{10}B and ^{6}Li are both at their natural abundances. As depicted in Fig. 4.3, the neutron detection efficiency of the detector

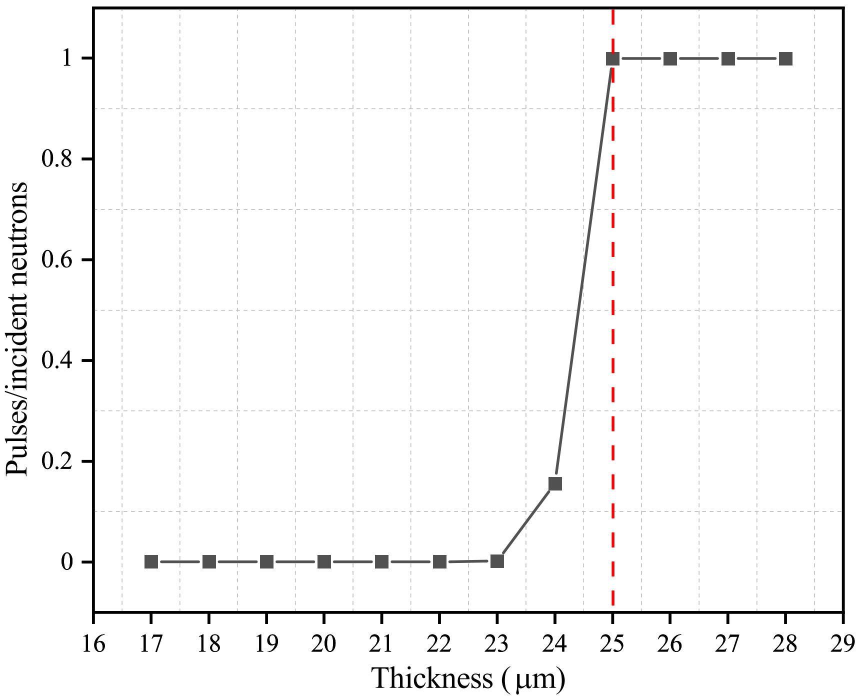

Figure 4.2: 5.84 MeV α-particle detection efficiency versus BN thickness.

rises and then falls as the thickness of the converter layer increases. According to the same figure, the optimmal thicknesses of the B_4C converter layer are about 2.6 μm (300 keV LLD) and 1.7 μm (900 keV LLD). For LiF, the optimmal thicknesses are about 30.6 μm (300 keV LLD) and 27.0 μm (900 keV LLD).

To facilitate better comparison with the results of other researchers, the enrichment levels of ^{10}B and ^{6}Li were adjusted to 99.99%. Based on that, the optimal thicknesses for 300 keV are listed in Tab. 4.1 for clarity. These results are consistent with previous studies [MHY$^+$03]. It is verified that the simulation model can correctly predict the energy loss of charged particles in the material and the self-absorption effect of the converter layer.

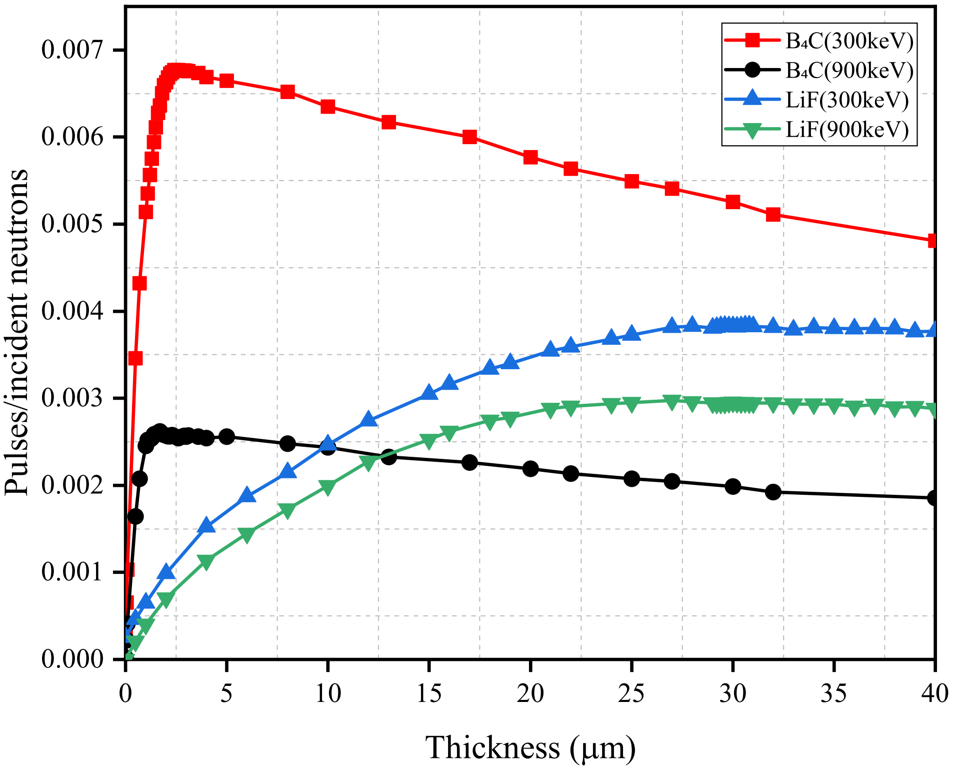

Figure 4.3: Ratio of pulses and incident neutrons as a function of converter layer thickness for a 300 keV LLD and 900 keV LLD [ZA20].

Table 4.1: Comparison converter layer thicknesses for B_4C and LiF with the results of Mcgregor et al.[MHY+03].

Converter layer	**Mcgregor et al.**[MHY+03]	**Zhongming et al.**
B_4C	$\approx 2.4\ \mu m$	$\approx 2.2\ \mu m$
LiF	$\approx 26\ \mu m$	$\approx 26.4\ \mu m$

4.2 Thickness optimisation

4.2.1 Converter layer

Figure 4.4 shows a comparative analysis between theoretical calculations and Geant4 simulations for the optimal converter layer thickness of semiconductor neutron detectors with the layered structure for varying LLD thresholds. The results illustrate a clear inverse correlation between the converter layer thickness and LLD values, suggesting that a higher LLD threshold permits a reduction in the converter layer thickness. The theoretical data, denoted by black squares, exhibits a marginally steeper descent in comparison to the Geant4 simulations, indicated by red circles, suggesting that the theoretical model predicts a slightly more pronounced thinning effect of the converter layer with increasing LLD. Both sets of data converge towards the higher LLD values, indicating a potential area of agreement between theory and simulation at elevated thresholds. This convergence could be indicative of a diminishing sensitivity to thickness variations at higher LLDs or a potential limitation in the differentiation capability of the simulation at these parameters.

Figure.4.5 furnishes a comparative analysis between theoretical calculations and Geant4 simulations concerning the LiF converter layer thickness of a semiconductor neutron detector with the layered structure across various LLD thresholds. Both theoretical and simulated datasets evince a monotonically decreasing trend,

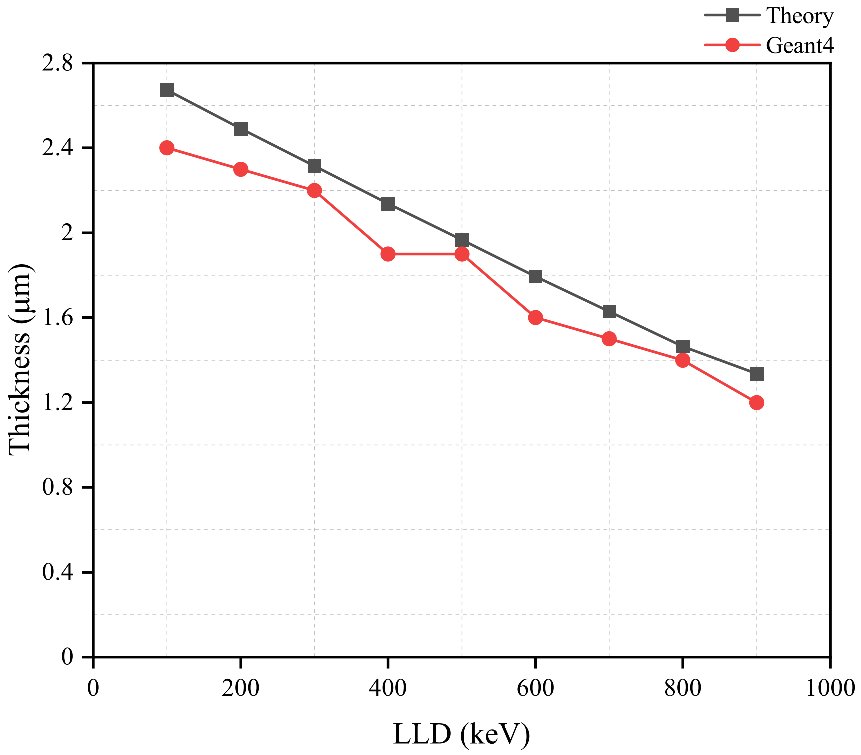

Figure 4.4: Comparative analysis of B_4C converter layer thickness at varying LLD thresholds: theory versus Geant4 simulations.

underscoring the inverse relationship between the converter layer thickness and the LLD values.

As the LLD threshold escalates, a notable discrepancy emerges between the theoretical predictions and the Geant4 simulations concerning the LiF converter layer thickness. The theoretical curve, delineated by black squares, forecasts a progressive thinning of the converter layer which becomes markedly more pronounced than the Geant4 simulation results, represented by red circles, at elevated LLD values. This divergence suggests that while both the theoretical model and the simulation align on the general trend of decreasing layer thickness with increasing LLD, they differ in their sensitivity to LLD variations at the higher end of the spectrum. This could imply a need to reassess the theoretical assumptions or the simulation parameters at these higher thresholds, as the increased difference may affect the practical application and efficiency of the neutron detector design. Further exploration into the underlying mechanisms contributing to this variation could yield improvements in the theoretical model and enhance the predictive accuracy for the optimal converter layer thickness at high LLD values.

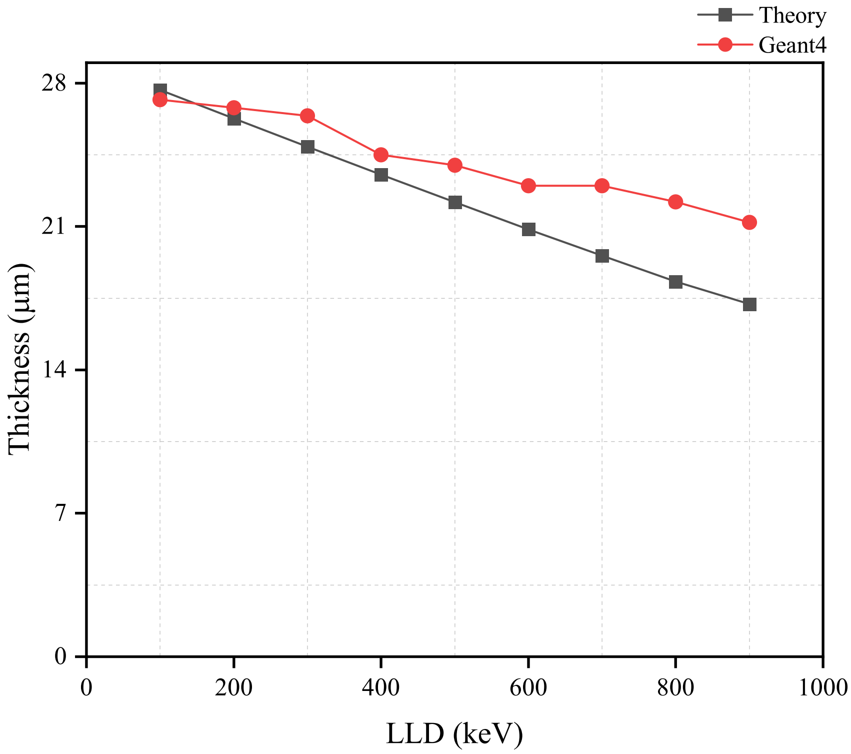

Figure 4.5: Comparative analysis of LiF converter layer thickness at varying LLD thresholds: theory versus Geant4 simulations.

4.2.2 Semiconductor layer

Optimising the thickness of the semiconductor layer is crucial to achieve high detection efficiency while keeping the semiconductor layer thin to reduce costs. By using the optimal thicknesses of the converter layer and gradually increasing the thickness of the semiconductor layer, the relationship between the thickness of various semiconductor materials and the detection efficiency was investigated. Please refer to the appendix for the related figures and tables.

The provided figures, from Fig. 1 to Fig. 10, illustrate the relationship between the thickness of five different semiconductor layers beneath B_4C or LiF converter layers and the neutron detection efficiency for various LLD settings ranging from 100 keV to 900 keV. With the simulation configuration as discussed in the methodology chapter, these results demonstrate the optimal thicknesses of the five semiconductor layers.

In terms of qualitative analysis, for the five materials with B_4C converter layers, it is observed from the figures that the detection efficiency increases with the thickness of the semiconductor layer, reaching a stable state at different thicknesses depending on the LLD settings. However, the rate of efficiency increase varies for different LLD, with higher LLD resulting in a slower increase.

For the five materials with LiF converter layers, the observed phenomenon is similar to that with B_4C layers. However, for different LLD, with LiF as the converter layer, the rate of increase in neutron detection efficiency with increasing semiconductor thickness is greater than when B_4C is the converter layer, especially for higher LLD energy. Additionally, when the converter layer is LiF, the decay of maximum detection efficiency with increasing LLD is less pronounced.

It is noteworthy that the maximum detection efficiency is inversely proportional to the LLD; as the LLD increases, the maximum detection efficiency decreases. These curves indicate that the efficiency return diminishes with increasing semiconductor thickness, especially for high LLD. This suggests that there is an optimal semiconductor thickness for each LLD setting to achieve maximum detection efficiency, and this optimal thickness increases with the LLD.

To more clearly present the optimal thicknesses for different LLD, detailed data are displayed from Tab. 1 to Tab. 10. Drawing from these findings, the quantitative analysis indicates that across both converter layer types and various LLD settings, diamond invariably presents the minimum optimal thickness among the five materials. Conversely, $CsPbBr_3$ consistently exhibits the greatest optimal thickness.

4.3 Threshold displacement energy of $CsPbBr_3$

For radiation damage caused by neutrons, the main type of damage is displacement damage. To model displacement damage, it is necessary to determine the TDE of the material. The TDE has been reported for diamond, SiC, Ga_2O_3, and GaN. However, as mentioned in the earlier chapter, at the time of writing, the TDE of $CsPbBr_3$ has not been reported. Therefore, this section employs the LAMMPS to find the TDE of $CsPbBr_3$. The average TDE for three atom sites are presented in Tab. 4.2. Furthermore, the TDE for 361 directions (ϕ from 0^o to 90^o, θ from 0^o to 90^o with a 15^o increment each time) under different temperatures are shown in Fig. 4.6, Fig. 4.7 and Fig. 4.8. The displacement energy ranges from 76.86 eV to 80.69 eV for Cs, from 58.64 eV to 69.84 eV for Pb, and from 70.19 eV to 97.03 eV for Br.

TDE **T (K)** **Site**	**100**	**200**	**300**	**400**
Cs	76.86	80.69	80.12	76.96
Pb	69.84	68.28	63.24	58.64
Br	70.19	81.25	97.03	90.47
Average	71.45	78.55	86.89	81.40

Table 4.2: Threshold displacement energies (eV) for each site and different temperature.

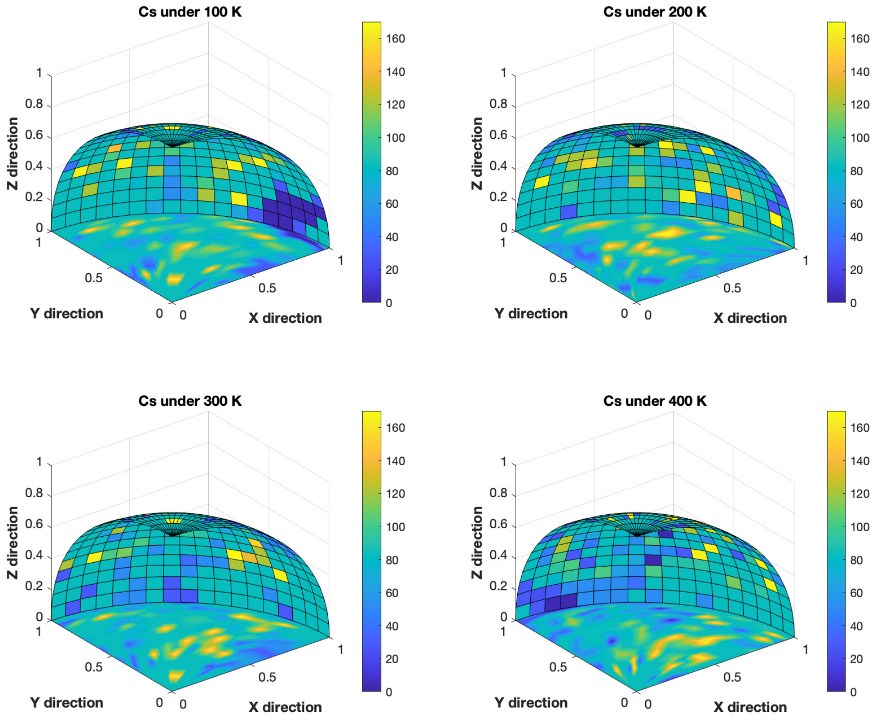

Figure 4.6: Spatial distribution of TDE for Cs site. The unit of the temperature scale is eV.

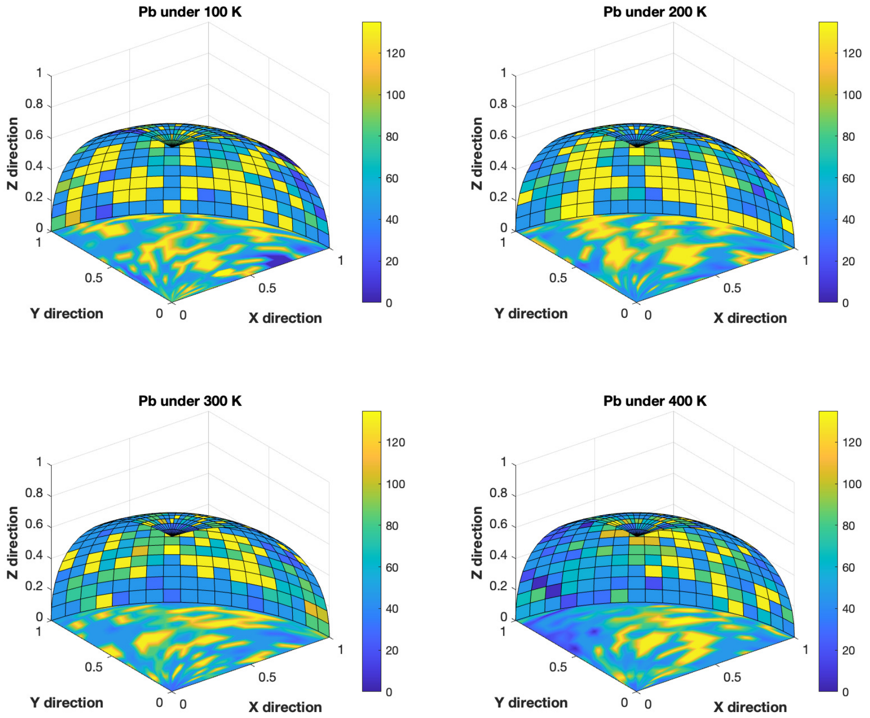

Figure 4.7: Spatial distribution of TDE for Pb site. The unit of the temperature scale is eV.

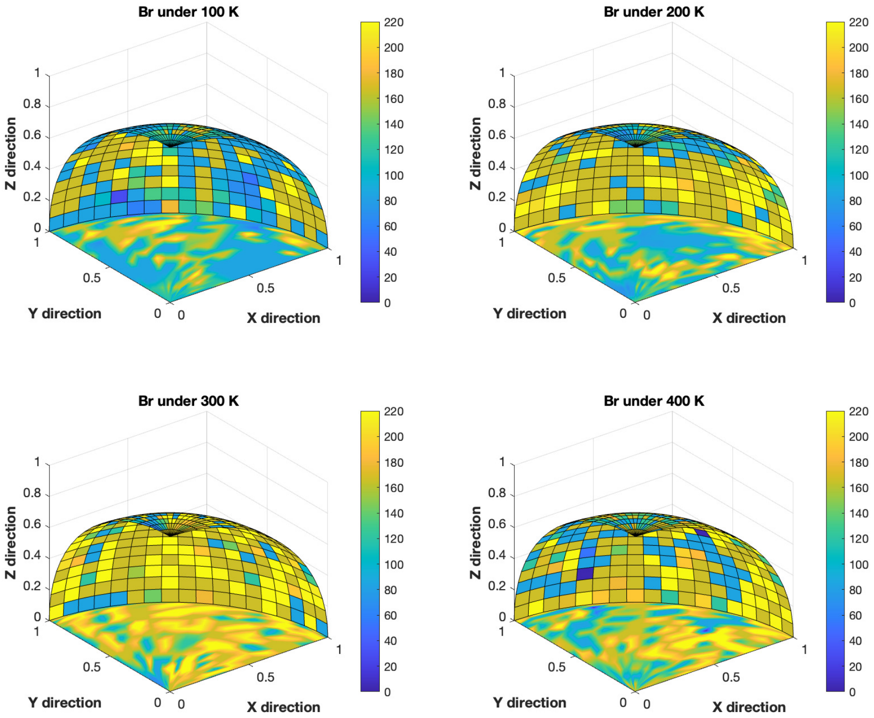

Figure 4.8: Spatial distribution of TDE for Br site. The unit of the temperature scale is eV.

4.4 Microscopic neutron radiation resistance

The section concerning radiation displacement damage has already been introduced in the methodology chapter; a brief overview of this can be provided here. One of the reactions between neutrons and a nucleus is elastic scattering. When an incident neutron with high energy strikes the nucleus, there is a chance that the nucleus will be knocked out of the lattice.

Although thermal neutrons comprise the majority of neutrons in nuclear power plants, moderator leakage could occur in the event of a nuclear accident, leading to the release of high-energy neutrons from the exposed core. Therefore, if the neutron flux of a nuclear reactor is to be monitored in the event of an accident, the detector material needs to be radiation-resistant. This section examines the radiation damage and radiation resistance capabilities of indirect detection materials, diamond, SiC, Ga_2O_3, GaN and $CsPbBr_3$.

Giving more details, this part presents the simulated PKA energy spectrum generated by a 1 MeV neutron flux for the five materials that were modelled. The atomic displacements are then calculated using Eq. 3.15. The DPA is determined by dividing the atomic displacements by the total number of atoms in the material. A smaller DPA indicates that the atoms are less likely to leave their lattice positions, and so can be used as a measure of the radiation hardness of the material. In reality, there is a possibility that an atom may return to its lattice position after being knocked out by a neutron. However, the DPA still has significance for the qualitative analysis of the radiation hardness of materials performed by this study.

Through Fig. 4.9, Fig. 4.10, Fig. 4.11, Fig. 4.12, and Fig. 4.13, along with Tab. 4.3, the average PKA energies and the corresponding DPA values for five different materials can be ascertained. For a neutron beam with an energy of $1\ MeV$, the converter layers offer limited neutron shielding; hence, the disparity in DPA values across the five materials with two different types of converter layer material is not significant.

According to Fig. 4.9, for diamond, the energy distribution of PKAs is relatively even, and the average PKA energy is highest among these materials. The spectrum for SiC and $CsPbBr_3$, Fig. 4.10 and Fig. 4.13, are very similar, with a greater number of low-energy PKAs and fewer high-energy PKAs. The energy spectrum of Ga_2O_3, as shown in Fig. 4.11, exhibits two distinct peaks, one in the low-energy region and the other in the high-energy region. This is conjectured to be due to two different types of PKAs, corresponding to Ga and O atoms. Although Fig. 4.12 does not display two distinct PKA peaks, there is a precipitous drop in the spectrum at around $50\ eV$ to $60\ eV$, which is hypothesised to be the boundary between the PKAs of N and Ga types.

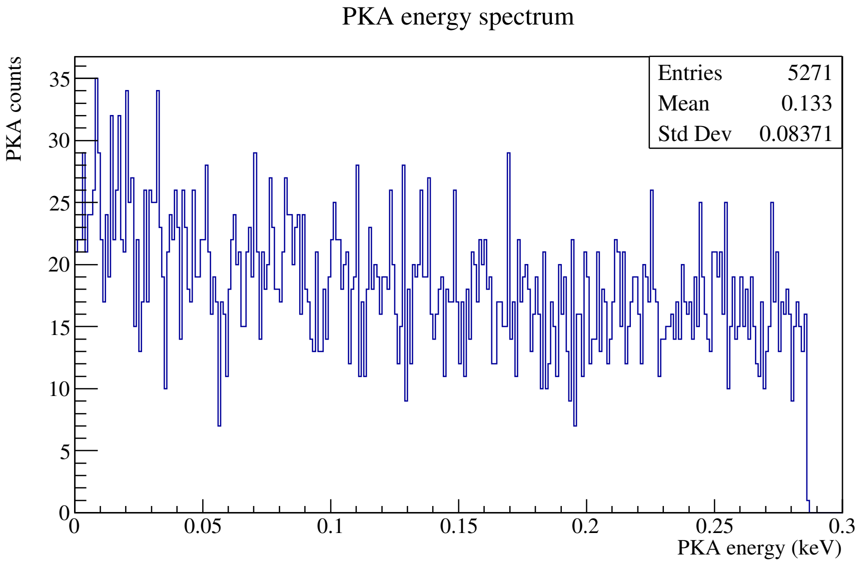

Figure 4.9: Primary knock-on atoms energy spectrum for diamond. This energy spectrum was created by ROOT. The X-axis shows the energy of PKA in keV. The Y-axis shows the count number of PKA. The figure keys show: Entries, the total number of PKA; Mean, the average PKA energy in keV; and Std Dev, the standard deviation of PKA energy (keV).

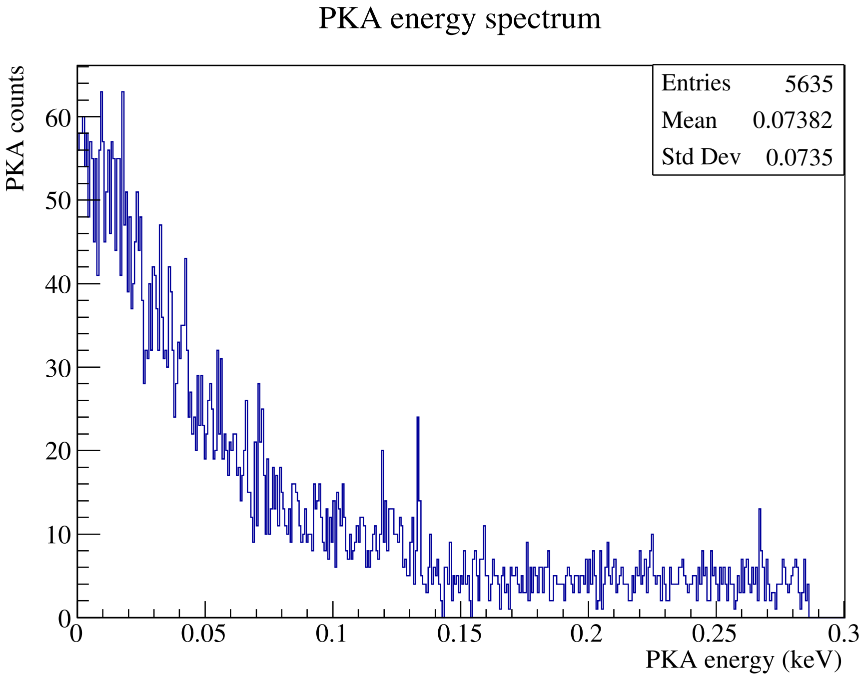

Figure 4.10: Primary knock-on atoms energy spectrum for SiC. This energy spectrum was created by ROOT. The X-axis shows the energy of PKA in keV. The Y-axis shows the count number of PKA. The figure keys show: Entries, the total number of PKA; Mean, the average PKA energy in keV; and Std Dev, the standard deviation of PKA energy (keV).

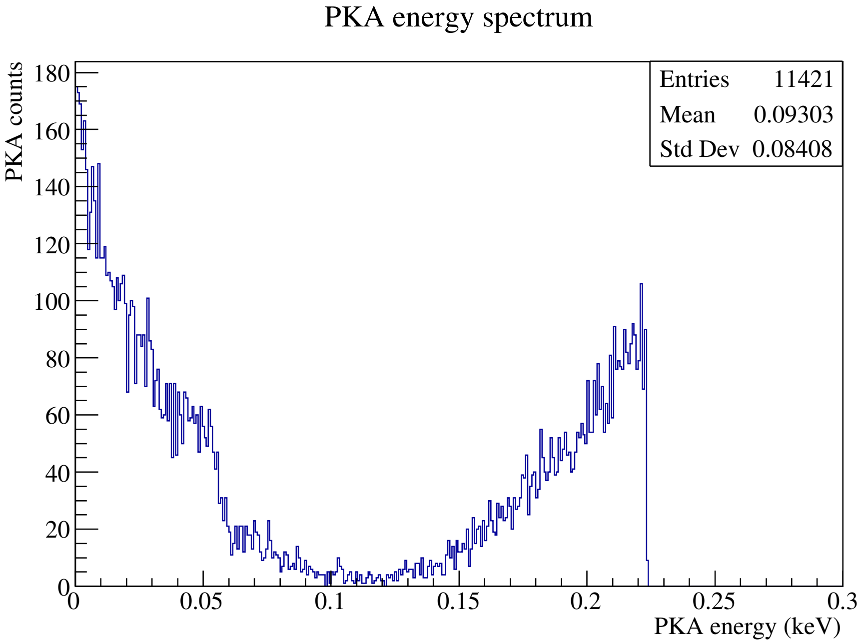

Figure 4.11: Primary knock-on atoms energy spectrum for Ga_2O_3. This energy spectrum was created by ROOT. The X-axis shows the energy of PKA in keV. The Y-axis shows the count number of PKA. The figure keys show: Entries, the total number of PKA; Mean, the average PKA energy in keV; and Std Dev, the standard deviation of PKA energy (keV).

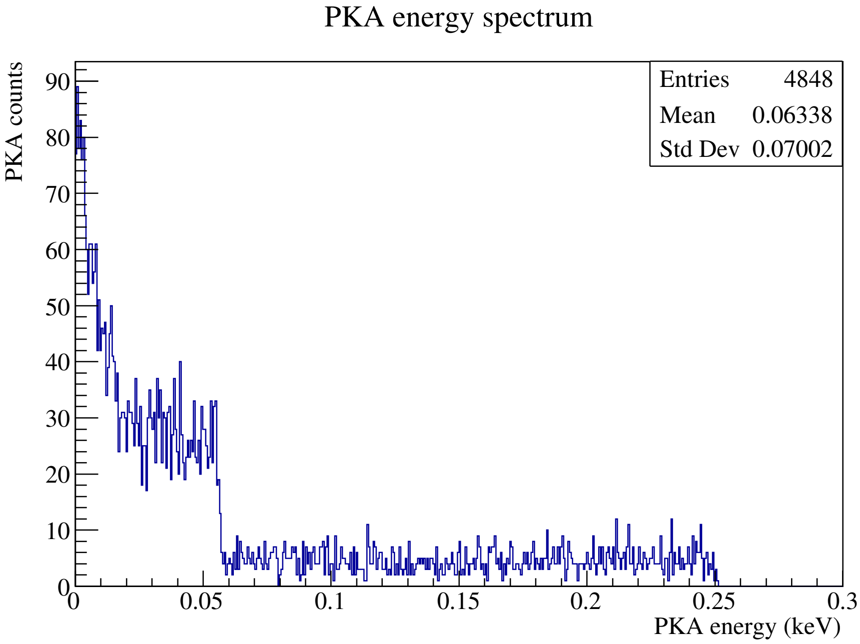

Figure 4.12: Primary knock-on atoms energy spectrum for GaN. This energy spectrum was created by ROOT. The X-axis shows the energy of PKA in keV. The Y-axis shows the count number of PKA. The figure keys show: Entries, the total number of PKA; Mean, the average PKA energy in keV; and Std Dev, the standard deviation of PKA energy (keV).

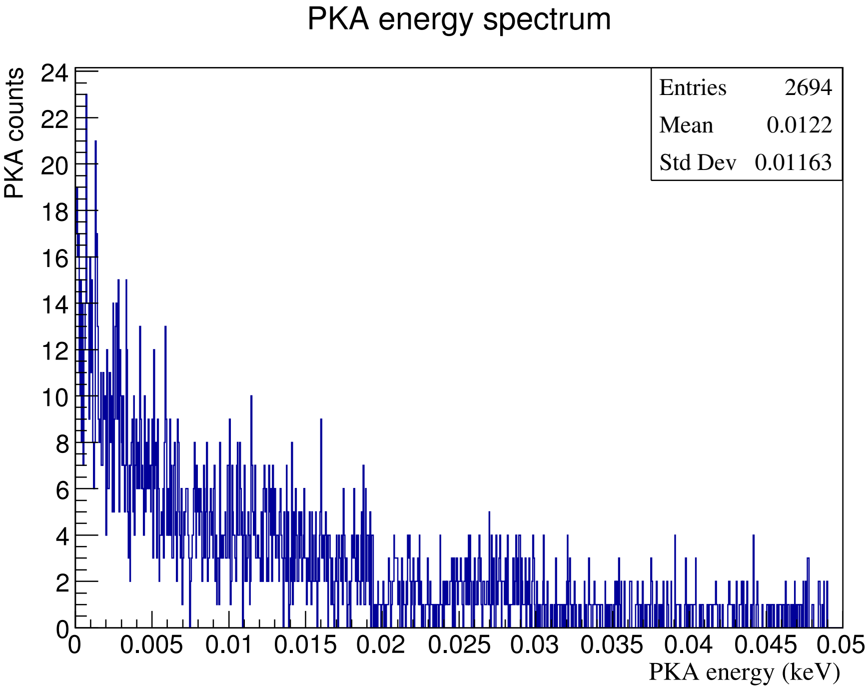

Figure 4.13: Primary knock-on atoms energy spectrum for $CsPbBr_3$. This energy spectrum was created by ROOT. The X-axis shows the energy of PKA in keV. The Y-axis shows the count number of PKA. The figure keys show: Entries, the total number of PKA; Mean, the average PKA energy in keV; and Std Dev, the standard deviation of PKA energy (keV).

Table 4.3: Displacements per atom and average primary knock-on atoms energy of five materials under a 1 MeV neutron flux. (The thicknesses of B_4C and LiF are 2.6 μm and 30.6 μm)

	Diamond	**SiC**	**Ga_2O_3**	**GaN**	**$CsPbBr_3$**
DPA ($\times 10^{-20}$)(B_4C)	1.30	4.12	6.83	1.01	0.12
DPA ($\times 10^{-20}$)(LiF)	1.29	4.05	6.72	0.99	0.13
Average PKA energy (keV)	134.30	73.68	92.33	63.28	11.55

4.5 Gamma rejection capability

The γ-ray rejection capability of the five semiconductor materials was investigated in this study. Figures 4.14, Fig. 4.15, Fig. 4.16, Fig. 4.17 and Fig. 4.18 illustrate the intrinsic photon detection efficiency versus the semiconductor thickness for 300 keV LLD for the two converter layers with γ-ray energy range from 0.5 MeV to 1.5 MeV.

As mentioned in the methodology chapter, to avoid any 'false-positive' neutron counts, the intrinsic γ-ray detection efficiency for semiconductor materials should be less than 10^{-6} [MKM+12]. The results of the study showed that when the thicknesses of the five indirect semiconductor materials examined were optimised, their intrinsic γ-ray detection efficiencies were all less than 10^{-6}. Therefore, all the studied materials meet the basic requirements for γ-ray rejection, provided they are used with optimal thicknesses.

To meet the requirement of a γ-ray intrinsic detection efficiency lower than 10^{-6}, the maximum allowable thicknesses of the five semiconductors with two types of converter layers are presented in Tab. 4.4 and Tab. 4.5. According to the tables, the maximum allowable thickness of the semiconductor layer tends to decrease as the energy of the γ ray increases. When examining the effects of different converter layers, the maximum allowable thickness is greater for B_4C compared to LiF. This is contrary to expectations, as LiF is significantly thicker than B_4C and should theoretically block some γ rays, potentially leading to an increased maximum allowable thickness; however, simulation results show the opposite. For different γ-ray energies, GaN, Ga_2O_3, and $CsPbBr_3$ exhibit a relative insensitivity to γ-ray energy, with the maximum allowable thicknesses showing little variation from 0.5 MeV to 1.5 MeV. When sorted by maximum allowable thickness for the same type of converter layer, the rank from smallest to largest is as follows: Ga_2O_3, GaN, $CsPbBr_3$, diamond, and SiC.

Table 4.4: Maximum allowable semiconductor thickness in order to get a γ-ray intrinsic detection efficiency smaller than 10^{-6} with 2.32 μm B_4C converter layer for 300 keV LLD with γ-ray range from 0.5 MeV to 1.5 MeV.

Gamma Energy (MeV)	Diamond (μm)	SiC (μm)	Ga_2O_3 (μm)	GaN (μm)	$CsPbBr_3$ (μm)
0.5	63	62	27	29	35
0.6	61	58	28	28	37
0.7	59	59	27	29	37
0.8	58	57	28	29	39
0.9	53	57	28	29	38
1.0	52	54	27	29	38
1.1	54	55	28	28	39
1.2	52	55	28	28	40
1.3	50	51	28	29	39
1.4	47	50	27	28	38
1.5	46	50	26	27	38

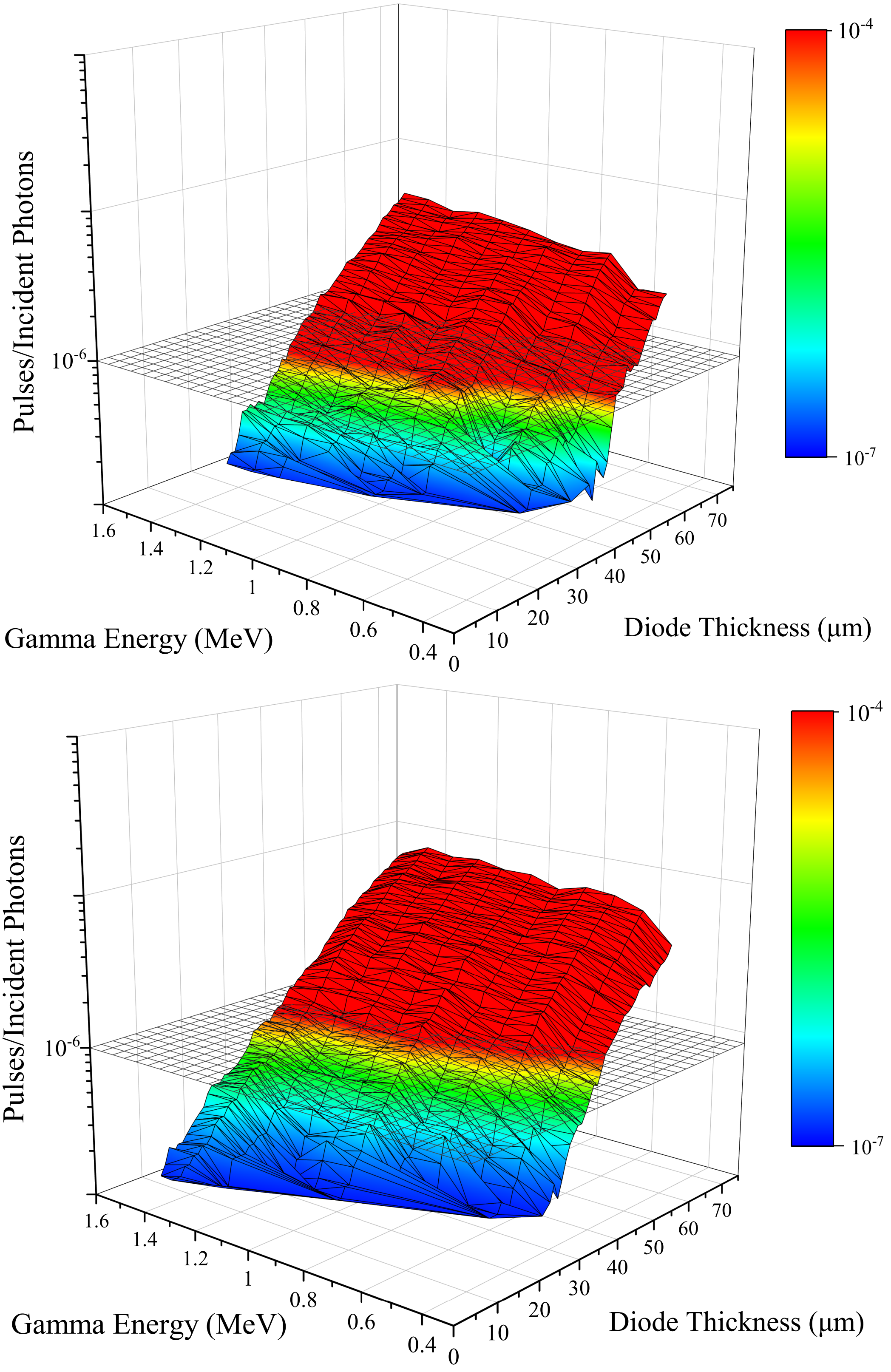

Figure 4.14: Gamma-ray detection efficiency to γ-ray energy range from 0.5 MeV to 1.5 MeV versus semiconductor thickness for 300 keV LLD with optimal B_4C (top) and LiF (bottom) converter layer thickness for diamond. The optimal thicknesses for B_4C and LiF converter layer are 2.32 μm and 24.89 μm.

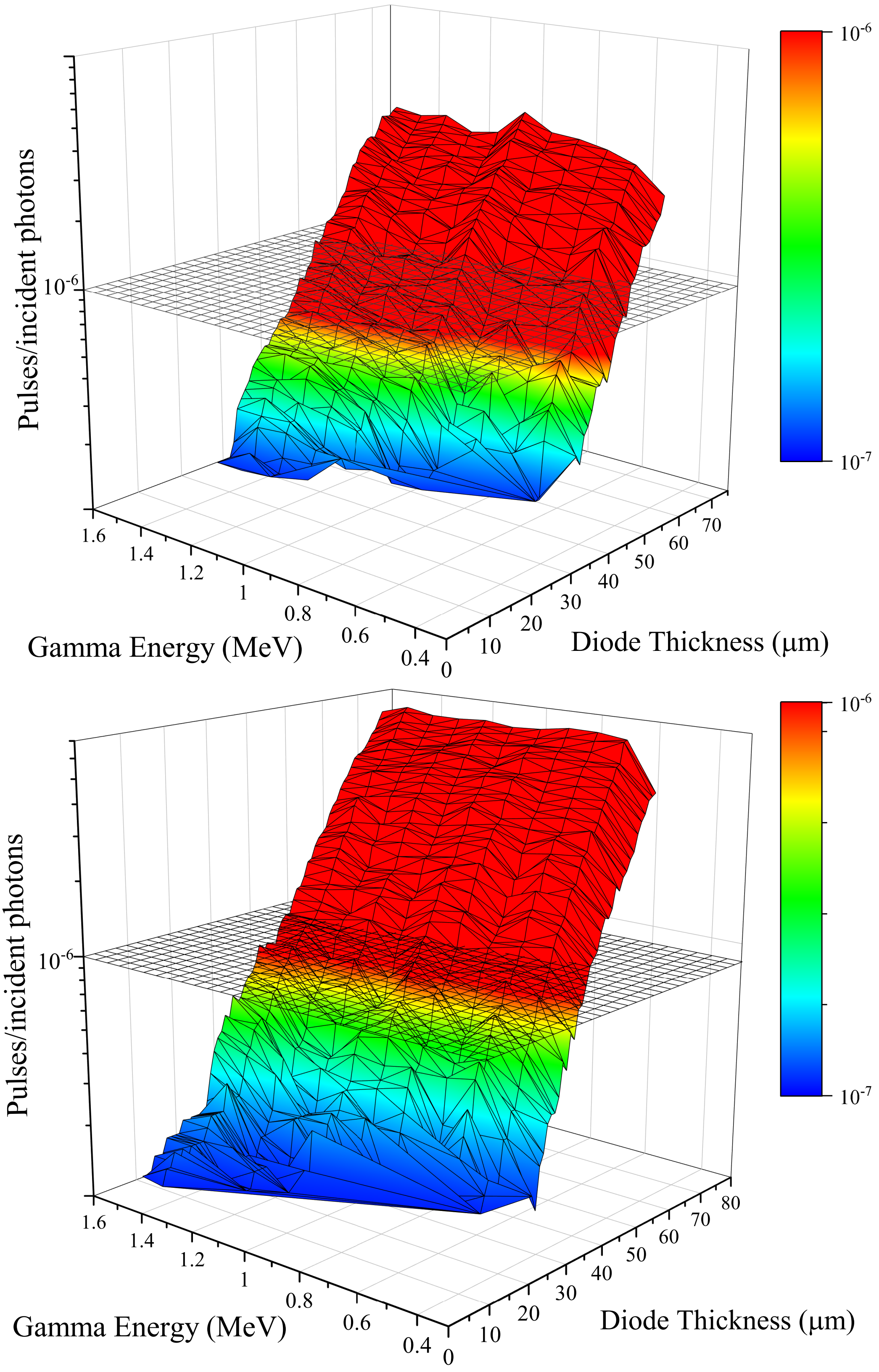

Figure 4.15: Gamma-ray detection efficiency to γ-ray energy range from 0.5 MeV to 1.5 MeV versus semiconductor thickness for 300 keV LLD with optimal B_4C (top) and LiF (bottom) converter layer thickness for SiC. The optimal thicknesses for B_4C and LiF converter layer are 2.32 μm and 24.89 μm.

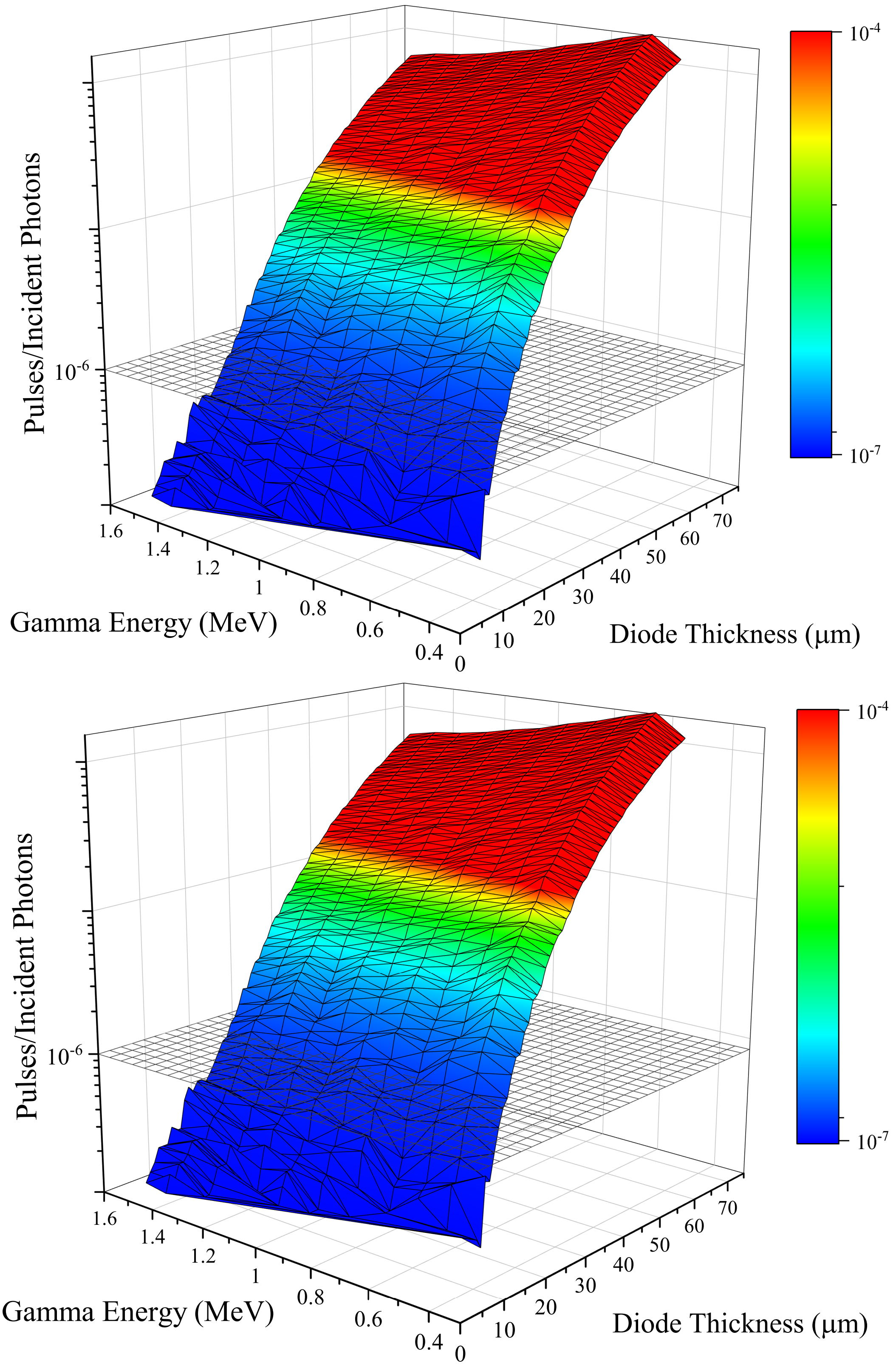

Figure 4.16: Gamma-ray detection efficiency to γ-ray energy range from 0.5 MeV to 1.5 MeV versus semiconductor thickness for 300 keV LLD with optimal B_4C (top) and LiF (bottom) converter layer thickness for Ga_2O_3. The optimal thicknesses for B_4C and LiF converter layer are 2.32 μm and 24.89 μm.

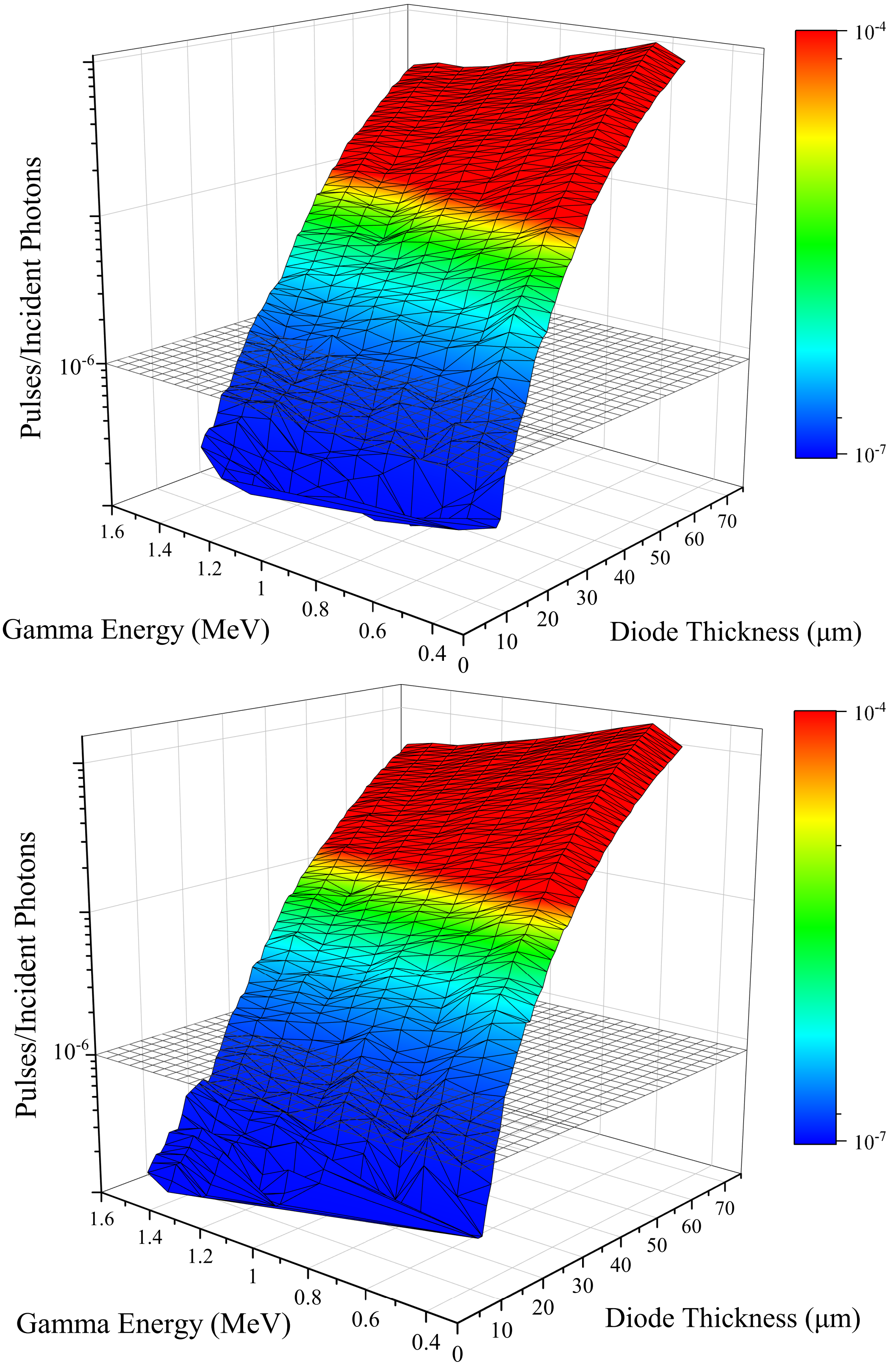

Figure 4.17: Gamma-ray detection efficiency to γ-ray energy range from 0.5 MeV to 1.5 MeV versus semiconductor thickness for 300 keV LLD with optimal B_4C (top) and LiF (bottom) converter layer thickness for GaN. The optimal thicknesses for B_4C and LiF converter layer are 2.32 μm and 24.89 μm.

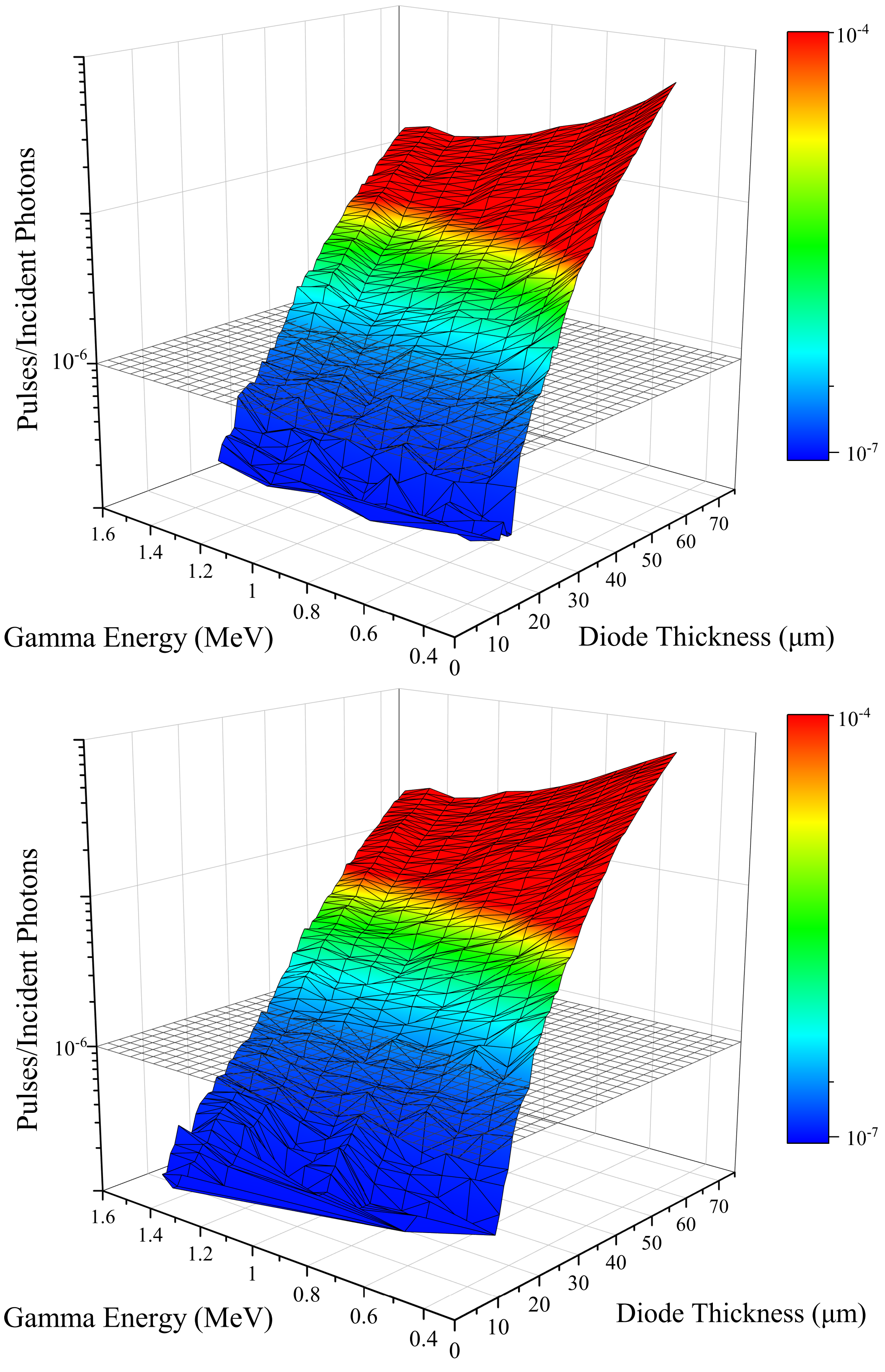

Figure 4.18: Gamma-ray detection efficiency to γ-ray energy range from 0.5 MeV to 1.5 MeV versus semiconductor thickness for 300 keV LLD with optimal B_4C (top) and LiF (bottom) converter layer thickness for $CsPbBr_3$. The optimal thicknesses for B_4C and LiF converter layer are 2.32 μm and 24.89 μm.

Table 4.5: Maximum allowable semiconductor thickness in order to get a γ-ray intrinsic detection efficiency smaller than 10^{-6} with 24.89 μm LiF converter layer for 300 keV LLD with γ-ray range from 0.5 MeV to 1.5 MeV.

Gamma Energy (MeV)	Diamond (μm)	SiC (μm)	Ga_2O_3 (μm)	GaN (μm)	$CsPbBr_3$ (μm)
0.5	53	52	25	25	32
0.6	51	49	24	25	34
0.7	47	48	24	25	32
0.8	46	48	25	26	34
0.9	44	47	24	25	35
1.0	40	45	23	25	34
1.1	42	47	24	25	35
1.2	41	46	24	25	34
1.3	41	45	24	25	34
1.4	39	44	23	24	34
1.5	38	44	24	24	32

Chapter 5

Discussion

In this chapter, an analysis and comparison of the optimal thicknesses of certain converter and semiconductor materials used in neutron detection have been conducted. The primary objective is to delve deeper into discussions and analyses on the basis of the previous chapter, to explain why the respective results were obtained. The first part has studied the issue of thickness optimisation, including the optimisation of converter layer thickness and semiconductor layer thickness. The second part has further discussed and compared the impact of neutron radiation on five semiconductor materials at the microscopic level. Finally, the γ-ray rejection capabilities of the five materials have been explored, which can facilitate the discrimination between neutron and γ signals.

5.1 Thickness optimisation

5.1.1 Converter layer

The trends in optimal thicknesses of the converter layers obtained from theoretical calculations and Monte Carlo (MC) simulations are consistent, as shown in Fig. 4.5 and Fig. 4.4. For both types of converter materials, an increasing trend in LLD energy results in a decrease in the optimal thickness, attributed to the essentially fixed energy of secondary charged particles. As the LLD energy increases, the secondary charged particles must deposit more energy in the semiconductor layer to yield a true count. This implies that after their generation, the secondary charged particles need to deposit less energy in the converter layer, necessitating a reduction in its thickness. This is because, for detectors aimed at forward detection, the deeper the neutron beam penetrates into the converter material, the lower its intensity.

It is observed from the figures that for the B_4C converter layer, the optimal thicknesses obtained from theory and MC simulations closely align. Given the statistical nature of MC simulations, which inherently contain statistical error, this result is considered acceptable. However, for the LiF converter layer, while the theoretical calculations and MC simulations match well at lower LLD energies, a noticeable gap exists at higher LLDs, particularly above 600 keV. Two main reasons may have been identified for this discrepancy.

Firstly, although the range of charged particles in BN was verified in the first part of the results chapter, where Geant4 and SRIM results were found to be very close, there are differences in the treatment of the Beth-Block equation by Geant4 and SRIM for high-energy incident charged particles ($v > v_0 Z^{2/3}$, v represents the velocity of the incident particle, v_0 is the Bohr velocity, and Z is the proton number of the target nucleus). This discrepancy is primarily attributed to the differences in the correction factors [PLY16]. Thus, at lower LLD energies, the differences in treatment of charged particle range by Geant4 and SRIM are not significantly manifested. However, at higher LLD energies, minor differences in range are magnified, leading to the observed discrepancies.

Secondly, the reaction of thermal neutrons with LiF releases an energy of 4.79 MeV, typically with ^{3}H having an initial kinetic energy of 2.73 MeV and α particles having an initial kinetic energy of 2.06 MeV [MPA$^+$19]. However, in reality, the energy distribution may not strictly follow these rules. Hence, ^{3}H or α particles with different energies in LiF have different ranges, adding errors to the theoretical calculations.

In summary, the formula for calculating the optimal thickness of the converter layer, based on theoretical derivation, has performed well in predicting the dual secondary charged particle mode. However, at higher LLD energies, some discrepancies have been observed between it and the MC simulation results for LiF converter layer.

5.1.2 Semiconductor layer

As shown in the results chapter, with the B_4C or LiF converter layer, the optimal thicknesses of five semiconductor neutron detectors with LLD energy range from 100 keV to 900 keV were investigated. Although it was initially assumed that the optimal thickness corresponded to the range of charged particles, such as α-particle produced in the nuclear reaction with the converter layer, it was found, upon comparison with SRIM calculations, that this assumption was not correct.

The range of heavy charged particles in matter

The moderation of charged particles in target materials is entirely the result of various interactions between the charged particles and the electrons and nuclei of the target material atoms, predominantly governed by coulomb interactions. When the energy of the incident charged particles is high, they undergo multiple collisions with the extranuclear electrons or nuclei of the target material atoms, resulting in energy transfer. As the energy of the incident charged particles gradually decreases, charge exchange effects occur. If the target material is sufficiently thick, ultimately, all the energy of the charged particles will be deposited within the target material. There are primarily four processes involved:

1. Inelastic collisions with extranuclear electrons.

2. Elastic collisions with atomic nuclei.
3. Inelastic collisions with atomic nuclei.
4. Elastic collisions with extranuclear electrons.

Inelastic collisions between charged particles and the extranuclear electrons of target atoms, leading to ionisation or excitation of the atoms, are the primary means by which charged particles lose kinetic energy when passing through matter. As the energy of the charged particles decreases, the process of elastic collisions with atomic nuclei gradually increases.

Incident charged particles may also penetrate the Coulomb barrier of the nucleus and undergo nuclear reactions, but this does not affect the moderation of charged particles in matter. According to the Beth-Block formula, since in this study, for each converter layer, the particle energy and type are the same, the main differences are related to the target material, which is the semiconductor layer, its density, and atomic number. Materials with high atomic numbers and high densities possess greater stopping power, also implying a lower optimal thickness. Subsequent analyses are based on this inference.

General discussion

As shown from Fig. 1 to Fig. 10, the detection efficiencies of various indirect-detection semiconductor materials were observed to have an initial increase followed by an asymptotic approach to a constant efficiency. With a fixed thickness of the converter layer, the number of charged particles generated and absorbed could be determined and changes in the detection efficiencies were primarily attributed to variations in the thickness of the semiconductor layer.

When the semiconductor is thin, most charged particles lose some energy and then escape. As the thickness of the semiconductor layer increases, more energy is deposited within the material. An optimal thickness is ultimately reached, where all charged particles deposit all their energy in the semiconductor. Beyond this optimal thickness, the detection efficiency does not improve any further because all charged particles have lost all their energy in the semiconductor layer.

As can be seen from Tab. 1 to Tab. 10, when semiconductor materials are equipped with a B_4C converter layer, their optimal thickness is smaller than when they are equipped with an LiF converter layer. This is mainly due to the larger energy produced by the reaction between neutrons and Li, as shown in Eq. 1.1 and Eq. 1.2. This causes the charged particles generated by the reaction between Li and neutrons to have a larger kinetic energy, requiring a thicker semiconductor layer to allow the charged particles to lose their energy completely.

Regarding the influence of different LLD energies on the maximum detection efficiency, it is observed that the rate of decay in maximum detection efficiency for detectors with B_4C converter layers is faster than that for detectors with LiF layers as the LLD energy increases. Taking diamond detectors as an example, with a B_4C converter layer, the maximum detection efficiency at an LLD energy of 100 keV is 3.75%, which decays to 1.25% at 900 keV, a reduction of 66.7%. In contrast, with a LiF layer, the maximum detection efficiency at an LLD energy of 100 keV is 4.6%, which decreases to 3.5% at 900 keV, a reduction of 23.9%. One possible reason for this phenomenon is the range of secondary charged particles. For B_4C converter layers, at an LLD energy of 900 keV, all counts are contributed by alpha particles, whereas for LiF layers, both types of secondary charged particles still have a significant range. Thus, this leads to a rapid decay in the maximum detection efficiency of detectors with B_4C converter layers as LLD energy changes.

Materials

Based on comparative analysis, it was determined that diamond performed well as a material for the two converter layer materials, with an optimal thickness that is relatively small. This result can potentially be attributed to the high electron density outside the nucleus of the diamond. The distribution of electron density is a complex quantum mechanical issue, typically requiring advanced computational methods like Density Functional Theory (DFT) for more precise determination. Here, it is simply assumed to be proportional to the electron density outside the nucleus, based on atomic density. Given that diamond possesses the highest atomic density among these five materials, it can be conjectured that it also has a relatively high electron density outside the nucleus. The increased electron density makes it more likely for charged particles to collide and interact with electrons upon entering the diamond, thereby increasing the likelihood of energy loss. Furthermore, diamond possesses the lowest relative atomic mass among the five materials, implying that as the energy of charged particles decreases and the number of elastic collisions with atomic nuclei increases, more energy will be lost by the charged particles in a single collision. In short, charged particles will quickly lose all their energy in the diamond, resulting in the smallest optimal thickness among the five materials.

When a B_4C converter layer is combined with GaN, the optimised thickness is greater than that of diamond. However, when combined with LiF, the optimised thickness and intrinsic detection efficiency for GaN and diamond are similar. Nevertheless, for the reasons explained above, the detection efficiency of GaN with a LiF converter layer is nearly 50% lower compared to that of GaN with a B_4C converter layer. Thus, B_4C is deemed more suitable as a converter layer for GaN detectors.

For SiC, regardless of whether the converter layer is B_4C or LiF, its optimal thickness is larger than that of diamond, GaN, and Ga_2O_3. However, when the converter layer is B_4C, the difference in optimal thickness between SiC and the aforementioned three materials is not significant. Therefore, if one wishes to use thinner SiC for detection, B_4C is a better converter layer choice. Furthermore, as SiC semiconductor devices are more widely manufactured and the processes involved are more mature, a comprehensive study accounting for an external electric field can provide a better assessment of the suitability and performance of SiC.

Interestingly, when combined with LiF, Ga_2O_3 exhibits superior performance with the lowest optimised thickness among the four materials. When the choice of converter layer is limited to LiF, Ga_2O_3 would be the best option among these materials. However, regarding detection efficiency, a B_4C converter layer is preferred for Ga_2O_3 as it requires a lower semiconductor thickness and has higher detection efficiency than with the LiF converter layer.

For the two converter layer materials and the two LLD energies, $CsPbBr_3$ has the largest optimal thickness among the five materials. The heavily charged particles released in the reaction between neutrons and the converter layer are mostly in the MeV energy range. The heavy charged particles with this energy level mainly interact with the valence electrons of the semiconductor atoms to generate ionisation inside the material. According to the relativistic modified Bethe-Block equation [Bet30], matters with greater density and relative atomic mass has a stronger ability to block heavy charged particles. The simulation results show that $CsPbBr_3$ has the highest relative atomic mass among the five non-directly probed materials, but its neutron-optimised thickness is the largest.

After careful deliberation, the explanation for this phenomenon is that the density of $CsPbBr_3$ in the simulations is at 4.42 g/cm^3, which is not dense, and the atomic density of $CsPbBr_3$ is approximately 2.2953×10^{22} $atoms/cm^3$. In contrast, the atomic density of diamond is 1.7849×10^{23} $atoms/cm^3$. As the atomic density of $CsPbBr_3$ is smaller than the other four materials, this is likely to result in a lower electron density outside the nucleus. In addition, it can be deduced that, as the energy of the incident charged particles decreases and they increasingly undergo elastic collisions with atomic nuclei, due to the lower atomic density, the probability of this process occurring is also lower in comparison to other materials. Moreover, as the three types of atoms in $CsPbBr_3$ have higher atomic numbers, the energy transferred by the charged particles in a single elastic collision is also lower than in other materials. Thus, it can be concluded that $CsPbBr_3$ has a weaker stopping power for heavily charged particles and therefore has a thicker optimal thickness.

5.2 Microscopic neutron irradiation damage

5.2.1 Threshold displacement energy of $CsPbBr_3$

Table. 4.2 demonstrates that for both the Cs and Br atom sites, the average TDE increases with temperature until it reaches 300 K, after which it decreases as the temperature increases further. However, this trend is not observed in the case of the Pb atom site. This phenomenon is attributed to the temperature dependence of the TDE, which is a consequence of the interaction between a neutron and a PKA. When a neutron imparts kinetic energy to the PKA, the PKA moves and collides with surrounding atoms, initiating a cascade of atomic collisions that leads to the formation of numerous Frenkel defect pairs. As illustrated in Fig. 5.1, these Frenkel defect pairs are not necessarily permanent, and there is a possibility that the atoms that were dislodged from their sites may be pulled back by interatomic potentials. This phenomenon results in a higher TDE than the formation energy of the Frenkel defect.

Additionally, this phenomenon is more likely to occur at higher temperatures, which is why the TDE increases initially with rising temperature. However, the TDE decreases beyond a specific temperature because the atom's thermal motion is amplified, leading to a balance between the kick-off and recombination stages, influenced by temperature. Interestingly, in this study, Tab. 4.2 shows that the average TDE of Pb decreases continuously as the temperature increases. This

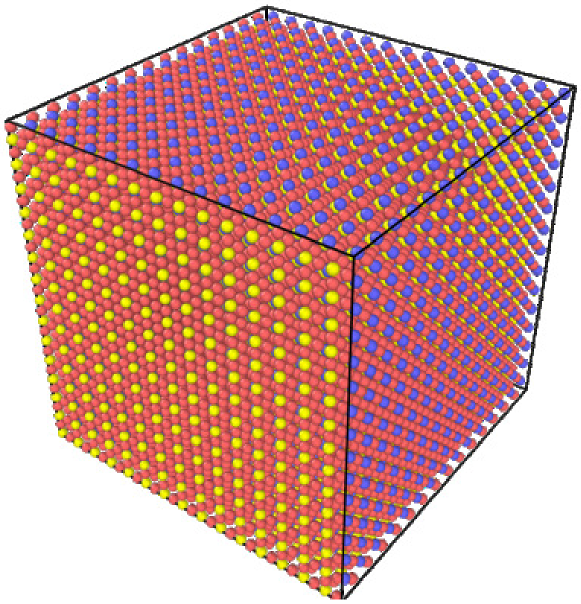

(a) $CsPbBr_3$ crystal in simulation

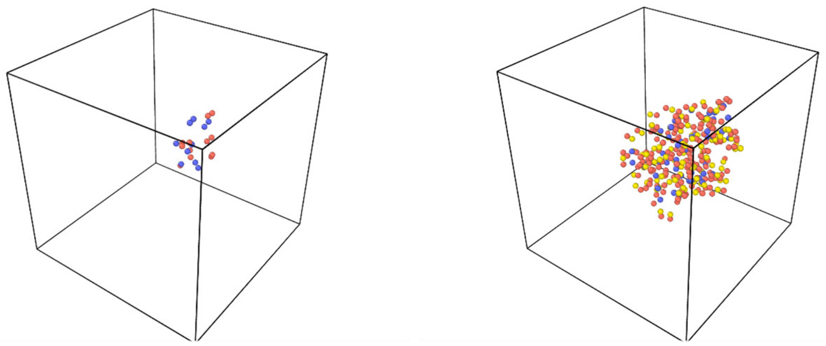

(b) 4.32 *ps* (c) 8.32 *ps*

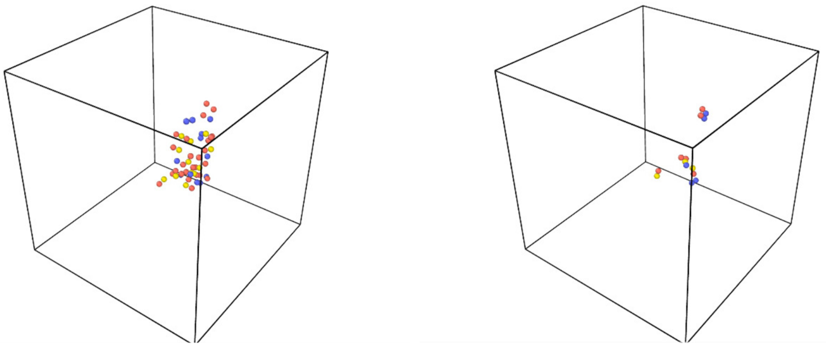

(d) 12.72 *ps* (e) 14.99 *ps*

Figure 5.1: View of simulation model in LAMMPS and view of the spatial distribution of interstitial atoms evolving over time in $CsPbBr_3$. The red ball represents Br atom, the blue ball represent Pb atom and the yellow ball represents Cs atom. (a) represents the crystal structure of $CsPbBr_3$ before the simulation, while (b) to (e) illustrate the spatial distribution of interstitial atoms at a specific moment following the initiation of a cascade collision.

observation could be attributed to the fact that Pb has the largest mass among the three types of atoms considered, making its atomic motion highly inert and prone to form stable defects. Furthermore, as mentioned earlier, higher temperatures enhance the thermal motion of Pb, making it difficult to stop a Pb PKA.

5.2.2 Displacement per atom

The materials in ascending DPA order are $CsPbBr_3$, GaN, diamond, SiC and Ga_2O_3. This indicates that $CsPbBr_3$ has the best radiation hardness when subjected to a 1 MeV neutron flux. Furthermore, $CsPbBr_3$ has the smallest average PKA energy, which means $CsPbBr_3$ will have less SKA that cause displacements. In this research, only the PKA energy spectrum is simulated and the DPA calculated using the PKA. However, PKA will sometimes create SKA that in turn can cause atomic displacements too. The material with the lowest average PKA energy, $CsPbBr_3$, would suggest that it has the lowest SKA. However, follow-up molecular dynamics research would be required to scrutinise this hypothesis.

The DPA of the diamond is lower than that of SiC and Ga_2O_3, despite the average PKA energy of diamond being higher than that of SiC and Ga_2O_3. This demonstrates that PKA in diamond will create less atomic displacements than SiC and Ga_2O_3, but diamond may create more SKA than SiC and Ga_2O_3.

5.3 Gamma-ray rejection capability

For intrinsic detection efficiency of γ rays with energies ranging from 0.5 MeV to 1.5 MeV, at the same thickness, the materials ranked from weakest to strongest as follows: $CsPbBr_3$, SiC, diamond, Ga_2O_3, and GaN.

$CsPbBr_3$ demonstrates a lower γ-ray detection efficiency when exposed to γ rays. Although previous reports have highlighted the high photoelectric conversion efficiency of $CsPbBr_3$, which may suggest superior γ-ray detection efficiency, this study finds a relatively low γ-ray detection efficiency for $CsPbBr_3$, for γ-ray energies from 0.5 MeV to 1.5 MeV. This phenomenon can be attributed to the larger molecular mass of $CsPbBr_3$, resulting in the primary reaction between atoms and photons being Compton scattering. Furthermore, due to the thin film of $CsPbBr_3$, Compton scattered electrons can easily escape from the film, leaving only a small amount of energy. Together with $CsPbBr_3$'s good resistance to neutron radiation, $CsPbBr_3$ is a strong candidate for neutron detection materials.

When using a B_4C instead of LiF converter layer, the γ-ray intrinsic detection efficiency of SiC is lower. This suggests that when using a B_4C converter layer, SiC neutron detectors possess better γ-ray resistance. At a low photon energy, the intrinsic γ-ray detection efficiency of SiC does not increase significantly with increasing thickness. However, at a high photon energy, especially for 1.5 MeV, the intrinsic γ-ray detection efficiency of SiC increases rapidly relative to lower energy

γ rays for thicknesses exceeding 11 μm. This suggests that SiC is less sensitive to lower energy γ rays. However, regardless of other factors, SiC possesses the greatest maximum allowable semiconductor thickness, indicating its superior γ-ray rejection capability among the five materials.

Diamond exhibits a similar γ-ray rejection capability as $CsPbBr_3$. Nevertheless, when employing LiF as the converter layer, the intrinsic γ-ray detection efficiency of diamond for 1.5 MeV γ rays reaches around 0.75×10^{-6}, which constitutes a 114% increase compared to the efficiency observed with the B_4C converter layer. This shows that the diamond neutron detector using B_4C as the converter layer has better γ-ray rejection capability than diamond using LiF. Furthermore, for different photon energies, diamond exhibits better γ-ray rejection capability for lower energy γ rays. However, as the energy of γ ray increases, the γ-ray rejection capability of diamond decays the fastest among the five materials, as reflected in the rapid increase in its maximum allowable thickness.

For Ga_2O_3, the intrinsic γ-ray detection efficiency and growth rate do not change significantly with increasing thickness for both converter layer materials. This suggests that the converter layer material has little effect on the maximum allowable thickness of Ga_2O_3. Similarly, the γ-ray intrinsic detection efficiency of Ga_2O_3 remains relatively unchanged under different γ-ray energies, indicating that the γ-ray energy has a limited effect on the γ-ray rejection capability of Ga_2O_3.

In general, the γ-ray rejection capability of Ga_2O_3 is minimally affected by the converter layer material and γ-ray energy.

The very close maximum allowable thicknesses of GaN and Ga_2O_3 suggest that their γ-ray rejection capabilities are quite similar. From this, it can be inferred that for these two materials, the primary interactions with γ rays occur with the Ga element. The maximum allowable thickness of GaN is also insensitive to changes in the converter layer material and to variations in γ-ray energies. It possess a relatively lower maximum allowable thickness. The presence of Ga element weakens the γ-ray resistance of the material. The growth rate of the intrinsic γ-ray detection efficiency of GaN as thickness increases is affected by the γ-ray energy. Higher energy γ rays increase the intrinsic γ-ray detection efficiency of GaN at lower thicknesses (<10 μm). However, when the GaN thickness exceeds 10 μm, its intrinsic detection efficiency for lower energy γ rays is greater than that for higher energy γ rays. This is because at low thicknesses, low energy γ rays can easily escape GaN, while the higher energy γ rays increase the number of electron pair effects, improving γ-ray detection efficiency in addition to Compton scattering. Once the GaN thickness is increased to a certain thickness, the low energy γ rays can deposit more energy in GaN, resulting in increased intrinsic detection efficiency. In summary, the GaN neutron detector with a B_4C converter layer has better γ-ray rejection capability than with LiF. Furthermore, with the

B_4C converter layer, the optimal thickness of GaN semiconductor layer is less than 3 μm, providing stronger rejection capability for lower energy γ rays.

Chapter 6

Conclusions

This chapter provides a review of all of the findings, achievements and techniques developed and detailed in this thesis. In summary, this thesis has:

1. A software suite is developed by using Python, based on theoretical methods, to calculate the optimal thicknesses of B_4C and LiF converter layers for specific energy levels. This software was utilised to ascertain the optimal thicknesses of these two types of converter materials when the energy range is between 100 keV, 200 keV, and 300 keV up to 900 keV. The theoretical method was used for comparison with Monte Carlo (MC) simulation results, demonstrating consistent trends.

2. Developed an automatic search program for the best thickness of semiconductor neutron detection based on Geant4 and custom Linux scripts. The program was used to demonstrate the optimisation of neutron detection thick-

ness for five non-directly detecting semiconductors: diamond, SiC, Ga_2O_3, GaN, and $CsPbBr_3$. The study discusses the performance of semiconductor neutron detectors under different converter layer materials and different LLD conditions. It brings great guidance for wideband gap semiconductor neutron detector fabrication and utilisation.

3. Conducted research that filled a gap in the study of Threshold Displacement Energy (TDE) for $CsPbBr_3$. Through an automated TDE finding program developed in this thesis, the average TDE energies of three types of atoms in $CsPbBr_3$ at 100 K, 200 K, 300 K, and 400 K were obtained. This provides data for the calculation of Displacement Per Atom (DPA) for $CsPbBr_3$.

4. Studied the radiation resistance of five non-directly detecting semiconductors: diamond, SiC, Ga_2O_3, GaN, and $CsPbBr_3$. The radiation resistance of the materials was primarily evaluated through the study of cascaded collision PKA spectra and DPA. At the microscopic level, based on a comparison of DPA values, the study predicts that $CsPbBr_3$ will exhibit the strongest resistance to displacement damage when subjected to neutron radiation of the material studied.

5. Used Monte Carlo simulation to simulate the γ-ray rejection capability of diamond, SiC, Ga_2O_3, GaN and $CsPbBr_3$, for the γ-ray energy range from 0.5 MeV to 1.5 MeV. Overall, when the thickness of each material is at

the optimised neutron detection thickness, all simulated materials demonstrated good γ-ray rejection capability. Additionally, the maximum growth thicknesses achievable by the five materials at specific γ-ray energies were determined to achieve a favourable γ rejection ratio.

Chapter 7

Recommendations

In this final chapter, the recommendations for further work are addressed. The primary focus of future work will include refining the theory for calculating the thickness of LiF converter layer, developing a simulation model for the charge detection efficiency (CDE) of GaN, further enhancing the automation of the programme, and strengthening the research on direct detection semiconductors.

1. Further research on the theory for calculating the thickness of LiF converter layer

    - When thermal neutrons react with LiF, there may be a new distribution of the energies of the secondary charged particles. Although the proportion of this new energy distribution is low, it could still be a reason for the discrepancies observed between the theoretical curves and MC simulations at high LLD. Therefore, future research will concentrate on this aspect, with improvements to the theoretical calculation formulas being undertaken to eliminate the differences between them.

2. Simulation and measurement of the actual charge detection efficiency of GaN

    - In the realm of GaN research, a significant shortcoming exists in terms of detailed CDE measurements. The low carrier lifetime of GaN, which can be less than 1 μs, renders the measurement of its carrier mobility, mobility rate and CDE challenging. Conversely, an all-encompassing simulation method for CDE has yet to emerge. Present-day simulations concentrate on pure charge collection efficiency, typically utilising finite element methods. However, most of these wide-band semiconductor materials are artificially constructed thin-film materials. Due to the limitations of the manufacturing process and technology, defects exist within both polycrystalline and single-crystalline thin films. Given the imprecise knowledge of internal defects and their distribution, an accurate simulation of CDE cannot be performed. In the future, a research avenue may involve the use of finite element methods, molecular dynamics methods and kinetic Monte Carlo methods in tandem to simulate CDE within defective wide band semiconductors.

3. Further research on programme development

- The converter layer thickness calculation software will be further refined, taking into account a wider range of emitted particle energies. Formulas for calculating the range of particles within the converter layer will be directly incorporated, thereby enhancing the user experience.

- This study presents the development of a custom Linux-based script for optimising the neutron detection thickness of semiconductors with converter layers. The current progress of this development is in its initial stage, where the script is only able to support text input of LLD energy and five semiconductor materials, namely diamond, SiC, GaN, Ga_2O_3, and $CsPbBr_3$, for performing optimised thickness simulations under different LLD energies. In the second phase of the programme development, additional materials for thickness optimisation and a graphical user interface with windowing capabilities will be added. The third phase will focus on machine learning, where a large number of Monte Carlo optimisation calculations will be used as a training set. In the final phase, users will be able to define materials, LLD, converter layer thickness, and material density to obtain optimal thicknesses quickly through machine learning.

- In this study, the automatic finding of TDE based on a Python script with LAMMPS molecular dynamics toolkits was developed. The current development is in its infancy and cannot support text input for custom materials. In the second phase of development, the focus will be on creating programme input interfaces, adding features such as defining materials and potential energy.

4. Research on direct detection materials BN and BAs

    - Future studies will be carried out on direct detection materials. Simulation studies on the properties of BN and BAs, including charge detection efficiency, radiation resistance, and TDE, will be conducted. The growth and synthesis methods of both materials will be further explored. In terms of experiments, neutron detection experiments will be conducted on BN detectors. Experimental spectra will be obtained for comparison with simulated spectra, and methods to improve detection efficiency will be sought, including but not limited to, the use of microstructure detectors and other approaches.

Glossary

Al Aluminium

AlN Aluminum nitride

As Arsenic

B Boron

BAs Boron arsenide

B_4C Boron carbide

BF_3 Boron trifluoride

BN Boron nitride

BNCT Boron Neutron Capture Therapy

c-BAs Cubic boron arsenide

c-BN Cubic boron nitride

CCE Charge Collection Efficiency

CDE Charge Detection Efficiency

CERN Conseil Européen pour la Recherche Nucléaire (French for European Council for Nuclear Research)

Co Cobalt

Cs Caesium

$CsPbBr_3$ Caesium lead bromide

CVD Chemical Vapour Deposition

D Deuterium

DFT Density Functional Theory

DPA Displacement Per Atom

DVNS Diamond Vertical Neutron Spectrometer

EGS Electron Gamma Shower

GaAs Gallium Arsenide

GaN Gallium nitride

Ga_2O_3 Gallium oxide

Geant4 is a toolkit for the simulation of the passage of particles through matter. Its areas of application include high energy, nuclear and accelerator physics, as well as studies in medical and space science

GM Geiger-Müller. A Geiger-Müller tube is the sensing element of a Geiger counter instrument that can detect a single particle of ionizing radiation, and typically produce an audible click for each. It was named for Hans Geiger who invented the device in 1908, and Walther Müller who collaborated with Geiger in developing it further in 1928. It is a type of gaseous ionisation detector with an operating voltage in the Geiger plateau

GYAGG Gadolinium-yttrium-aluminum-gallium garnets

h-BN Hexagonal boron nitride

HDPE High-density polyethylene

^{3}He Helium-3

HEC High End Computer

JET Joint European Tours

LAMMPS Large-scale Atomic/Molecular Massively Parallel Simulator

Li Lithium

LiF Lithium fluoride

LJ The Lennard-Jones potential describes electronically neutral atoms or molecules

LLD Low-Level Discriminator

LPCVD Low Pressure Chemical Vapor Deposition

MBE Molecular Beam Epitaxy

MC Monte Carlo methods, or Monte Carlo experiments, are a broad class of computational algorithms that rely on repeated random sampling to obtain numerical results

MCNP Monte Carlo N-Particle. 'N' indicates that the code can simulate the behaviour of multiple types of particles

MD Molecular Dynamics

MOCVD Metal-Organic Chemical Vapor Deposition

MPI Message Passing Interface

MSM Metal-Semiconductor-Metal

N Nitrogen

NPT In molecular dynamics simulations, such as those performed in LAMMPS, the Isothermal-Isobaric ensemble is often referred to as the NPT ensemble. The abbreviation NPT stands for: N: Number of particles (constant) P: Pressure (constant) T: Temperature (constant) These three properties are maintained at constant values in an Isothermal-Isobaric ensemble, hence the abbreviation NPT

NVE In the context of molecular dynamics simulations, such as those performed in LAMMPS, the Microcanonical ensemble is often referred to as the NVE ensemble. The abbreviation NVE stands for: N: Number of particles (constant) V: Volume (constant) E: Energy (constant) These three properties are conserved in a Microcanonical ensemble, hence the abbreviation NVE

PBN Pyrolytic boron nitride

PKA Primary Knock-out Atom

PMT Photomultiplier Tube

PWR pressurized water reactor

SDD Single-crystal Diamond Detector

Si Silicon

SiC Silicon carbide

SRIM The Stopping and Range of Ions in Matter

SSB Silicon Surface Barrire

T Tritium

TDE Threshold Displacement Energy

TEM Transmission Electron Microscopy

TOF Time-Of-Flight

^{235}**U** Uranium-235

WBG Wide-bandgap

WS Wigner-Seitz

XRD X-ray Diffraction

ZnS(Ag) Zinc sulfide with silver activator

Bibliography

[AAA$^+$03] S. Agostinelli, J. Allison, K. Amako, J. Apostolakis, H. Araujo, P. Arce, M. Asai, D. Axen, S. Banerjee, G. Barrand, et al. Geant4-a simulation toolkit. *Nuclear Instruments and Methods in Physics Research Section A: Accelerators, Spectrometers, Detectors and Associated Equipment*, 506(3):250–303, 2003.

[AAA$^+$16] J. Allison, K. Amako, J. Apostolakis, P. Arce, M. Asai, T. Aso, E. Bagli, A. Bagulya, S. Banerjee, G. Barrand, et al. Recent developments in Geant4. *Nuclear Instruments and Methods in Physics Research Section A: Accelerators, Spectrometers, Detectors and Associated Equipment*, 835:186–225, 2016.

[AIM$^+$14] K. Atsumi, Y. Inoue, H. Mimura, T. Aoki, and T. Nakano. Neutron detection using boron gallium nitride semiconductor material. *APL Materials*, 2(3):032106, 2014.

[AKJ15] J. Azamat, A. Khataee, and S. W. Joo. Molecular dynamics simulation of trihalomethanes separation from water by functionalized nanoporous graphene under induced pressure. *Chemical Engineering Science*, 127:285–292, 2015.

[And80] H. C. Andersen. Molecular dynamics simulations at constant pressure and/or temperature. *The Journal of Chemical Physics*, 72(4):2384–2393, 1980.

[ASM$^+$10] V. Avrutin, D. J. Silversmith, Y. Mori, F. Kawamura, Y. Kitaoka, and H. Morkoc. Growth of bulk GaN and AlN: Progress and challenges. *Proceedings of the IEEE*, 98(7):1302–1315, 2010.

[AW57] B. J. Alder and T. E. Wainwright. Phase transition for a hard sphere system. *The Journal of chemical physics*, 27(5):1208–1209, 1957.

[BBC$^+$95] C. Bauer, I. Baumann, C. Colledani, J. Conway, P. Delpierre, F. Djama, W. Dulinski, A. Fallou, K. K. Gan, R.S. Gilmore, et al. Radiation hardness studies of CVD diamond detectors. *Nuclear Instruments and Methods in Physics Research Section A: Accelerators, Spectrometers, Detectors and Associated Equipment*, 367(1-3):207–211, 1995.

[Bet30] H. Bethe. Zur theorie des durchgangs schneller korpuskularstrahlen durch materie. *Annalen der Physik*, 397(3):325–400, 1930.

[BLF$^+$20] C. G. Bischak, M. Lai, Z. Fan, D. Lu, P. David, D. Dong, H. Chen, A. S. Etman, T. Lei, J. Sun, et al. Liquid-like interfaces mediate structural phase transitions in lead halide perovskites. *Matter*, 3(2):534–545, 2020.

[BLT$^+$22] D. A. Buchnyy, V. S. Litvin, D. N. Trunov, V. N. Marin, S. N. Axenov, and R. A. Sadykov. Simulation of the neutron-detection efficiency and resolution of a scintillation counter based on zns (ag): 6lif. *Journal of Surface Investigation: X-ray, Synchrotron and Neutron Techniques*, 16(6):1121–1129, 2022.

[BPVG$^+$84] H. J. C. Berendsen, J. P. M. Postma, W. F. Van Gunsteren, A. DiNola, and J. R. Haak. Molecular dynamics with coupling to an external bath. *The Journal of chemical physics*, 81(8):3684–3690, 1984.

[BTM$^+$01] P. Bergonzo, D. Tromson, C. Mer, B. Guizard, F. Foulon, and A. Brambilla. Particle and radiation detectors based on diamond. *physica status solidi (a)*, 185(1):167–181, 2001.

[BY20] J. Blevins and G. Yang. Enabling Ga_2O_3's neutron detection capability with boron doping and conversion layer. *Journal of Applied Physics*, 128(15):155706, 2020.

[CP91] T. Cagin and B. M. Pettitt. Grand molecular dynamics: A method for open systems. *Molecular Simulation*, 6(1-3):5–26, 1991.

[DAG$^+$22] M. Duer, T. Aumann, R. Gernhäuser, V. Panin, S. Paschalis, D. M. Rossi, N. L. Achouri, D. Ahn, H. Baba, C. A. Bertulani, et al. Observation of a correlated free four-neutron system. *Nature*, 606(7915):678–682, 2022.

[DPR$^+$03] A. Dadgar, M. Poschenrieder, A. Reiher, J. Bläsing, J. Christen, A. Krtschil, T. Finger, T. Hempel, A. Diez, and A. Krost. Reduction of stress at the initial stages of GaN growth on Si (111). *Applied physics letters*, 82(1):28–30, 2003.

[DRHC11] V. Domnich, S. Reynaud, R. A. Haber, and M. Chhowalla. Boron carbide: structure, properties, and stability under stress. *Journal of the American Ceramic Society*, 94(11):3605–3628, 2011.

[EBKAA$^+$21] L. El Bouanani, S. E. Keating, C. Avila-Avendano, M. G. Reyes-Banda, M. I. Pintor-Monroy, V. Singh, B. L. Murillo, M. Higgins, and M. A. Quevedo-Lopez. Solid-state neutron detection based on methylammonium lead bromide perovskite single crystals. *ACS Applied Materials & Interfaces*, 13(24):28049–28056, 2021.

[EH85] D. J. Evans and B. L. Holian. The nose–hoover thermostat. *The Journal of chemical physics*, 83(8):4069–4074, 1985.

[Eva83] D. J. Evans. Computer “experiment” for nonlinear thermodynamics of couette flow. *The Journal of Chemical Physics*, 78(6):3297–3302, 1983.

[FCB+19] E. Farzana, M. F. Chaiken, T. E. Blue, A. R. Arehart, and S. A. Ringel. Impact of deep level defects induced by high energy neutron radiation in β-Ga_2O_3. *APL Materials*, 7(2):022502, 2019.

[FIRBM+20] L. Fernandez-Izquierdo, M. G. Reyes-Banda, X. Mathew, I. R. Chavez-Urbiola, L. El Bouanani, J. Chang, C. Avila-Avendano, N. R. Mathews, M. I. Pintor-Monroy, and M. Quevedo-Lopez. Cesium lead bromide ($CsPbBr_3$) thin-film-based solid-state neutron detector developed by a solution-free sublimation process. *Advanced Materials Technologies*, 5(12):2000534, 2020.

[FKA+22] A. Fedorov, I. Komendo, A. Amelina, E. Gordienko, V. Gurinovich, V. Guzov, G. Dosovitskiy, V. Kozhemyakin, D. Kozlov, A. Lopatik, et al. Gyagg/6lif composite scintillation screen for neutron detection. *Nuclear Engineering and Technology*, 54(3):1024–1029, 2022.

[FR16] R. B. Firestone and Z. S. Revay. Thermal neutron radiative cross sections for li6, 7, be9, b10, 11, c12,13, and n14, 15. *Physical Review C*, 93(5):054306, 2016.

[Gel60] S. Geller. Crystal structure of β-Ga_2O_3. *The Journal of Chemical Physics*, 33(3):676–684, 1960.

[GFCW+21] F. M. Gonzalez, E. M. Fries, C. Cude-Woods, T. Bailey, M. Blatnik, L. J. Broussard, N. B. Callahan, J. H. Choi, S. M. Clayton, S. A. Currie, et al. Improved neutron lifetime measurement with ucn τ. *Physical review letters*, 127(16):162501, 2021.

[GGMW19] X. Guan, Y. Gong, I. Murata, and T. Wang. The new design and validation of an epithermal neutron flux detector using ^{71}Ga (n, γ) ^{72}Ga reaction for bnct. *Journal of Instrumentation*, 14(06):P06016, 2019.

[GMK+20] H. Gao, S. Muralidharan, M. R. Karim, S. M. White, L. Cao, K. Leedy, H. Zhao, D. C. Look, and L.J. Brillson. Neutron irradiation and forming gas anneal impact on β-Ga_2O_3 deep level defects. *Journal of Physics D: Applied Physics*, 53(46):465102, 2020.

[GMMW15] X. Guan, M. Manabe, I. Murata, and T. Wang. Design of an epithermal neutron flux intensity monitor with gan wafer for boron neutron capture therapy. *Journal of Nuclear Science and Technology*, 52(4):503–508, 2015.

[GVK+22] B. S. Gajjar, S. K. Varshney, S. Kumar, M. Jindal, P. Vaghasiya, S. George, Z. Khan, and H. K. B. Pandya. Boron carbide as high-energy radiation shielding material for iter. *IEEE Transactions on Plasma Science*, 50(12):5078–5084, 2022.

[HBK+20] J. Holmes, J. Brown, F. A. Koeck, H. Johnson, M. K. Benipal, P. Kandlakunta, A. Zaniewski, R. Alarcon, R. Cao, S. M. Goodnick, et al. Performance of 5-μm pin diamond diodes as thermal neutron detectors. *Nuclear Instruments and Methods in Physics Research*

Section A: Accelerators, Spectrometers, Detectors and Associated Equipment, 961:163601, 2020.

[HLM82] W. G. Hoover, A. J. C. Ladd, and B. Moran. High-strain-rate plastic flow studied via nonequilibrium molecular dynamics. *Physical Review Letters*, 48(26):1818, 1982.

[HSVM20] P. Hazdra, P. Smrkovský, J. Vobecký, and A. Mihaila. Radiation resistance of high-voltage silicon and 4H-SiC power pin diodes. *IEEE Transactions on Electron Devices*, 68(1):202–207, 2020.

[Jon24] J. E. Jones. On the determination of molecular fields.-I. from the variation of the viscosity of a gas with temperature. *Proceedings of the Royal Society of London. Series A, Containing Papers of a Mathematical and Physical Character*, 106(738):441–462, 1924.

[KAY$^+$20] M. I. Kobayashi, M. Angelone, S. Yoshihashi, K. Ogawa, M. Isobe, T. Nishitani, S. Sangaroon, S. Kamio, Y. Fujiwara, T. Tsubouchi, et al. Thermal neutron measurement by single crystal CVD diamond detector applied with the pulse shape discrimination during deuterium plasma experiment in LHD. *Fusion Engineering and Design*, 161:112063, 2020.

[KPF$^+$19] J. Kim, S. J. Pearton, C. Fares, J. Yang, F. Ren, S. Kim, and A. Y. Polyakov. Radiation damage effects in Ga_2O_3 materials and devices. *Journal of Materials Chemistry C*, 7(1):10–24, 2019.

[KTS$^+$20] P. Kandlakunta, C. Tan, N. Smith, S. Xue, N. Taylor, R. G. Downing, V. Hlinka, and L. R. Cao. Silicon carbide detectors for high flux neutron monitoring at near-core locations. *Nuclear Instruments and Methods in Physics Research Section A: Accelerators, Spectrometers, Detectors and Associated Equipment*, 953:163110, 2020.

[Law57] J. D. Lawson. Some criteria for a power producing thermonuclear reactor. *Proceedings of the physical society. Section B*, 70(1):6, 1957.

[LCZ$^+$19] J. Liu, J. Chang, G. Zhong, J. Zhang, X. Pang, and J. Jia. Fabrication and performance of single crystal diamond neutron and gamma ray detectors. *AIP Advances*, 9(9):095103, 2019.

[LLR20] J. Lehtomäki, J. Li, and P. Rinke. Boron doping in gallium oxide from first principles. *Journal of Physics Communications*, 4(12):125001, 2020.

[LZYO19] Y. Liu, T. Zhu, J. Yao, and X. Ouyang. Simulation of radiation damage for silicon drift detector. *Sensors*, 19(8):1767, 2019.

[MAC$^+$22] A. Massara, S. Amaducci, L. Cosentino, F. Longhitano, C. Marchetta, G. E. Poma, M. Ursino, and P. Finocchiaro. 6lif converters for neutron detection: Production procedures and detector tests. *Instruments*, 7(1):1, 2022.

[MGN+16] A. Muraro, L. Giacomelli, M. Nocente, M. Rebai, D. Rigamonti, F. Belli, P. Calvani, J. Figueiredo, M. Girolami, G. Gorini, et al. First neutron spectroscopy measurements with a pixelated diamond detector at jet. *Review of Scientific Instruments*, 87(11):11D833, 2016.

[MHY+03] D. S. McGregor, M. D. Hammig, Y. H. Yang, H. K. Gersch, and R. T. Klann. Design considerations for thin film coated semiconductor thermal neutron detectors - I: Basics regarding alpha particle emitting neutron reactive films. *Nuclear Instruments and Methods in Physics Research, Section A: Accelerators, Spectrometers, Detectors and Associated Equipment*, 500(1-3):272–308, 2003.

[MKM+12] J. W. Murphy, G. R. Kunnen, I. Mejia, M. A. Quevedo-Lopez, D. Allee, and B. Gnade. Optimizing diode thickness for thin-film solid state thermal neutron detectors. *Applied Physics Letters*, 101(14):143506, 2012.

[MLBO96] D. S. McGregor, J. T. Lindsay, C. C. Brannon, and R. W. Olsen. Semi-insulating bulk gaas thermal neutron imaging arrays. *IEEE Transactions on Nuclear Science*, 43(3):1357–1364, 1996.

[MMP+06] M. Marinelli, E. Milani, G. Prestopino, M. Scoccia, A. Tucciarone, G. Verona-Rinati, M. Angelone, M. Pillon, and D. Lattanzi. High performance ^{6}LiF-diamond thermal neutron detectors. *Applied Physics Letters*, 89(14):143509, 2006.

[MNT16] P. J. Mohr, D. B. Newell, and B. N. Taylor. Codata recommended values of the fundamental physical constants: 2014. *Journal of Physical and Chemical Reference Data*, 45(4):043102, 2016.

[MPA+19] S. D. Monk, S. P. Platt, M. J. Anderson, D. Cheneler, and M. Alhamdi. Development of an optimized converter layer for a silicon-carbide-based neutron sensor for the detection of fissionable materials. In *2019 IEEE Nuclear Science Symposium and Medical Imaging Conference (NSS/MIC)*, pages 1–7. IEEE, 2019.

[MSP+05] F. Moscatelli, A. Scorzoni, A. Poggi, M. Bruzzi, S. Lagomarsino, S. Mersi, S. Sciortino, and R. Nipoti. Measurements and simulations of charge collection efficiency of p+/n junction sic detectors. *Nuclear Instruments and Methods in Physics Research Section A: Accelerators, Spectrometers, Detectors and Associated Equipment*, 546(1-2):218–221, 2005.

[NZS+18] K. Nordlund, S. J. Zinkle, A. E. Sand, F. Granberg, R. S. Averback, R. Stoller, T. Suzudo, L. Malerba, F. Banhart, W. J. Weber, et al. Improving atomic displacement and replacement calculations with physically realistic damage models. *Nature communications*, 9(1):1084, 2018.

[OOK+18] O. Obraztsova, L. Ottaviani, A. Klix, T. Döring, O. Palais, and A. Lyoussi. Comparison between Silicon-Carbide and diamond for fast neutron detection at room temperature. *EPJ Web of Conferences*, 2018.

[PAM+16] R. Pilotti, M. Angelone, M. Marinelli, E. Milani, G. Verona-Rinati, C. Verona, G. Prestopino, R. M. Montereali, M. A. Vincenti, E. M. Schooneveld, et al. High-temperature long-lasting stability assessment of a single-crystal diamond detector under high-flux neutron irradiation. *Europhysics Letters*, 116(4):42001, 2016.

[PAP+16] R. Pilotti, M. Angelone, G. Pagano, S. Loreti, M. Pillon, F. Sarto, M. Marinelli, E. Milani, G. Prestopino, C. Verona, et al. Development and high temperature testing by 14 MeV neutron irradiation of single crystal diamond detectors. *Journal of Instrumentation*, 11(06):C06008, 2016.

[PFW+07] D. S. Peng, Y. C. Feng, W. X. Wang, X. F. Liu, W. Shi, and H. B. Niu. High-quality GaN films grown on surface treated sapphire substrate. *Journal of Physics D: Applied Physics*, 40(4):1108, 2007.

[Pli95] S. Plimpton. Fast parallel algorithms for short-range molecular dynamics. *Journal of Computational Physics*, 117(1):1–19, 1995.

[PLY16] M. Peng, C. Lan, and T. Ye. The computing and simulation of energy loss performance for deuteron in different target. *Applied Physics*, 6(8):159–166, 2016.

[Pro20] The Materials Project. Materials data on $CsPbBr_3$ by materials project. *LBNL Materials Project*, 7 2020.

[RFS+00] V. Ramachandran, R. M. Feenstra, W. L. Sarney, L. Salamanca-Riba, and D. W. Greve. Optimized structural properties of wurtzite GaN on SiC(0001) grown by molecular beam epitaxy. *Journal of Vacuum Science & Technology A: Vacuum, Surfaces, and Films*, 18(4):1915–1918, 2000.

[SBB60] H. W. Schmitt, R. C. Block, and R. L. Bailey. Total neutron cross section of b10 in the thermal neutron energy range. *Nuclear Physics*, 17:109–115, 1960.

[SDR+99] S. Seshadri, A. R. Dulloo, F. H. Ruddy, J. G. Seidel, and L. B. Rowland. Demonstration of an SiC neutron detector for high-radiation environments. *IEEE Transactions on Electron Devices*, 46(3):567–571, 1999.

[SGF+23] Y. Shi, Z. Guo, Q. Fu, X. Shen, Z. Zhang, W. Sun, J. Wang, J. Sun, Z. Zhang, T. Liu, et al. Localized nuclear reaction breaks boron drug capsules loaded with immune adjuvants for cancer immunotherapy. *Nature Communications*, 14(1):1884, 2023.

[SHZ⁺21] K. Su, Q. He, J. Zhang, Z. Ren, L. Liu, J. Zhang, X. Ouyang, and Y. Hao. Device performance of chemical vapor deposition monocrystal diamond radiation detectors correlated with the bulk diamond properties. *Journal of Physics D: Applied Physics*, 54(14):145105, 2021.

[SKRK20] S. Sankaranarayanan, P. Kandasamy, R. Raju, and B. Krishnan. Fabrication of gallium nitride and nitrogen doped single layer graphene hybrid heterostructures for high performance photodetectors. *Scientific Reports*, 10(1):14507, 2020.

[SPD23] R. M. Sahani, A. Pandya, and A. Dixit. Zno-6lif/polystyrene composite scintillator for thermal neutron radiation detection. *Review of Scientific Instruments*, 94(2), 2023.

[SPP⁺20] T. Slavicek, S. Petersson, S. Pospisil, G. Thungstrom, and M. Slavickova. SiC based charged particle strip sensor spectrometer with neutron detection capability. *Journal of Instrumentation*, 15(01):C01036, 2020.

[SR74] F. H. Stillinger and A. Rahman. Improved simulation of liquid water by molecular dynamics. *The Journal of Chemical Physics*, 60(4):1545–1557, 1974.

[SRX⁺19] Y. T. Shi, F. F. Ren, W. Z. Xu, X. Chen, J. Ye, L. Li, D. Zhou, R. Zhang, Y. Zheng, H. H. Tan, et al. Realization of p-type gallium nitride by magnesium ion implantation for vertical power devices. *Scientific Reports*, 9(1):8796, 2019.

[Stu09] A. Stukowski. Visualization and analysis of atomistic simulation data with OVITO–the Open Visualization Tool. *Modelling and simulation in materials science and engineering*, 18(1):015012, 2009.

[SVSN20] L. Soriano, H. Valencia, K. X. Sun, and R. Nelson. Fast neutron irradiation effects on multiple gallium nitride (GaN) device reliability in presence of ambient variations. In *2020 IEEE International Reliability Physics Symposium (IRPS)*, pages 1–6. IEEE, 2020.

[TAB⁺22] A. P. Thompson, H. M. Aktulga, R. Berger, D. S. Bolintineanu, W. M. Brown, P. S. Crozier, P. J. in't Veld, A. Kohlmeyer, S. G. Moore, T. D. Nguyen, et al. LAMMPS-a flexible simulation tool for particle-based materials modeling at the atomic, meso, and continuum scales. *Computer Physics Communications*, 271:108171, 2022.

[VSM⁺20] I. P. Vali, P. K. Shetty, M. G. Mahesha, M. N. Rao, and S. Kesari. Thermal neutron irradiation effects on structural and electrical properties of n-type 4H-SiC. *Journal of Materials Science: Materials in Electronics*, 31:8496–8501, 2020.

[VVRP⁺18] C. Verona, G. Verona-Rinati, S. Platt, E. M. Schooneveld, and A. Pietropaolo. Comparison between silicon and single-crystal diamond photodiodes for localized pulsed fast neutron detection. *Europhysics Letters*, 121(6):68002, 2018.

[WMBC15] J. Wang, P. Mulligan, L. Brillson, and L. R. Cao. Review of using gallium nitride for ionizing radiation detection. *Applied Physics Reviews*, 2(3):031102, 2015.

[WS33] E. Wigner and F. Seitz. On the constitution of metallic sodium. *Physical Review*, 43(10):804, 1933.

[XMW+17] Q. Xu, P. Mulligan, J. Wang, W. Chuirazzi, and L. Cao. Bulk GaN alpha-particle detector with large depletion region and improved energy resolution. *Nuclear Instruments and Methods in Physics Research Section A: Accelerators, Spectrometers, Detectors and Associated Equipment*, 849:11–15, 2017.

[ZA20] Z. Zhang and M. D. Aspinall. Optimizing converter layer and active volume thickness for gallium nitride neutron detectors. In *2020 IEEE Nuclear Science Symposium and Medical Imaging Conference (NSS/MIC)*, pages 1–6. IEEE, 2020.

[ZA21a] Z. Zhang and M. D. Aspinall. Comparison of neutron detection performance of four thin-film semiconductor neutron detectors based on Geant4. *Sensors*, 21(23):7930, 2021.

[ZA21b] Z. Zhang and M. D. Aspinall. Simulation of the effect of neutron radiation on the caesium lead bromide. In *2021 IEEE Nuclear Science Symposium and Medical Imaging Conference (NSS/MIC)*, pages 1–2. IEEE, 2021.

[ZA22] Z. Zhang and M. D. Aspinall. Simulations of charge collection of a gallium nitride based pin thin-film neutron detector. *Journal of Instrumentation*, 17(08):C08013, 2022.

[ZSZ+20] Z. Zhu, Z. Sun, J. Zou, B. Tang, Q. Xiu, R. Wang, J. Qu, W. Deng, S. Wang, J. Peng, et al. Fabrication and performance evaluation of GaN thermal neutron detectors with ^{6}LiF conversion layer. *Chinese Physics B*, 29(9):090401, 2020.

[ZZB10] J. F. Ziegler, M. D. Ziegler, and J. P. Biersack. SRIM–The stopping and range of ions in matter (2010). *Nuclear Instruments and Methods in Physics Research Section B: Beam Interactions with Materials and Atoms*, 268(11-12):1818–1823, 2010.

[ZZL+18] Z. Zhu, H. Zhang, H. Liang, B. Tang, X. Peng, J. Liu, C. Yang, X. Xia, P. Tao, R. Shen, et al. High-temperature performance of gallium-nitride-based pin alpha-particle detectors grown on sapphire substrates. *Nuclear Instruments and Methods in Physics Research Section A: Accelerators, Spectrometers, Detectors and Associated Equipment*, 893:39–42, 2018.

[ZZT+18] Z. Zhu, J. Zou, B. Tang, Z. Wang, X. Peng, H. Liang, H. Zhang, and G. Du. Effects of 10 MeV electron irradiation on the characteristics of gallium-nitride-based pin alpha-particle detectors. *Nuclear*

Instruments and Methods in Physics Research Section A: Accelerators, Spectrometers, Detectors and Associated Equipment, 902:9–13, 2018.

Appendix

Table 1: Optimised semiconductor thickness with optimal B_4C converter layer thickness for diamond with LLD range from 100 keV to 900 keV.

LLD (keV)	100	200	300	400	500	600	700	800	900
Thickness (μm)	0.2	0.5	0.7	0.8	0.8	1.0	1.1	1.3	1.4

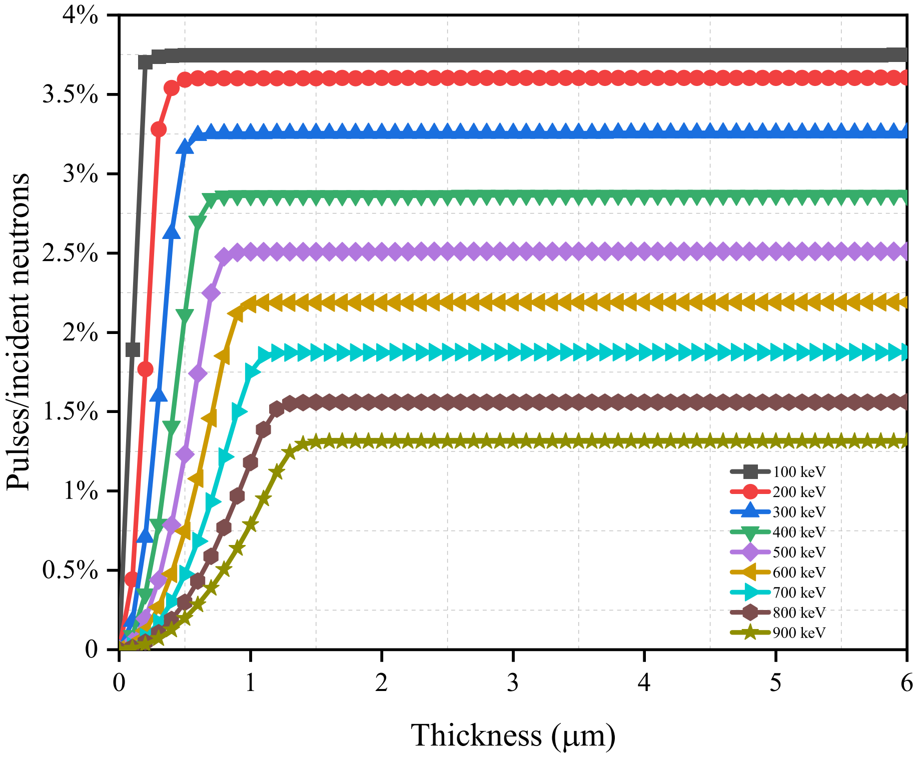

Figure 1: Neutron detection efficiency versus semiconductor material thickness with optimal B_4C converter layer thickness for diamond with LLD range from 100 keV to 900 keV.

Table 2: Optimised semiconductor thickness with optimal B_4C converter layer thickness for SiC with LLD range from 100 keV to 900 keV.

LLD (keV)	100	200	300	400	500	600	700	800	900
Thickness (μm)	0.3	0.7	1.0	1.1	1.1	1.3	1.6	1.8	1.8

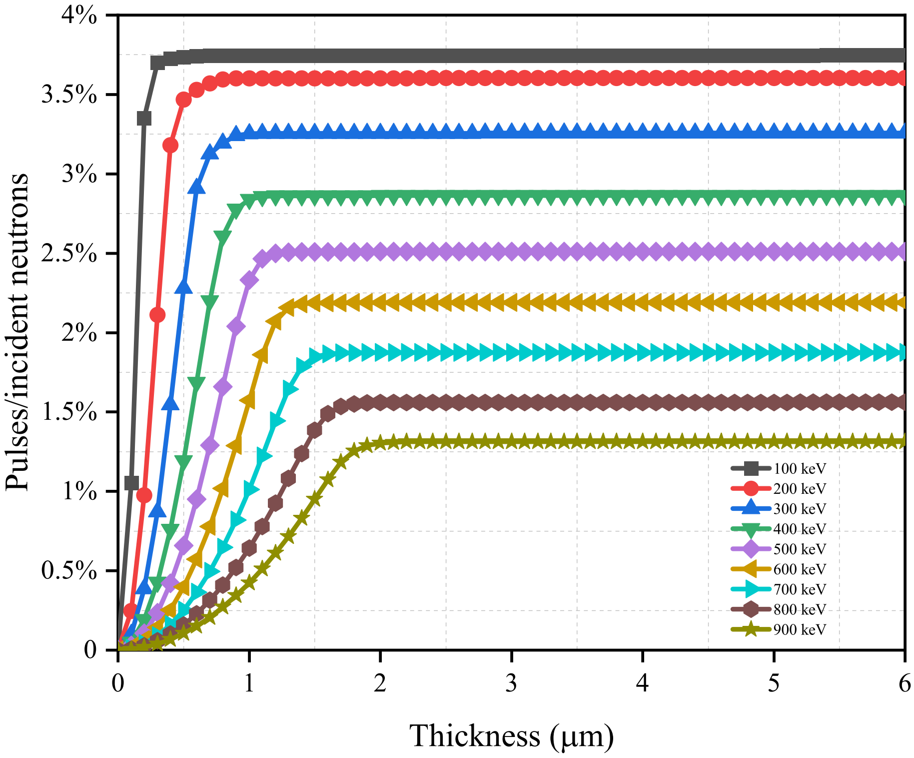

Figure 2: Neutron detection efficiency versus semiconductor material thickness with optimal B_4C converter layer thickness for SiC with LLD range from 100 keV to 900 keV.

Table 3: Optimised semiconductor thickness with optimal B_4C converter layer thickness for Ga_2O_3 with LLD range from 100 keV to 900 keV.

LLD (keV)	100	200	300	400	500	600	700	800	900
Thickness (μm)	0.3	0.7	1.1	1.2	1.2	1.3	1.5	1.8	1.7

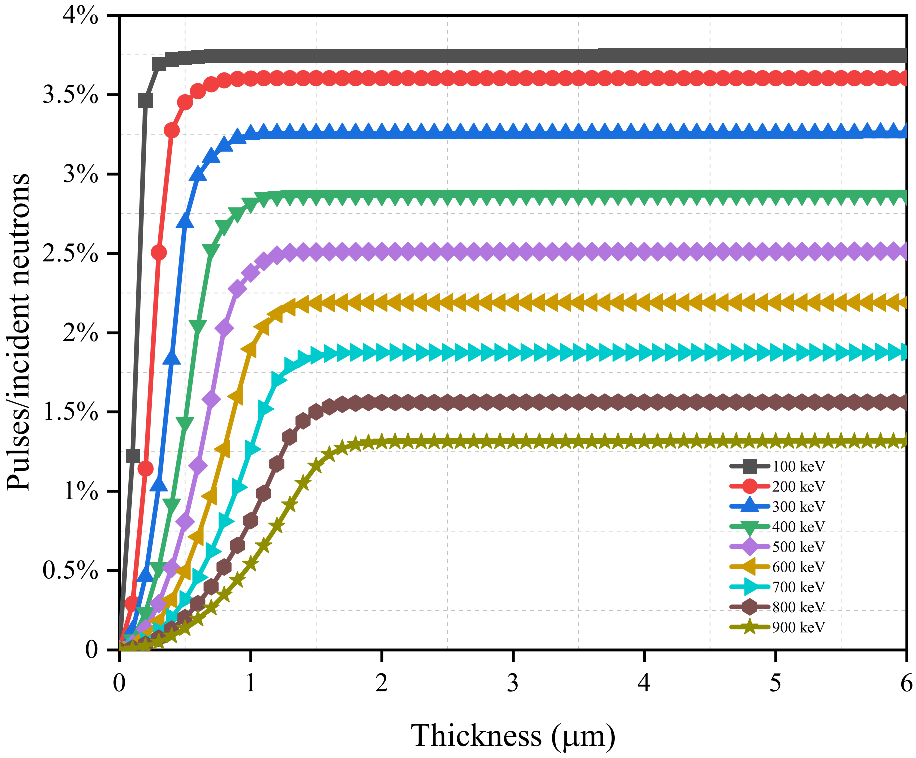

Figure 3: Neutron detection efficiency versus semiconductor material thickness with optimal B_4C converter layer thickness for Ga_2O_3 with LLD range from 100 keV to 900 keV.

Table 4: Optimised semiconductor thickness with optimal B_4C converter layer thickness for GaN with LLD range from 100 keV to 900 keV.

LLD (keV)	100	200	300	400	500	600	700	800	900
Thickness (μm)	0.3	0.8	1.2	1.3	1.3	1.5	1.7	2.0	1.9

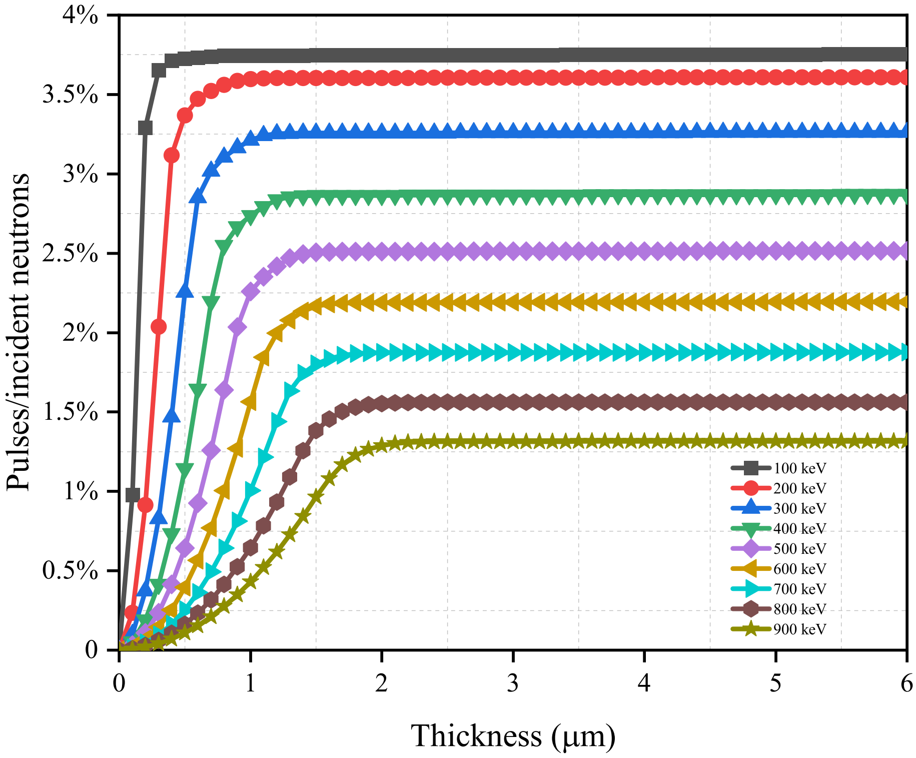

Figure 4: Neutron detection efficiency versus semiconductor material thickness with optimal B_4C converter layer thickness for GaN with LLD range from 100 keV to 900 keV.

Table 5: Optimised semiconductor thickness with optimal B_4C converter layer thickness for $CsPbBr_3$ with LLD range from 100 keV to 900 keV.

LLD (keV)	100	200	300	400	500	600	700	800	900
Thickness (μm)	0.6	1.4	2.3	2.5	2.5	2.9	3.4	4.1	3.9

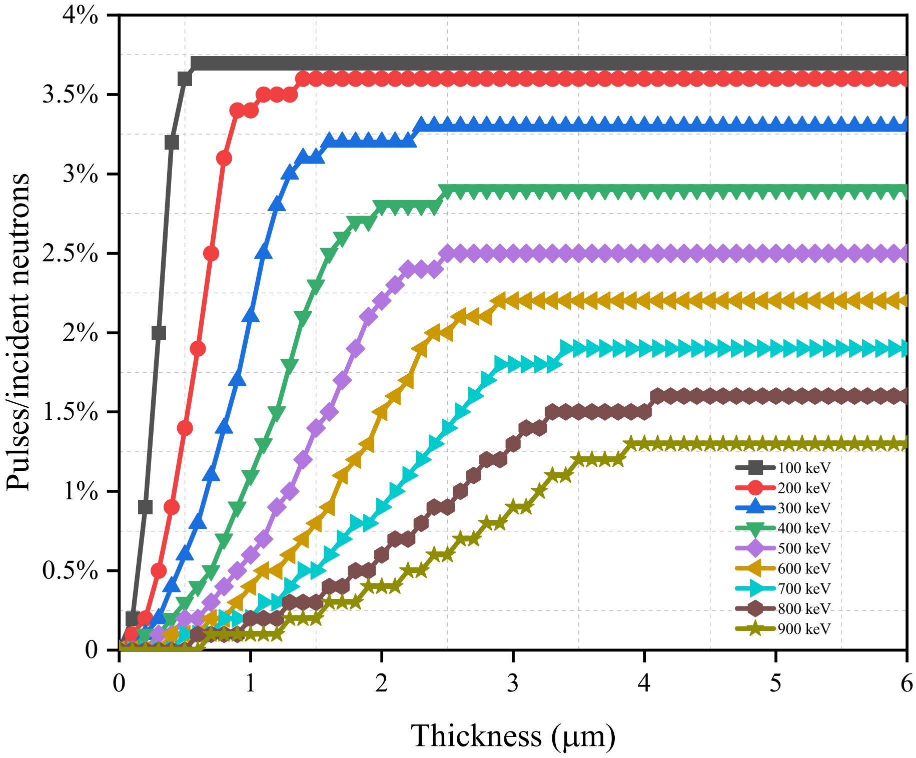

Figure 5: Neutron detection efficiency versus semiconductor material thickness with optimal B_4C converter layer thickness for $CsPbBr_3$ with LLD range from 100 keV to 900 keV.

Table 6: Optimised semiconductor thickness with optimal LiF converter layer thickness for diamond with LLD range from 100 keV to 900 keV.

LLD (keV)	100	200	300	400	500	600	700	800	900
Thickness (μm)	1.5	2.5	3.5	4.5	5.5	6.0	8.0	8.0	9.0

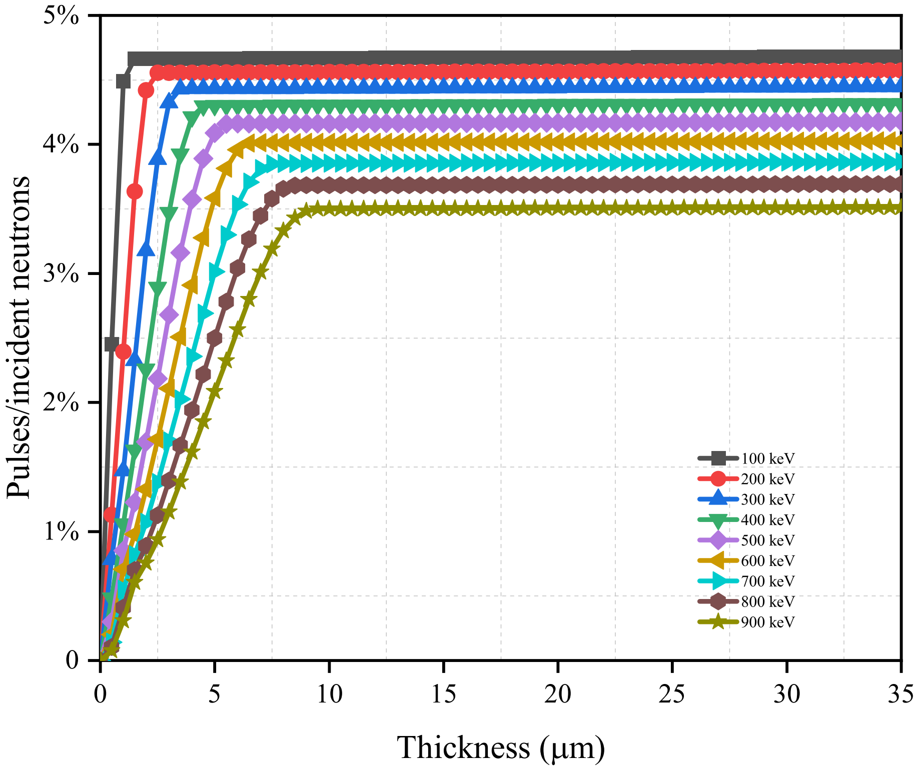

Figure 6: Neutron detection efficiency versus semiconductor material thickness with optimal LiF converter layer thickness for diamond with LLD range from 100 keV to 900 keV.

Table 7: Optimised semiconductor thickness with optimal LiF converter layer thickness for SiC with LLD range from 100 keV to 900 keV.

LLD (keV)	100	200	300	400	500	600	700	800	900
Thickness (μm)	2.0	3.5	4.5	5.5	7.5	8.0	11.0	11.0	12.0

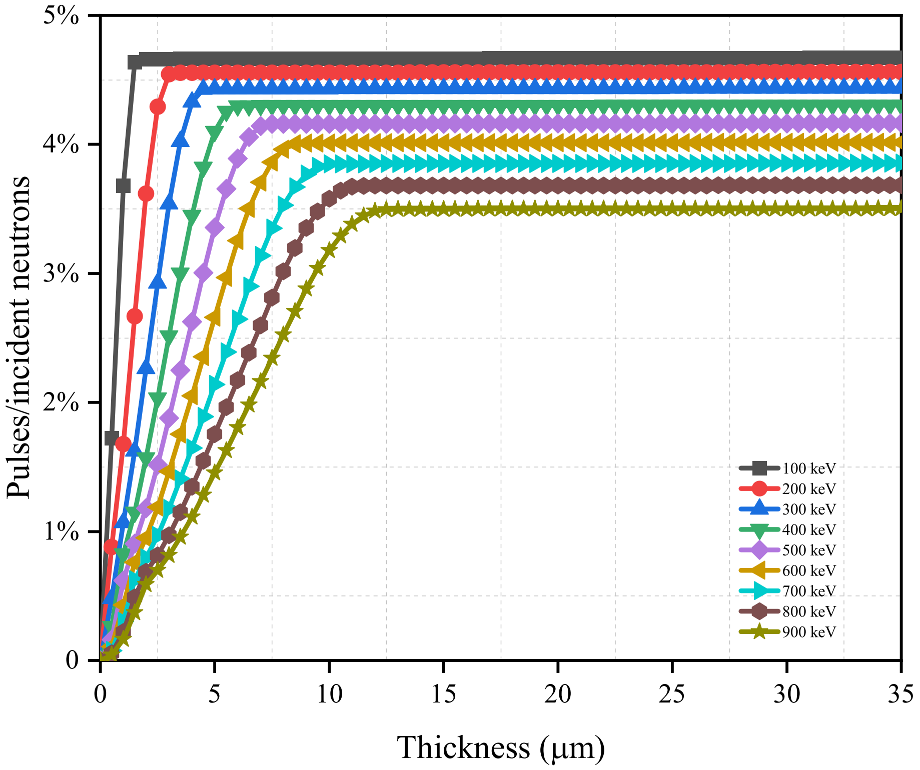

Figure 7: Neutron detection efficiency versus semiconductor material thickness with optimal LiF converter layer thickness for SiC with LLD range from 100 keV to 900 keV.

Table 8: Optimised semiconductor thickness with optimal LiF converter layer thickness for Ga_2O_3 with LLD range from 100 keV to 900 keV.

LLD (keV)	100	200	300	400	500	600	700	800	900
Thickness (μm)	1.5	2.5	3.0	4.0	5.0	5.5	7.5	7.5	8.5

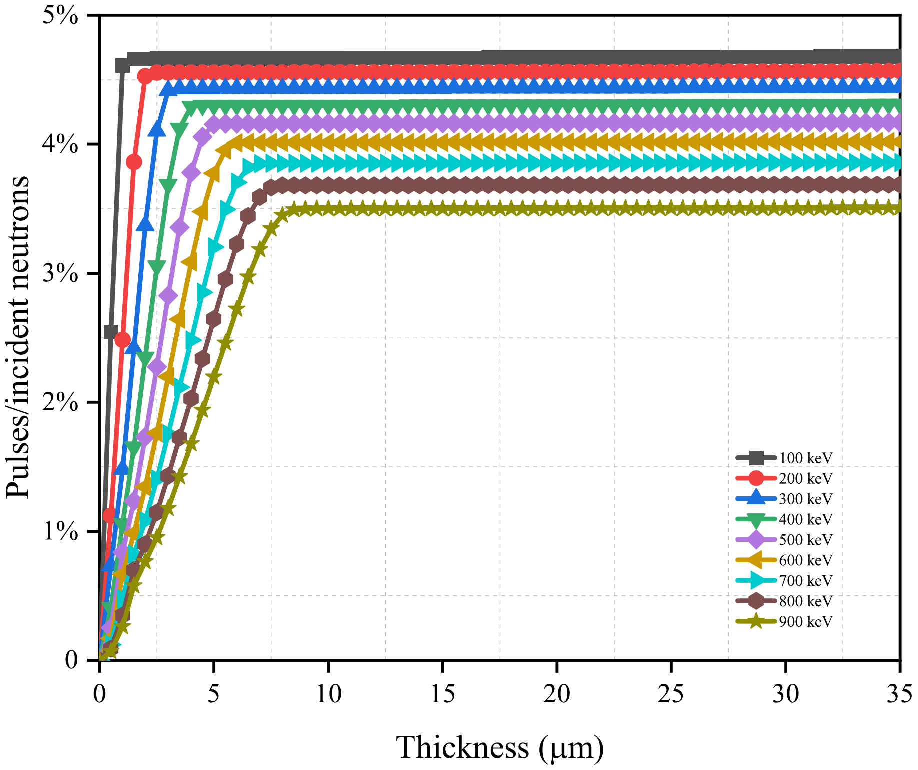

Figure 8: Neutron detection efficiency versus semiconductor material thickness with optimal LiF converter layer thickness for Ga_2O_3 with LLD range from 100 keV to 900 keV.

Table 9: Optimised semiconductor thickness with optimal LiF converter layer thickness for GaN with LLD range from 100 keV to 900 keV.

LLD (keV)	100	200	300	400	500	600	700	800	900
Thickness (μm)	1.5	2.5	3.5	4.5	5.5	6.5	8.0	8.5	9.0

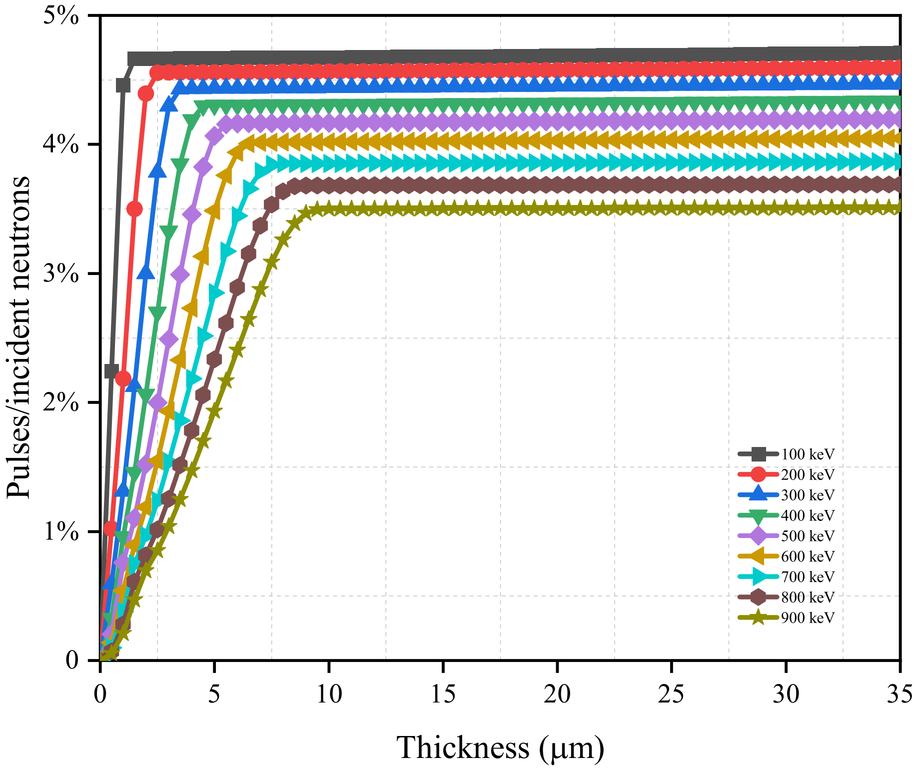

Figure 9: Neutron detection efficiency versus semiconductor material thickness with optimal LiF converter layer thickness for GaN with LLD range from 100 keV to 900 keV.

Table 10: Optimised semiconductor thickness with optimal LiF converter layer thickness for $CsPbBr_3$ with LLD range from 100 keV to 900 keV.

LLD (keV)	100	200	300	400	500	600	700	800	900
Thickness (μm)	3.0	5.5	7.0	9.0	12.0	13.5	15.0	17.5	19.5

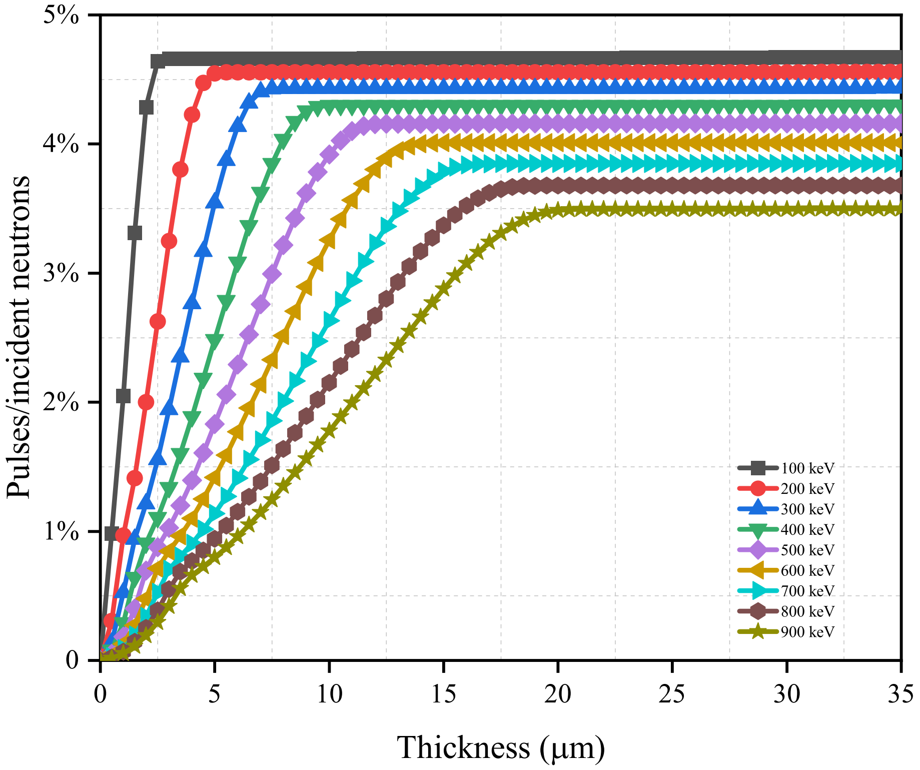

Figure 10: Neutron detection efficiency versus semiconductor material thickness with optimal LiF converter layer thickness for $CsPbBr_3$ with LLD range from 100 keV to 900 keV.